FABRICATION OF CARBON/SILICON CARBIDE LAMINATE COMPOSITES BY LASER CHEMICAL VAPOR DEPOSTION AND THEIR MICROSTRUCTURAL CHARACTERIZATION

A Thesis

Presented to

The Academic Faculty

By

Joshua Robert Gillespie

In Partial Fulfillment

Of the Requirements for the Degree

Master of Science in Mechanical Engineering

Georgia Institute of Technology

January 2004

FABRICATION OF CARBON/SILICON CARBIDE LAMINATE COMPOSITES BY LASER CHEMICAL VAPOR DEPOSTION AND THEIR MICROSTRUCTURAL CHARACTERIZATION

Approved

W. Jack Lackey, Chairman

J. Qu

S. K. Sitaraman

Date Approved: January 5, 2004

DEDICATION

I would like to dedicate this thesis to my family whose love and support have pushed me to excel throughout life. I would like to especially remember my grandfather, Robert S. Haywood, for shaping my desire to be a Ramblin' Wreck from Georgia Tech. My fianceé, Jennifer Leigh Pharris has given me immeasurable encouragement throughout this year to accomplish my work. With deep appreciation, I give thanks to my fraternity Θ Ξ, and all my friends whose fellowship has uplifted me through all college struggles. My family, Jennifer, and all my friends constitute only a part of the grace God has given me to achieve.

ACKNOWLEDGEMENT

I would like to acknowledge the assistance and leadership of my advisor, Dr. Lackey, in my graduate school undertaking. When he hired me as an undergraduate intern, he provided me with an excellent opportunity to pursue my Master's degree in a challenging field. As a fatherly advisor and a professor, he created an atmosphere of friendship that was transmitted to the research team. Working under him has been one of my most pleasant experiences.

The research team under Dr. Lackey, both past and present, were an integral part in the success of my work. I would like to give thanks to Dr. Chad Duty whose previous work, especially in solid modeling has greatly assisted my development as an undergraduate and graduate research assistant. I appreciated the mechanical expertise of Ryan Johnson and Scott Bondi whose care for the LCVD system enabled me to carry out my experiments. The hours of running experiments were aided by the company of Jian Mi, who helped my initial experiments. Sharing an office with Dr. Mingxuan Jiang and enjoying some spirited discussions with her made my days at work even more enjoyable. I am very grateful for having the opportunity to work with such fine people.

I would like to give thanks to the Woodruff School of Mechanical Engineering at the Georgia Institute of Technology. Both the ME Department and Tech have challenged me to grow into a stronger individual and professional. Lastly, I would like to give thanks to Dr. S. K. Sitaraman and Dr. J. Qu for being on my reading committee.

TABLE OF CONTENTS

DEDICATION……..……..... iii

ACKOWLDEGEMENTS…….……....iv

LIST OF FIGURES……viii

LIST OF TABLES…….…....xi

SUMMARY…….....xii

CHAPTER I- INTRODUCTION AND BACKGROUND…….……....1
I.1. Chemical Vapor Deposition……..1
I.2. Laser Chemical Vapor Deposition……1
I.3. Composite Manufacturing…….2
I.4. Industrial Applications of LCVD Laminate Processing……3
I.5. Research Scope and Deliverables……..3

CHAPTER II- LITERATURE REVIEW OF LCVD…….5
II.1. General LCVD Process…….5
II.1.2. Photolytic LCVD……7
II.1.2. Pyrolytic LCVD……...8
II.2. LCVD Materials and Structures……9
II.2.1. LCVD Materials……...9
II.2.1. Structures……....11
II.2.1.1. Direct Writing and Dots……11
II.2.1.2. Fibers and Walls……....13
II.2.1.3. Complex Structures……...16
II.3. Silicon Carbide and Carbon Deposition……..18
II.3.1. Silicon Carbide Deposition……....18
II.3.2. Carbon Deposition……..21
II.4. Thermal Stress Analysis for Laminates and Coatings…….22

CHAPTER III- EXPERIMENTAL APPARATUS AND PROCEDURES…….25
III.1. Current LCVD Rapid Prototyping System……25
III.2. Experimental Setup……27
III.3. Post Experimental Apparatus…….28
III.4. Design of Experiments……...29
III.5. Hypothesis of Factor Effects……..29
III.6. Laminate Experimental Procedure…….32
III.7. Reagent Delivery Calculations and Controls…….33

III.8. Codeposition Experiments……36
III.9. Stress Modeling……37

CHAPTER IV- EXPERIMENTAL RESULTS…… 39
IV.1. Modifications to Experiments……...39
IV.1.1. Thermal Imager……39
IV.1.2. Gas Jet Reagent Delivery……40
IV.1.3. Substrate Surface Polishing……41
IV.2. Preliminary Results: Optical Microscope……41
IV.3. Thermal Imager Profile Testing……....42
IV.4. Experimental Results……....44
IV.4.1. Laminated Deposition: Trial 1……44
IV.4.2. Laminated Deposition: Trial 2……....46
IV.4.3. Laminated Deposition: Trial 3……47
IV.4.4. Laminated Deposition: Trial 4……48
IV.4.5. Laminated Deposition: Trial 5……49
IV.4.6. Laminated Deposition: Trial 6……52
IV.4.7. Laminated Deposition: Trial 7……56
IV.4.8. Laminated Deposition: Trial 8……58
IV.4.9. Laminated Deposition: Midpoint Trial……61
IV.4.10. Codeposition: Trial 1……65
IV.4.11. Codeposition: Trial 2……67
IV.4.12. Codeposition: Trial 4……69
IV.4.13. Codeposition: Trial 7……70
IV.4.14. Codeposition: Midpoint Trial..……..74

CHAPTER V- CONCLUSIONS……76
V.1. Laminate Conducive Conditions……76
V.2. Variable Effects……77
V.2.1. Temperature……..77
V.2.2. Scan Rate……...78
V.2.3. Reagent Switch Time……79
V.2.4. Pressure……79
V.2.5. Gas Jet……...79
V.3. Regression Analysis……...80
V.4. Overview……...81

CHAPTER VI- RECOMMENDATIONS…….. ...83
VI.1. Square-Flat Temperature Profile…… ..83
VI.1.1. Concept……...83
VI.1.2. Implementation……...84
VI.1.3. Advantages……...84
VI.2. Design of Experiments……...…85
VI.2.1. Laminated Composites……..…85
VI.2.2. Codeposition……..…87

APPENDIX……..….....90

REFERENCES……...127

LIST OF FIGURES

Figure 2-1A. A dot shaped carbon deposit with a slight volcano[20]…….12

Figure 2-1B. A dot shaped carbon deposit with a pronounced volcano effect[2]……..12

Figure 2-2. Direct writing……13

Figure 2-3. Single pass carbon wall[22]……..13

Figure 2-4. Fiber growth……14

Figure 2-5. Carbon fiber grown by LCVD[21]…..……..14

Figure 2-6. Cross sectional area of a carbon muli-layered wall……..16

Figure 2-7. Outer morphology of a carbon multi-layered wall……...16

Figure 2-8. Two-dimensional assembly made from angled carbon fibers[20]……...17

Figure 2-9. Carbon nanotubes[22]……..17

Figure 2-10. Carbon microspring produced by LCVD[25]……...18

Figure 2-11. Multiple degrees of freedom are coordinated to build a helical microspring……..….18

Figure 2-12. Nodular LCVD SiC coating……...21

Figure 2-13. Globular morphology of LCVD SiC surface.……21

Figure 2-14. Columnar morphology near a cut made by moving the laser beam across a previous deposit[21]……22

Figure 2-15. Surface morphology of LCVD C/SiC showing volcano effect with cracking and delamination……..23

Figure 2-16. Cross sectional view with cracking and delamination of C/SiC laminate……...23

Figure 3-1. CAD model and photo of the Georgia Institute of Technology LCVD Rapid Prototyping System……25

Figure 3-2. Cross sectional view of upper chamber design…….26

Figure 3-3. Experimental setup for the SiC/C laminate composite investigations……..28

Figure 3-4. Laser spot of fiber growth as observedby the thermal imager……..30

Figure 4-1A. An SEM micrograph of wall 1-2-2 showing the top of the deposit……...45

Figure 4-1B. An SEM micrograph of wall 1-2-2 showing the deposit's cross section ..45

Figure 4-2. Cross sectional view of wall 4-2-2……48

Figure 4-3A. External view of wall 5-2-2 with a trace SiC layer beside the wall……...51

Figure 4-3B. Overhead view showing the narrow and steep volcano with no cracks….51

Figure 4-4. Transverse cross section view of wall 5-1-1 showing the original deposit (right) and the process flaw (left)……...52

Figure 4-5. Wall 6-1-1 with nodular formation and volcano cracks……53

Figure 4-6. Transverse cross section of wall 6-1-2, largely a silicon carbide deposit with a carbon vein …….54

Figure 4-7. Through-the-thickness cracks in wall 6-1-2……..54

Figure 4-8. Overhead view of wall 7-1-2 exhibiting different morphologies …….56

Figure 4-9. Volcano effect of wall 8-1-2 with stratified carbon microstructure and patchy deposits of silicon carbide …….58

Figure 4-10. Volcano center showing cauliflower morphology……..59

Figure 4-11A. Wall 8-2-1 cross section of a silicon carbide deposit with a carbon vein…….60

Figure 4-11B. Higher magnification of the voids and cracks near carbon vein……...60

Figure 4-12. Volcano effect and multiple morphologies of wall 8-2-2……...61

Figure 4-13A. Stratifications in volcano for wall MP-1-1……..62

Figure 4-13A. Globular substructure of the volcanostratification in wall MP-1-1…….62

Figure 4-14A. Volcano of wall MP-2-1 with evidence of carbon deposition in the volcano center…….……...64

Figure 4-14B. Volcano center showing no evidence of carbon deposition…….64

Figure 4-15. Crack deflection in wall MP-2-2……65

Figure 4-16. Wall 2-3-2 with tubular growths on trace deposit……..67

Figure 4-17A. Fiber 2-3-F1 changes from out-of-order to controlled growth……68

Figure 4-17B. Fiber 2-3-F2 remains a flawed deposit throughout process……68

Figure 4-18. Stalactite growth from the tip of 2-3-F2……69

Figure 4-19A. Overhead view showing minimal volcano and consistent morphology in fiber 7-3-1……..71

Figure 4-19B. Traverse cross sectional views shows layered growth of fiber 7-3-1…..71

Figure 4-20A. Fiber 7-3-F1 with pronounced volcano effect…….73

Figure 4-20B. Stratified inner surface of volcano in fiber 7-3-F1……...73

Figure 4-21. Bristle-like formations emerging from the columnar morphology…….73

LIST OF TABLES

Figure 2-1. Various materials deposited by LCVD…….10

Figure 3-1. Factor levels for the design of experiments……..32

Figure 3-2. Codeposition factorial experiment setup……..37

Figure 4-1. Thermal imager filter temperature ranges…….39

Figure 5-1. Experiments which produced laminates……76

Figure 6-1. Initial design of experiments for square-field laser……...86

SUMMARY

Laser Chemical Vapor Deposition (LCVD) is a process by which reagent gases are thermally activated to react by means of a laser focused on a substrate. The reaction produces a ceramic or metallic deposit. This process is a derivative of Chemical Vapor Deposition (CVD), which is currently used in industry, among other things, as a coating technology for high performance parts such as turbine blades, cutting tools, microelectronics. LCVD differs substantially from CVD, because CVD produces deposits that cover the entire substrate since the furnace, which houses the substrate produces a globally heated reaction zone. LCVD uses a laser to yield precision deposits on the order of the laser spot size. For this investigation, a CO_2 laser with a 200 μm spot size was employed to transmit up to 100 W of power.

From a materials perspective, laminated composites are used for a variety of applications because two materials as a composite can yield more desirable thermal, electrical, and mechanical properties than either material by itself. This investigation focuses on the use of LCVD as a method for producing laminated composites, specifically carbon/silicon carbide laminates. The laminates that were produced were examined using scanning electron microscopy (SEM) and electron dispersive spectroscopy (EDS) to determine composition. Deposit geometrical characteristics such as laminate thickness and "volcano" depth as well as deposit morphology were also determined using SEM. Another subset of experiments was performed for the purpose of simultaneously depositing carbon and silicon carbide, ie., codeposition.

Carbon/silicon carbide laminates consisting of up to 4 layers (two per material) were prepared. The most uniformly shaped layers were prepared at the lower temperatures investigated. Laminates prepared at higher temperatures were less desirable in that a valley was present along the length of the strip of laminate. Some desirable traits for laminates were observed, chiefly crack deflection. When a crack intercepts a laminate interface the crack can be deflected along the interface instead of penetrating the layer. Crack deflection serves to disperse the energy causing the crack and maintain the integrity of the material. SEM micrographs demonstrate how crack deflection aided in cracks induced by thermal stress. A regression analysis was performed for subjective measurements such as overall deposit quality and volcano effect. Plus the analysis was performed for the deposit width and height. The temperature variable and the reagent switch time proved to be the most important variable in effecting deposit quality and the volcano effect. For the dimensional analysis, only the temperature proved to have a significant effect on the data.

The results demonstrate that the temperature profile present across the deposition region has a negative effect on the deposits because steep temperature gradients caused differing deposition rates across the width of the deposit. The lower deposition rates occur in the deposit center where higher temperatures are present. To minimize the temperature gradients caused by the Gaussian laser power distribution, a recommendation was made to install a four facet prism in the path of the laser beam. A four facet prism would split the beam into four sub beams. The sub beams could be focused so that the centers mark the corners of a square. This square region would exhibit a much more uniform temperature field which would permit more uniform growth conditions across

the width of the deposition zone. This should improve deposit uniformity and integrity. The decrease in thermal gradient should reduce thermally induced stress. Future experiments with the "four sub beam system" are proposed taking into account the process knowledge gained from this thesis research.

CHAPTER I

INTRODUCTION AND BACKGROUND

I.1. Chemical Vapor Deposition

Chemical Vapor Deposition (CVD) is a process by which reagent gases flow through a furnace to either decompose a reagent or to cause two reagents to chemically react. The reaction yields uniform ceramic or metallic coatings on a substrate or located within the furnace. In industry, CVD has been used for a variety of purposes. Many materials, including silicon carbide coatings for turbine blades to guard against oxidation and dielectric films like silicon nitride, are produced by CVD. CVD process variables, such as temperature, pressure, reagent composition, and flowrate can be controlled to yield materials with the desired film thickness, crystallinity, and morphology. CVD produced materials are known for high purity. The advantages of versatile applications, multiple materials, a high degree of process control, and chemical purity have made CVD an important and sustaining tool of industry.

I.2. Laser Chemical Vapor Deposition

Laser Chemical Vapor Deposition (LCVD) is a derivative of CVD. Instead of global heating of a substrate to induce deposition, a laser is used to cause a local CVD reaction at the spot heated by the laser. LCVD processes have the same advantages mentioned above for CVD. In addition, LCVD is capable of precision deposition as opposed to global deposition. By moving the laser relative to the substrate complex geometries with

a high degree of precision have been constructed demonstrating the flexibility of LCVD. Currently, research is being focused on understanding the deposition variables to gain control of the process. As of now, LCVD has limited industrial use, but there is potential for applications that require high precision processing and flexible manufacturing such as rapid prototyping, once LCVD has been more thoroughly investigated.

I.3. Composite Manufacturing

Composite materials offer potential in almost every industrial endeavor. Composites can be excellent for structural reinforcements. For example strong ceramic fibers can be dispersed throughout a metallic matrix to provide greater high temperature strength to prevent yielding. Ceramics suffering from brittle fracture can be processed with ceramic or metallic whiskers, which enhance fracture toughness. Single material composites, where the material is isotropic, can alter the direction of crystal growth, so that properties like thermal conductivity can be manipulated to produce desirable temperature gradients such as ceramic stove tops. Perhaps a material suffers from a significantly weaker Young's modulus in a certain crystal direction. Multiple grains will not allow a component to have a preferential yielding direction due to the mixed crystal orientations, thus rendering the material essentially isotropic.

Laminated composites have two particular useful applications, crack deflection and oxidation protection. Carbon is a very useful material structurally, but its integrity can be damaged by oxidation occurring at high temperatures. A material like silicon carbide has very favorable bonding capabilities with carbon to form composites and also can resist oxidation at high temperatures. However a single coating can still crack leaving

depletion zones for oxidation at the sites of the crack. By altering the coating to consist of alternating graphite and silicon carbide layers, cracks can be deflected along the interfaces of the layers. Even though these cracks can still run through the entire coating thickness, the cracks will be longer and will hinder the oxidation of the carbon structure.

I.4. Industrial Applications of LCVD Laminate Processing

LCVD can readily produce silicon carbide and carbon. If effective composites can be manufactured, there are substantial uses for high precision composites. Currently carbon or graphite is used in high temperature aerospace applications, but a silicon carbide coating is necessary to provide oxidation protection. Microelectronic processing requires high precision and LCVD can provide the necessary high resolution manufacturing for any lamination tasks. In addition to carbon and silicon carbide, many other material combinations are awaiting feasible process capabilities to utilize the higher performance of composites. The key to this feasibility is the understanding and control of process variables to produce materials with effective mechanical, thermal, and electrical properties.

I.5. Research Scope and Deliverables

The scope of this investigation is to use an available LCVD rapid prototyping device at the Georgia Institute of Technology to fabricate carbon/silicon carbide laminate structures and analyze them with respect to morphology, geometry, and structural integrity. The process variables of temperature, scan rate, reagent interchange time and pressure were manipulated to quantify the effects on laminate structure. Scanning

electron microscopy (SEM) was used to observe the specimen's morphology and geometric characteristics. The geometric attributes of concern were deposit width, height, planarity, and volumetric deposition rate. The material composition of the laminated materials was determined by EDS. These characterization results were use in conjunction to determine the preferred process parameters for the production of carbon/silicon carbide laminate manufacturing by LCVD. This feasibility study will provide operating conditions suitable for future focused studies of laminate processing by LCVD.

CHAPTER II

LITERATURE REVIEW OF LCVD

The literature review presented here details the history of LCVD research as burgeoning technology derived from CVD. Previous modeling of the deposition process is discussed along with the structure and materials produced by LCVD. Specifically, the deposition process of silicon carbide and carbon are reviewed as these materials are the focus of the research presented in later chapters. A review of nano indentation as a means of mechanical property inspection is presented since this is a promising tool for characterizing laminates and thus for determining how process parameters affect deposit quality.

II.1. General LCVD Process

LCVD was conceived from the incorporation of a laser into the already commercially established CVD process in the 1970's. The first research into the process began with Nelson and Richardson in 1972, where a CO_2 laser was used to grow carbon fibers from ethane and methane reagents.[1] Since this inception, LCVD has been used to produced a variety of geometries using numerous materials. Much of the understanding of LCVD has been developed from thermal and mass transport modeling. LCVD has two main subdivisions depending on how the laser induces the deposition process. These are photolytic and pyrolytic deposition, which are discussed below.

Currently attempts are being made to fashion LCVD among the rapid prototyping technologies, such as the one employed at the Georgia Institute of Technology.[2] Rapid prototyping is a manufacturing technology where prototypes are fabricated by sequential layering. The advantage of layered manufacturing is that the process is flexible with regards to geometry, which reduces the production time of prototypes. Currently stereolithography, selective laser sintering, fused deposition modeling, and laminated object manufacturing are among the commercially available rapid prototyping systems.

The reactions in LCVD are either combination reactions of reagents or reagent decomposition. Usually the reagents involve a substantial quantity (molar ratios of 10:1) of hydrogen or helium mixed with a gas that contains the elements for the material that is desired for deposition. Equations 1 and 2 clarify the basic reaction with a general and specific reaction.

$$A_{(g)} + B_{(g)} \rightarrow C_{(s)} + D_{(g)} \qquad (1)$$

$$SiCl_4 + 2H_2 \rightarrow Si + 4HCl \qquad (2)$$

The deposits produced in LCVD typically are pure substances with low porosity. However, some reagents like methyltrichlorosilane (MTS) have the ability to co-deposit multiple materials depending on the conditions. Deposition from MTS, which was used in this research, will typically yield silicon carbide, but excess silicon or carbon has been known to form during CVD reactions.[3] Overall the pure substances are ideally suited for electronic devices and novel structural materials. Currently the challenge is to gain more

control over the morphology (i.e. reduce cracks or roughness) and the geometric capabilities.

II.1.1. Photolytic LCVD

Photolytic LCVD occurs when the photons from a laser cause the dissociation of the bonds in the gas phase.[4] This requires that the laser beam be aligned parallel to the substrate surface so that the reagent molecules just above the surface absorb the photon radiation and the dissociating solid particles are adsorbed onto the substrate. This process differs substantially from conventional CVD, because photolytic LCVD does not heat the substrate. This is a distinct advantage for processes where coatings are being applied to devices that are temperature sensitive. The deposition rates normally achieved for this process are quite small (~0.01 nm/min), which is inherently good for control, but is also inherently poor for rapid prototyping.[5]

The geometries of deposition using a parallel laser for photolytic LCVD are limited to simple films. However, the production of super lattice films (coatings with layer thickness on the order of nanometers) could be ideally suited for this process. Another limitation is that the deposition requires reagents species that can absorb the photons in order to dissociate. This requires that the wavelength of the laser be such that the reagents are opaque to the radiation and absorb the photons. Otherwise the radiation will simply transmit through the gas without interaction. Therefore photolytic processes are substantially limited with respect to deposition geometry and the reagents must be paired with the proper laser, all of which severely limits the flexibility of the process.

II.1.2. Pyrolytic LCVD

Pyrolytic LCVD systems, such as the one used at the Georgia Institute of Technology, uses a laser beam to locally heat the substrate at the laser spot to temperatures that thermally induce the reaction. Since this is a thermally activated process, a laser need only to produce the requisite temperature for deposition regardless of reagent type. This flexibility substantially differs from the aforementioned photolytic deposition.

Another flexible advantage of pyrolitic LCVD is that laser beam is usually normal to the substrate, so multiple geometries can be formed by moving the laser relative to the substrate. The depositon zone is regulated by the temperature gradients of the substrate, which are on an order of magnitude on par with the size of the laser. This provides a high resolution to the deposition process, making it suitable for research as a rapid prototyping process and for fabrication of complex geometrical parts. Most research on LCVD has been performed on the pyrolytic process because of its superior flexibility with respect to deposit geometry and a greater variety of materials available for deposition.

Deposition rates for the pyrolytic process can have a substantial range. This is largely dependant upon the temperatures achieved by the laser and the reagent gas pressure. There are three classifications for pressure conditions with respect to LCVD: 1)high pressure (1.5 atmospheres or more), 2) moderate pressure (0.5 to 1.5 atmospheres), and 3) low pressure (below 0.5 atmosphere). High-pressure deposition has achieved linear deposition rates of 100 μm/s and higher.[6] Whereas, the low and moderate pressures ranges typically yield linear deposition rates around 1.0 μm/s.[7] At this point all reference to LCVD will be understood to be pyrolytic LCVD.

II. 2. LCVD Materials and Structures

In the history of LCVD research, a wide variety of materials have been deposited from a similarly diverse set of reagents. LCVD systems have been designed to further this flexibility though moveable substrate stage designs that can produce multiple deposit shapes. Most research has been focused on producing more materials or furthering the control of the deposit shapes to enable useful industrial applications. This section briefly surveys the materials that have been successfully deposited by LCVD and basic geometries that are available for manipulation.

II. 2. 1. LCVD Materials

LCVD research has demonstrated that a wide variety of materials can be deposited, which provides areas for more research into reaction control and industrial application. Not only is it valuable to know what materials can be deposited, but it is just as important to investigate the materials that are suitable for substrates. The role of the substrate will be characterized later in the review. Table 2-1 displays the broad range of materials, both substrate and deposit, that can be produced by LCVD along with various statistics for fiber growth. This table is partially reproduced from the review of Duty, *et al*.[2]

Table 2-1. Various Materials Deposited by LCVD.

Deposit	**Reagents***	**Substrate**	**Pressure (mbar)**	**Linear Deposit Rate (µm/s)**	**Laser Type**	**Laser Spot (µm)**	**Laser Power (mW)**	**Ref**
Al	TMAA	Quartz	1-7.5	3	Ar	45	1100	8, 9
B	$B_2H_6 + H_2$	n/a	10^3-10^4	625-1100	Ar	20	200	10
Graphite	C_2H_4	B	400-5000	3500	Ar	10	12 000	11
Cu	$Cu(hfac)_2$	Si	20	n/a	Ar	45	8000	12
Diamond	C_2h_4	n/a	930	10/254	Ar	10	150	13
Ge	GeH	n/a	10^3-10^4	18-35	Nd:Yag	20	200	10
Ni	Ni(CO)4	C, AlO_3	250	n/a	Ar	35	n/a	14, 15
SiC	$SiH_4 + C_2H_2$	n/a	10^3-10^4	75-125	Nd:Yag	20	200	10, 16
W	$WF_6 + H_2$	B	1000	160	Ar	10	3000	11
TiC	$TiCl_4 + CCL_4 + H_2$	n/a	8	0.12	CO_2	800	800	17
Si	SiH_4	n/a	10^3-10^4	500	Nd:Yag	20	200	10
Fe	$Fe(CO)_4$	C, AlO_3	20	45	Ar	35	n/a	14
TiB_2	$TiCl_4 + BCL_3 + H_2$	Mullite	20	0.4	Co_2	9000	80 000	18, 19
WC	$WF_6 + C_2H_4 + H_2$	B	760	175	Ar	10	12 000	11

*TMAA = trimethyl-amine alane, $Cu(hfac)_2$ = copper bis(hexaflouroacetylacetonate)

II. 2. 2. Structures

The structures produced by LCVD are rooted in the ability to move the laser relative to the substrate. For a stationary laser, dot shaped deposits can be form with a diameter comparable to the size of the laser spot. If the laser is allowed to operate for a longer time a fiber will form longitudinal to the axis of the laser beam. If the laser scans the substrate, direct writing of a thin film will take place. By making multiple passes, a layered wall can be formed. The manipulation of these basic movements can produce a variety of shapes. Shapes of composite material are created by switching the reagent type.

II. 2. 2. 1. Direct Writing and Dots

The simplest of features created by LCVD are direct writing and dots. The dots are formed by keeping the laser stationary for a prescribed time. This time is determined by the deposit growth rate, which is influenced by the kinetics of the reaction and the mass transport of the reagent. The spot shapes range between either spherical domes or volcano like bowls. According to Jean,[20] these shapes are governed by the laser power and laser shape. The LCVD system at the Georgia Institute of Technology utilizes a CO_2 laser beam with a Gaussian power distribution. The peak power occurs in the center and trails off radially outward. Jean proposed that the peak temperatures are either less favorable for deposition or that as deposits are formed, laser ablation occurs on the fresh deposit. As the deposit's center begins to demonstrate a slower growth rate, the problem is further exacerbated because the volcano shape inhibits the mass transfer of reagent to the deposit center.

Thermal modeling by Duty[7] demonstrated that the diameter of the dot is related to the temperature distribution of the laser spot on the substrate. A sufficiently high temperature is

required to disassociate the reagents molecules. The deposit shape's diameter is thus limited to the diameter on the substrate where the minimum temperature exists to induce deposition. In this ideal case, a spherical dome is created, but in reality most spots do exhibit at least a slight volcano effect, demonstrating LCVD's need for high precision temperature control. Figure 2-1 shows two dot deposits where one (A) is a well shaped spherical dome with a slight volcano defect, and the other (B) is a flawed crater deposit. Dot shaped deposits have importance as the elemental deposit shape, because these dots have the potential to serve as small structural supports in microelectronics.

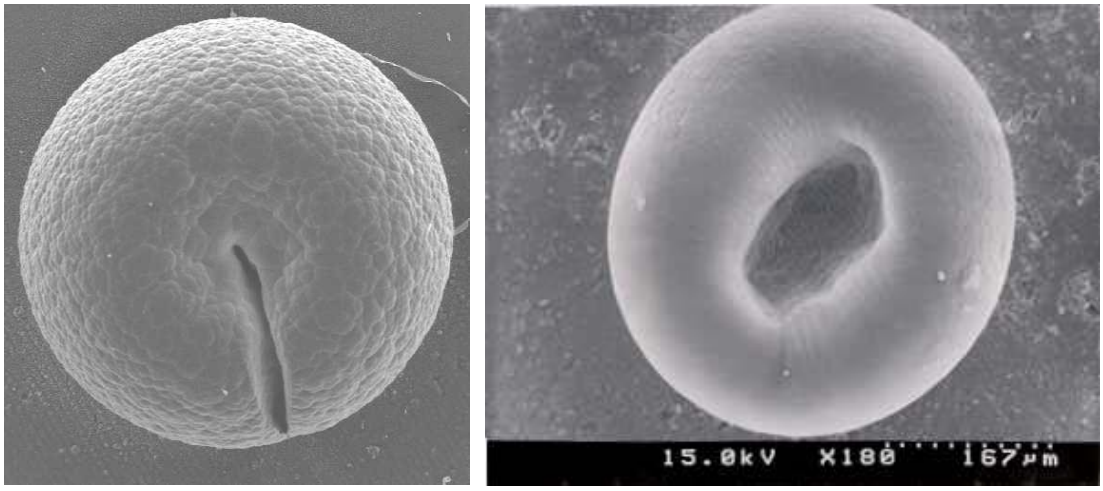

Figure 2-1A. (left) A dot-shaped carbon deposit with a slight volcano effect.[20]

Figure 2-1 B. (right) A dot-shaped carbon deposit with a pronounced volcano effect.[2]

Direct writing involves thin film deposition through the scanning of the laser across the substrate. The thickness of the film is quite dependent upon the scan rate. A slower scan rate will increase the temperature, the deposition rate, and the film thickness. Direct writing at atmospheric pressure has been accomplished with the Georgia Tech LCVD system with scan rates of 0.2 in/min. The heat and mass transfer dictate the morphology and deposition rate

for direct writing. Knowledge of shape and speed of the deposit could have practical uses for drawing electrical connections through embedded circuitry. Figure 2-2 illustrates the direct writing process and Figure 2-3 is a sample of a thin film produced by a single pass.

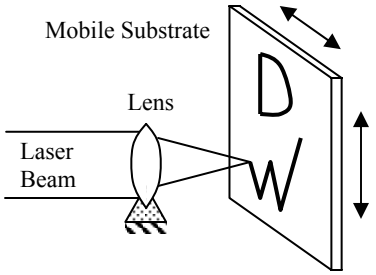

Figure 2-2. Direct writing.

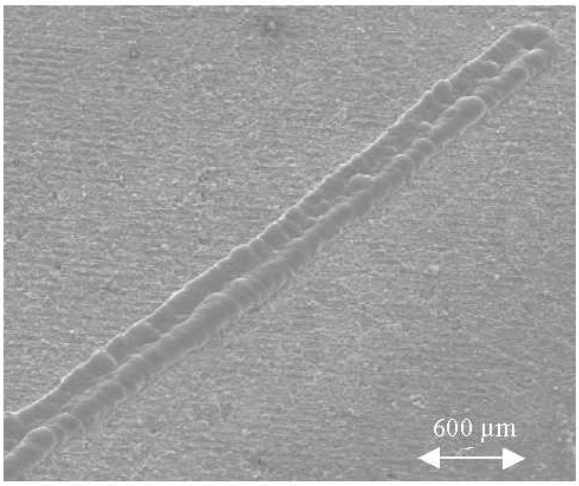

Figure 2-3. Single pass carbon wall.[22]

II. 2.2.2 Fibers and Walls

Fibers are produced by a stationary laser beam where the laser is kept in operation so that the deposit shapes grows out of the dot configuration into a long slender fiber. A fiber will continue growing toward the laser until the laser spot is so out of focus that the temperature drops below that necessary for deposition. This can be remedied through designs that employ a stage to move the substrate away from the laser at a rate equivalent to the fibers growth rate. Figure 2-4 demonstrates fiber growth where the stage speed maintains the focal point of the laser on the end of the fiber.

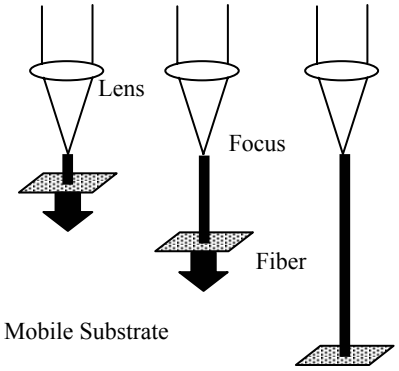

Figure 2-4. Fiber growth.

Without any stage movement at all, the fiber growth rate has been noted to be quadratic with respect to time. As a fibers grows, the heat transfer mode of conduction is "bottle necked" by the slender fiber, raising the temperature at the fiber tip. This increase in temperature increases the deposition rate until the fiber outgrows the laser focus and then fiber growth decays to nothing. Fibers with lengths on the order of inches have been grown. Unfortunately, the fibers can also show volcano effects on the distal tip. A carbon fiber is shown in Figure 2-5.

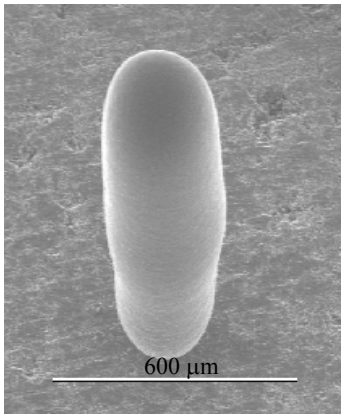

Figure 2-5. Carbon fiber grown by LCVD.[21]

Walls are constructed by moving the laser beam relative to the substrate so that the beam traverses in a back-and-forth pattern. Each pass of the laser builds more deposit upon the

previous pass. Thus a wall is constructed layer by layer. Ideally, LCVD walls produced by a Gaussian laser beam have a rectangular cross section with a slightly convex top. There are many challenges in the construction of walls. The volcano effect can still occur to give the wall a valley on the top running along the longitudinal axis of the wall. Another challenge in wall construction is that cross sectional views showing the inside of the deposit can often reveal cracks between the layers. This phenomena has been noted in layered CVD processes and could be due to residual stresses occurring from thermal expansion and contraction from laser heating.[23]

Control of this process can be quite complicated because of the interplay between the heat transfer and the scan rate. As the walls get higher, the conduction effects change, for similar reasons that the conduction changes in fiber growth. This makes the deposition of uniform layers challenging, but resolvable. Thermal models for wall construction have been created for LCVD by HAN and Jensen.[24] The current investigation will attempt to produce high quality composite walls. Figure 2-6 and 2-7 show the cross section and the outer morphology of a carbon wall, respectively.

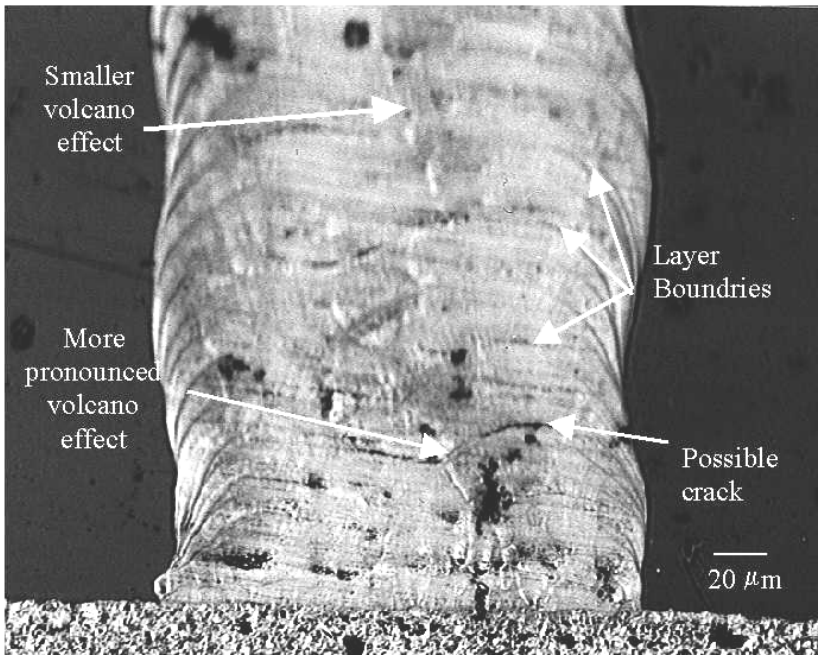

Figure 2-6. Cross sectional area of a carbon multi-layered wall.

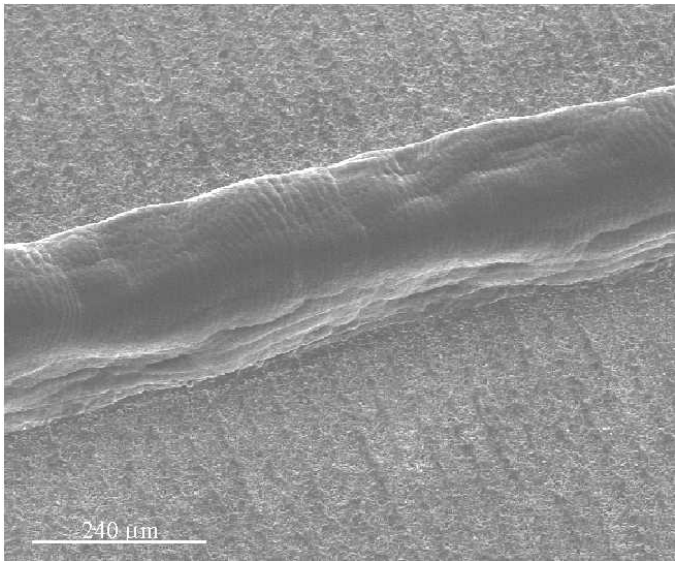

Figure 2-7. Outer morphology of a carbon multi-layered wall.

II. 2. 2. 3. Complex Structures

Through the manipulation of the basic geometric structures described above, complex geometries can be fabricated. Jean was able to produce two fibers grown at an angle to form

an apex shown in Figure 2-8.[20] Another LCVD structure grown at Georgia Tech is the formation of carbon nanotubes. The fiberous mesh of tubes are grown using lower temperatures (800°C) for brief time periods (2 minutes) with a stationary laser spot or a catalyzed substrate. A sample SEM micrograph of a nanotube network is displayed in Figure 2-9.

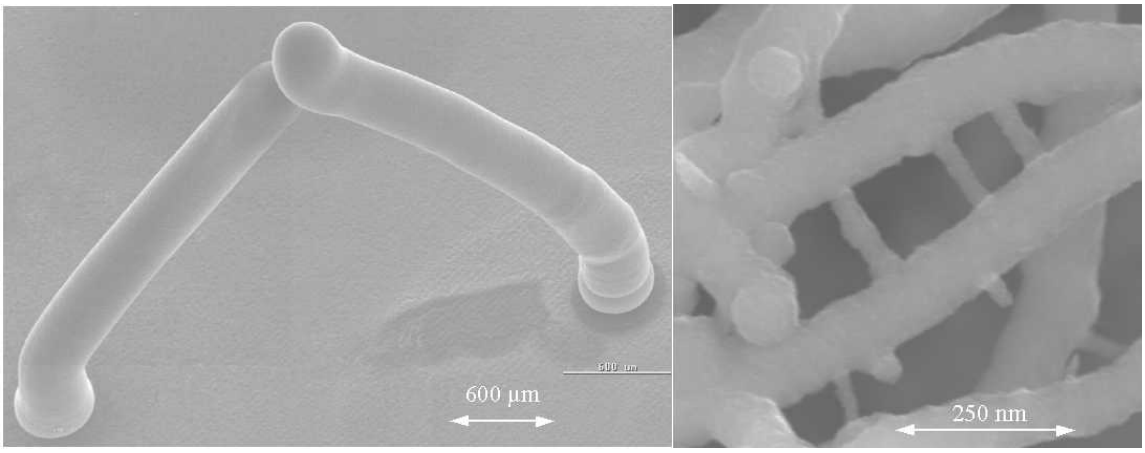

Figure 2-8. (Left) Two-dimensional assembly made from angled carbon fibers.[20]

Figure 2-9. (Right) Carbon nanotubes.[22]

Probably the most successful complex shapes achieved have been micro springs, such as the one produced by Maxwell, Williams, and *et al.* shown in Figure 2-10.[23] The helical spring can be produced by using a goniometer, where the deposit forms along the curved surface revolving cylinder that is also translating downward. Building a straight fiber followed by a combination of rotation and translation to form a spring can produce free-form micro springs. This cylindrical substrate assembly is shown in Figure 2-11. The ability to use various performs to manipulate deposition remarkably enhances the flexibility of LCVD,

but control of the deposition will be mastered through research on the process characteristics of the more basic shapes.

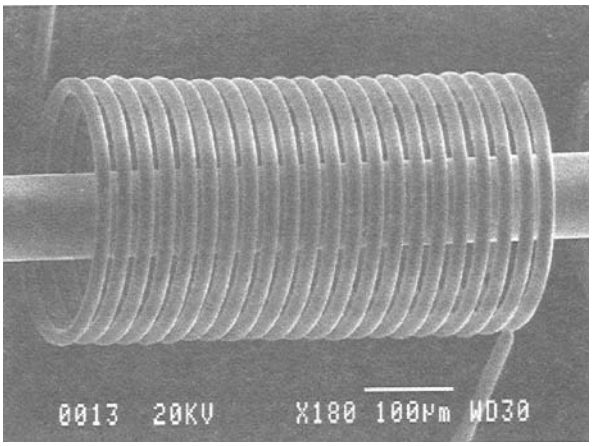

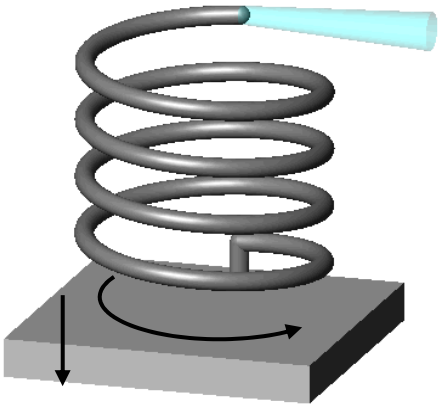

Figure 2-10. (Left) Carbon microspring produced by LCVD.[25]

Figure 2-11. (Right) Multiple degrees of freedom are coordinated to build a helical microspring.

II. 3. Silicon Carbide and Carbon Deposition

LCVD can readily deposit both silicon carbide and carbon. Carbon deposition via CVD is well understood and the LCVD of carbon is better understood than other materials. Silicon Carbide has mostly been investigated for possible applications as a CVD coating technology and only very limited LCVD of silicon carbide has been performed.[26] This section will detail the thermodynamics, morphology and crystalline structures of both processes and the results of previous investigations in both CVD and LCVD.

II. 3. 1. Silicon Carbide Deposition

MTS is the most commonly used gas for silicon carbide deposition. Kingon and *et al*. performed a thermodynamic study of silicon carbide deposition.[27] Silicon carbide can be

produced from a variety of reagent combinations such as $SiH_4/CH_4/H_2$, $SiH_4/C_2H_4/H_2$, $SiH_4/C_3H_8/H_2$, CH_3SiCl_3/H_2 (MTS), and $(CH_3)_2SiCl_2$/H2 (dimethyldichlorosilane). The hydogen gas is used as a carrier gas for the other reagents and is sometimes replaced with argon. Hydrogen also plays a role in increasing the deposition rate.[28] Of all the reagent systems investigated, the MTS/H_2 system proved to be the most reliable for silicon carbide production. Possible problems in the deposition process could be the yielding of free carbon or free silicon within the silicon carbide phase. When the molar ratio of H_2 to MTS exceeds 20:1, silicon carbide is the only phase present for pressures on the order of 0.1 to 100 kPa for typical deposition temperatures, 1200-1500°C.

The kinetics of silicon carbide deposition is governed by the Arrhenius Equation, demonstrated in Equation 3,

$$R_D = A*\exp(-E_a/(R*T)) \qquad (3)$$

where R_D is the deposition rate, A is a constant, E_a is the activation energy, R is the ideal gas law constant, and T is the temperature. The investigation by Besmann[29] revealed that the activation energy for the reaction is 188 kJ/mol and A is $1.607*10^{10}$ nm/min. For moderate deposition temperatures around 1250 K, this yields confirmed deposition rates around 150 nm/min, which are useful rates for coating technologies.

The morphology and crystal structure produced in silicon carbide deposition can vary widely. The most common structure for silicon carbide is β-SiC (a zinc blende lattice), which has a [111] orientation. The α-SiC structure with a [220] orientation can also appear in CVD, and presumably in LCVD, but the material properties are not as desirable. All other

structures do not have the stability to exist in the deposition. In the work of Chin *et al*., β-SiC was shown to be the predominant structure for temperatures ranging from 1400 to 1700 K.[30] The pressure for this investigation varied from 70-220 torr. As the temperatures exceeded 1700 K, α-SiC emerged as the major structure of the deposit.

Chin *et al*. also studied how the morphology of β-SiC was connected to the following variables of temperature, H_2:MTS ratios, and pressure.[30] Three morphology classification were identified: 1) smooth, 2) angular/columnar, and 3) faceted. Smooth morphology, which is usually the most desirable, was noted for temperatures below 1450 K. The columnar and angular morphology were observed from 1450 to 1750 K. The faceted (large crystal growth) morphology occured at temperatures above 1750 K and α-SiC was formed. Pressure and concentration ratio had only the slightest effects on the morphology. Increases in pressure would further the trend toward smooth deposits, and increases in the H_2:MTS ratio promoted more crystal growth and faceting. This is consistent with the previous statement that increases in H_2:MTS ratio would increase deposition rate. Flow-rates were not observed to change the morphology.

Figures 2-12 and 2-13 shows typical morphologies for SiC walls that have been produced at the LCVD Laboratory at the Georgia Institute of Technology. The figure on the left shows very nonuniform growth characteristics. This SiC coating looks like a conglomeration of several nodules. The desired morphology for a coating is a smooth surface. These nodules are sites for stress concentrations which may lead to more cracking in the coating. The micrograph on the right shows the grains of the coating. Even at this magnification, the grains are globular and suggest that the SiC will have a lower toughness and hardness. The stress concentrations from the globular grains and any residual stress induced by the thermal

activity of laser heating and cooing will result in lower toughness. The hardness tests can be affected by the nodules being more prone to failure from the stress concentrations.

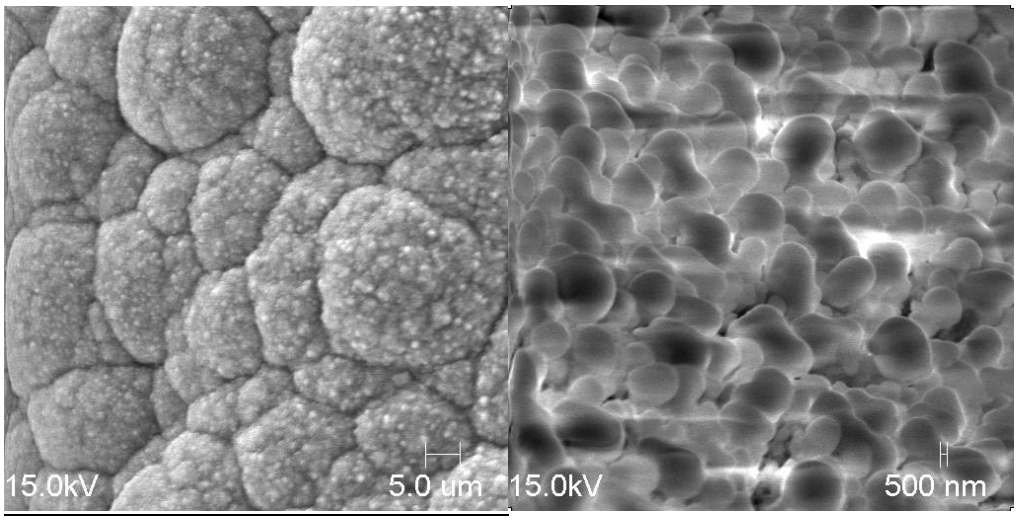

Figure 2-12. (Left) Nodular LCVD SiC coating.

Figure 2-13. (Right) Globular morphology of LCVD SiC surface.

II. 3. 2. Carbon Deposition

The deposition of carbon from methane is perhaps simpler than silicon carbide deposition from MTS. In methane (CH_4) only carbon is deposited, so there is no need to consider other phases in the deposit. In a thermodynamic analysis of carbon CVD in a methane/hydrogen environment, maximum carbon deposition was predicted at 2000 K and at 2500 K the deposition reaction would not proceed; the reagent converted to acetylene and other hydrocarbon gases.[21]

The kinetics of the LCVD of carbon is also governed by the Arrhenius equation. The activation energy for the LCVD of carbon in the previous investigation was found to be 176 kJ/mol and the pre-exponential constant was $4.433*10^{20}$ nm/min. Both of these factors

demonstrate that carbon deposition is substantially more rapid than silicon carbide deposition, which is why carbon deposition is being investigated more for bulk deposition.

The general morphology and crystal structure of carbon has already been largely discussed in the shapes produced by LCVD. The surface morphology of carbon deposition is typically columnar or smooth in appearance as displayed in Figure 2-14. This is typical of LCVD reactions with peak temperatures around 1700-2300 K. Carbon can have several crystal structures including graphite and diamond, though graphite material is more typical. The diamond structure has not been noted in LCVD methane experiments, but does occur when ethylene is the reagent.[2]

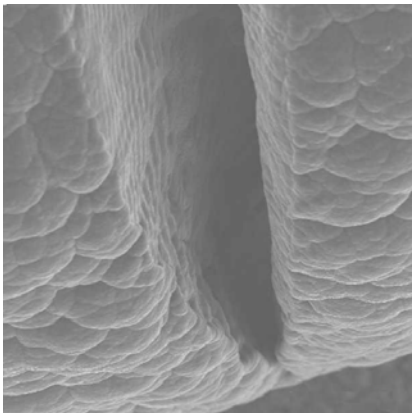

Figure 2-14. Columnar morphology near a cut made by moving the laser beam across a previous deposit.[21]

II. 4. Thermal Stress Analysis for Laminates and Coatings

One issue that needs resolution in LCVD is residual stress and cracks in the deposited material. One of the objectives of the present research is to model and investigate the process parameters of temperature, pressure, reagent switch time, and scan rate to reveal the

appropriate combination of factor levels to decrease cracking. The appearance of cracks will be observed through SEM.

Figures 2-15 and 2-16 demostrate the cracking and other deformities that exist in LCVD deposits for both outer morphologies and cross sections for laminated carbon and silicon carbide. Figure 2-15 is a close-up view of the inner surface of a volcano. The carbon on the micrograph's left has a crack running through it and there is some

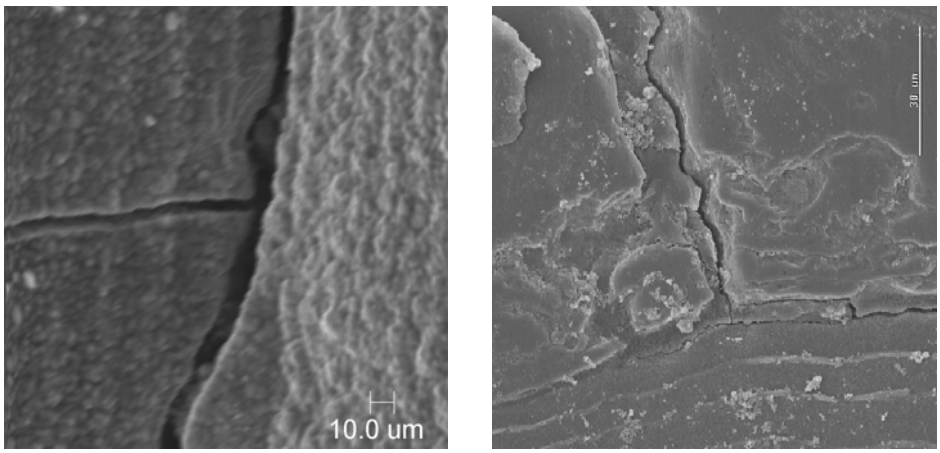

Figure 2-15. (Left) Surface morphology of LCVD C/SiC showing volcano effect with cracking and delamination.

Figure 2-16. (Right) Cross sectional view with cracking and delamination of C/SiC laminate.

delamination running vertically between the SiC on the right and the carbon. Figure 2-16 shows a cross section of a wall perpendicular to the long axis. A crack is running vertically through the thickness of the SiC and there is evidence of delamination with the carbon below.

For a detailed analysis of how nano indentation can be used to estimate properties other than hardness, see the literature from Suresh and Giannakopoulos.[31] In brief, a nano indenter

uses either a Vickers or Berkovich indenter to pierce a material. The system records the force load (P) versus indention depth (h) curve for both loading and unloading sequences. The initial slope of the unloading sequence is linear and this slope is used to determine the hardness and the elastic modulus of the material. However, if the material has residual stresses, the P-h curve is shifted from the curve associated with unstressed virgin material.

For ceramics, the plastic residual stress, σ^R, can be calculated using Equation 2-4,

$$\sigma_y^R = \frac{P_{\max}}{2.8 * A_{\max}} \tag{4}$$

where P_{max} and A_{max} are the maximum loads and indented areas from the test. A comparison with the known yield stress will confirm the calculation if the plastic residual stress is greater than the yield stress. Since cracking is evident in LCVD deposits, this work will focus on the investigation of plastic residual strains in the ceramic composites.

CHAPTER III

EXPERIMENTAL APPARATUS AND PROCEDURE

III.1. Current LCVD Rapid Prototyping System

The LCVD prototyping system at Georgia Tech was initially designed and constructed from 1997 to 1999. Since the first experiments in October 1999, several features have been added. Figure 3-1 displays the prototyping system used for the composite experiments.

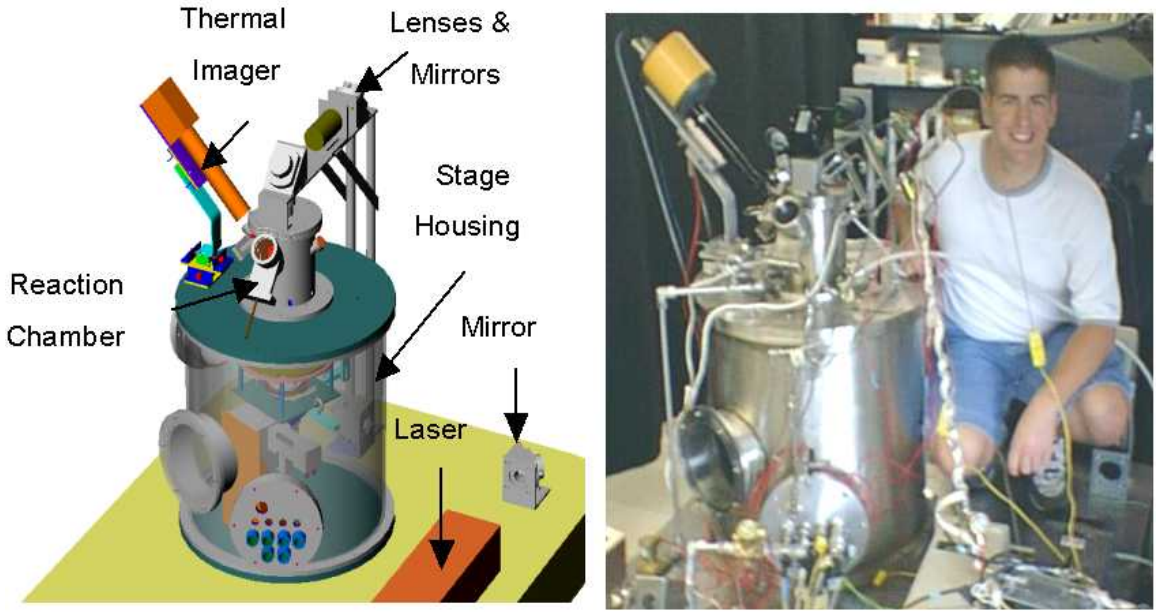

Figure 3-1. CAD model and photo of the Georgia Institute of Technology LCVD Rapid Protyping System.

Currently the system is a vertical two-chamber design. The top chamber houses the experimental reactor. This reaction chamber has various ports for delivering reagent gases

and exhausting by-product gases. Other ports are located on the reaction chamber for laser beam entry. The CO_2 laser enters the chamber vertically through an amber zinc selenide window. Figure 3-2 shows the cross-sectional view of the two chambers.

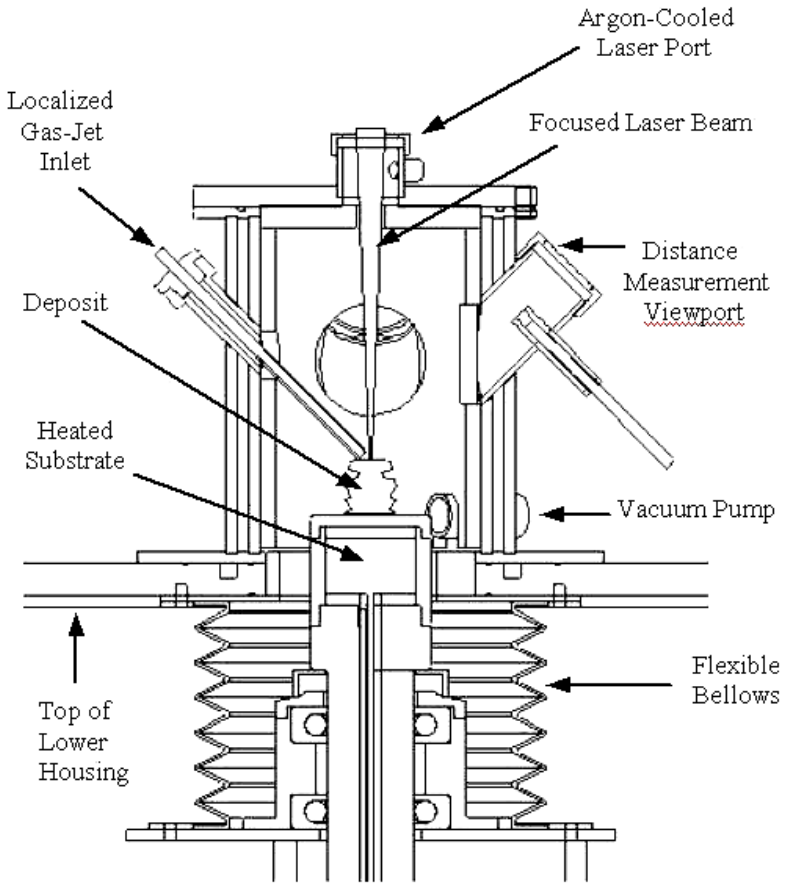

Figure 3-2. Cross sectional view of upper chamber design.

The reaction chamber features a substrate holder where the substrates are positioned for deposition. The substrate holder is a mobile platform to allow for relative movement between a laser beam and a substrate. Another feature, which is critical to controlling the shape of the deposition, is the gas jet, which delivers a stream of reagent directly to the heated laser spot. In order to monitor the deposition, another fused silica window port exists for a thermal imager. The thermal imager collects the infrared radiation from the deposition

process. Next, the thermal imager calculates the temperature that correlates with the received radiation signal. On a real time graphic display the temperature field of the reaction is presented on a computer monitor. Another attribute of the thermal imager is the control loop with the user interface so that a set point temperature, albeit peak temperature or area average temperature, can be maintained.

The lower chamber houses the stage assembly, which provides mobility to the substrate holder. Originally the stage assembly supported translational motion in the vertical direction and along one axis in the horizontal plane. Also, another stage supports rotation about the vertical axis. Recently in the Spring of 2003, another stage was installed to provide another horizontal translational axis, perpendicular to the other horizontal axis.

An elaborate reagent delivery and exhaust piping system connects the various gas cylinders, vacuum pump, scrubber, and laboratory hood vent. The gases available for deposition include methane, polypropelene, acetylene, and methyltrichlorosilane (MTS). Other gases available as carrier gases include hydrogen and nitrogen. Argon is used to pressurize the lower chamber with an inert gas so that stage electronics are protected from corrosion.

The whole LCVD prototyping system is controlled through a computer that employs a Labview graphical interface. The Labview programs control the power of the CO_2 laser, the mass flow controllers, solenoids, stages, vacuum pumps, and valves. This interface allows the user to monitor chamber pressures, laser spot temperatures, and stage positioning.

III.2. Experimental Setup

The experimental setup employed for laminated composite fabrication is presented in Figure 3-3. The methane and hydrogen are stored in pressurized tanks and the flow is

metered by mass flow controllers. The MTS is stored in a bubbler (vaporizer) with an entry port linked to a hydrogen supply line. The hydrogen is metered into the bubbler and the increase in pressure from the incoming gas forces the hydrogen and MTS vapor mixture to leave through the exit port. The hydrogen and MTS vapor mixture is diluted downstream by another hydrogen supply line. The mass flow controllers and valves are controlled through the Labview graphical interface.

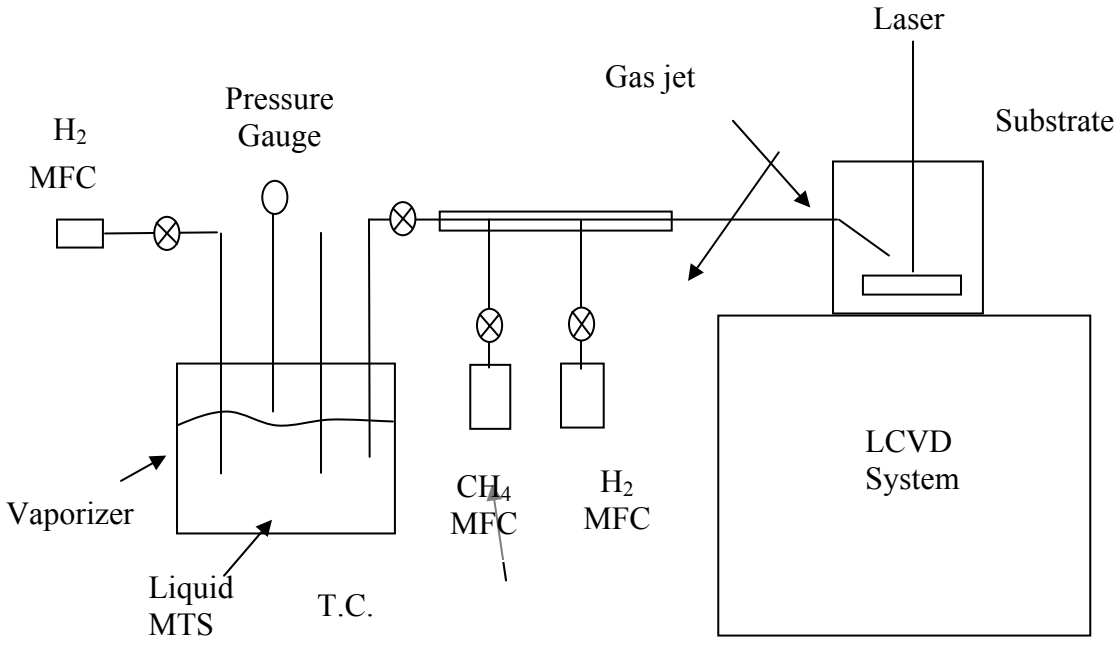

Figure 3-3. Experimental setup for the SiC/C laminate composite investigations.

Graphite substrates were used. The grades were AXQ and SK-85 and their surface preparation is described later in Section IV.1.2.

III.3. Post Experimental Apparatus

There are two major investigations to be made once the experiments are complete: geometric and mechanical properties. The geometric properties of deposit dimensions, deposition rate, surface quality, and cracks will be examined using the SEM located in the

Georgia Tech Research Institute (GTRI) under the supervision of Dr. Lisa Detter-Hoskin. This electron microscope has the capability of magnifying up to 300,000x and also has a functional EDS to evaluate the deposits material composition.

III.4. Design of Experiments

The design of experiments will consist of a 2^{4-1} design with a resolution of IV. The factors that will be investigated are deposition temperature, deposition pressure, reagent switch time, and scan rate. The factors will be two-level for high and low settings. The pressure factor will be aliased with the other three factors to provide a maximum resolution of IV. The pressure factor is suspected of contributing the least effect, especially with regard to material properties and component stress. Therefore, to more efficiently conduct experiments, the pressure factor was chosen to alias the remaining three factors. An ANOVA method will be employed to determine main effects of the singular factors.

III.5. Hypotheses on Factor Effects

The temperature factor is suspected to greatly influence the deposition rate, morphology, and the residual stress cracking of the deposits. The laser spot produces temperature fields that change on the order of 1000ºC over the distance of less than half a millimeter. A sample from the thermal imager is shown in Figure 3-4. Bond lengths in crystals are in equilibrium when maintained at the temperature they are formed. The significant cooling experienced by the crystals, given such high and compact thermal gradients must, play a role in the residual stress of the deposits and the cracks that have been observed. LCVD walls experience another thermal load because as the laser traverses back and forth over the wall, the crystals in the deposit experience multiple heating and cooling cycles. Thus, there is the potential for

thermal fatigue. On the positive side, higher temperatures can sustain a greater deposition rate, but perhaps at the cost of deposit quality.

The reagent switch time is the time used to flow a new reagent gas before beginning deposition by turning on the laser. If MTS is used to deposit silicon carbide and pure carbon deposition with methane is desired next, then the MTS must be purged from the upper chamber. This purging can be accomplished by evacuating the chamber and refilling with methane. Once filled, the methane is allowed flow for approximately ten minutes as a carrier gas to expel the MTS and dilute any remaining MTS to an insignificant level. Purging can be more time intensive and requires the lower chamber to be refilled with expensive high purity

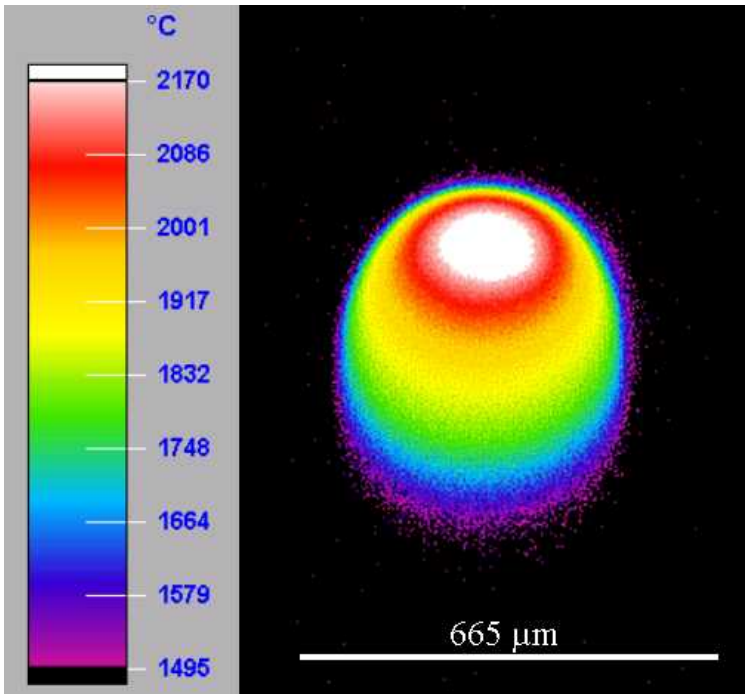

Figure 3-4. Laser spot of fiber growth as observed by the thermal imager.

argon. Instead, methane is allowed to flow for 15 minutes. At flowrates around 500 sccm, this should be enough to purge the MTS and allow single material laminates with minor codeposition.

For functionally graded material deposition, methane is flowed for only 2.5 minutes before the laser in engaged. This allows a significant amount of methane to begin deposition simultaneously with MTS. As time moves along, the flow of methane will slowly purge the preceeding MTS. This will produce a layer that has a gradual composition change throughout.

The former method has the advantage of producing single material laminates with both materials maintaining a high degree of purity. Purity in laminates can be advantageous for exploiting known and specific material properties. Chemical purity can also serve other purposes in electronic applications. The latter method can produce functionally graded materials. In many instances functionally graded materials have better mechanical properties. Components with well-defined interfaces can be subject to delamination at the interface. This is another reason why a small degree of codeposition is tolerated instead of using a full purge. A functionally graded material has a diffuse interface, thus hindering the materials from delamination. Functionally graded material may also have increased strength and toughness.

The scan rate variable should primarily affect the geometric properties of laminate walls. However, the scan rate does affect how long crystals are subject to the intense heat of the laser beam. Hence, faster scan rates could have the tendency to reduce residual stress. Alternatively, faster scanning could cause thermal shock from rapidly heating and cooling. Also faster scan rates could slow the deposition rate. The lesser time an area receives the heat of the laser beam, there is less time for deposition. A positive side to slower growth rates is that a greater resolution can be achieved for the layers. Smaller layer thicknesses can be more desirable than larger ones, particularly if the layers can be reduced to dimensions

less than about 50 nm where super lattice materials may form. If layers like this are possible, then the mechanical properties for the deposit could significantly change.

The pressure variable is largely only expected to affect the geometric properties. Lower pressures (300 torr) lead to lower deposition rates. This could help lead toward the development of super lattice structures previously mentioned. Also, if the pressure could influence the crystal microstructure, then physical properties could be altered. Since the pressure factor is deemed to have the least importance it has been selected as the aliasing variable to reduce the experiments by half.

III.6. Laminate Experimental Procedure

Table 3-1 illustrates the high and low levels used for the four-factor analysis. These conditions were used for the carbon and silicon carbide deposition.

Table 3-1. Factor levels for the design of experiments

	Factors			
	Temp	Scan Rate	Reagent Flow Time	Pressure
Experiments	ºC	in/min		torr
1	1200	0.1	2.5 minutes	300
2	1200	0.1	15 minutes	790
3	1200	0.2	2.5 minutes	790
4	1200	0.2	15 minutes	300
5	1350	0.1	2.5 minutes	790
6	1350	0.1	15 minutes	300
7	1350	0.2	2.5 minutes	300
8	1350	0.2	15 minutes	790
Midpoint	1300/1575	0.15	7 minutes	550

These experiments were replicated so that multiple samples were available for the various characterization methods. The SEM examination required two replicates for the cross sectional views. The transverse cross section was viewed as well as the longitudinal cross

section of the wall. These views permitted measurements of wall dimensions as well as inspection for any cracks. Replication also permitted varying whether carbon or silicon carbide was the first layer to be deposited. Outer morphology analysis with the SEM can be used for any of the above replicates. In all, 32 experimental runs were conducted for this investigation.

The walls were constructed by making 0.2 inch passes back and forth on the substrate. A single pass constitutes two layers due to the back and forth motion. Each deposited material was given three passes for six layers. The reagents were switched three times to produce four zones of alternating material deposits. The order of the experiments was randomized and the when a class of experiments was performed, all replicates were prepareded in the same experimental session. All procedures for chamber evacuation or other reagent handling were maintained the same for all classes of experiments, unless otherwise stated.

III.7. Reagent Delivery Calculations and Control

The MTS was delivered via a hydrogen carrier gas. The liquid MTS was stored in the vaporizer and hydrogen was metered inside to force out the gaseous MTS. The desired flowrate of MTS, deposition pressure, and molar reagent-to-carrier gas ratio was controlled through the hydrogen mass flow controllers.

Before the MTS can flow into the reaction chamber, the vaporizer must be slightly more pressurized than the chamber. The chamber was pressurized to the desired set point with the hydrogen dilution line. The vaporizer, with the down stream shut-off valve and throttling valve closed, was pressurized with the hydrogen carrier line. Once the vaporizer was slightly more pressurized, the shut-off valve was opened and the throttle valve was slowly opened so

that reagent flow began smoothly. Liquid MTS was corrosive and a rapid expulsion of MTS could put liquid in the gas lines.

Whenever possible the vaporizer was maintained just above atmospheric pressure to ensure its purity. For the cases where deposition occurs at 300 torr, the vaporizer was slowly brought to equilibrium with the chamber by slightly opening the throttle valve to slowly leak the MTS vapor.

When MTS was going to be used for deposition there are some basic caculations that govern the mass flow control. It is important to note that these calculations are based on steady state mass flow. However, once a trial experiment has been conducted there is enough hydrogen also in the bubbler so that steady state is acheved quickly when MTS is flowed into the chamber. The first step in the procedure is to measure the temperature of the MTS, which is done via the thermocouple on the bubbler. Since the vapor above the MTS is saturated, the vapor pressure of the gas is known by consulting thermodynamic charts. A chart of vapor pressure versus temperature is shown in Appendix A-1.

After selecting a pressure for the deposition chamber and pressurizing the vaporizer, the partial pressure of the hydrogen in the vaporizer is required. This quantity is simply the difference between the pressure of the vaporizer and the vapor pressure of MTS. The ratio of partial pressure of hydrogen to MTS is equivalent to the molar and volumetric flow ratio of the gases as they would exit the vaporizer. The mass flow controllers are calibrated in terms of sccm volumetric flow.

For a desired H_2:MTS molar ratio and a desired MTS volumetric flow rate, the flow rates for the hydrogen carrier line and dilution line are calculated using Equations 3-1 and 3-2.

$$\dot{V}_{MTS} = \frac{P_{v,MTS}}{P_{v,H_2,c}} * \dot{V}_{H_2,c} \qquad 3\text{-}1$$

$$\dot{V}_{H_2,d} = R * \dot{V}_{MTS} - \dot{V}_{H_2,c} \qquad 3\text{-}2$$

Here $\dot{V}$ refers to the volumetric flow rate and the subscripts denote whether the flow rate is from the hydrogen dilution line, hydrogen carrier line, or the MTS. P_v is the vapor pressure of the respective gasses and *R* is the molar ratio of hydrogen to MTS selected for deposition. A chart for hydrogen flowrates to produce 25 sccm volumetric flow for MTS with a 20:1 hydrogen to MTS ratio is provided in Appendix A-2. A table displays the values used for the experiments in A-3.

For this investigation the molar ratio used was 20:1 and the volumetric flowrate for MTS was 25 sccm. The volumetric flow rate can be converted to a mass flowrate for SiC that is available for deposition using Equation 3-3. The equation converts sccm to mole/min of MTS, then to g/min of MTS, and lastly into the grams available for silicon carbide deposition. This calculation is valid at 173 torr and 25ºC. At other conditions, another density conversion for moles to cm^3 is required. A chart for density calculations is displayed in Appendix A-4. These calculations were based on the ideal gas law. The ideal gas law stipulates that gases behave independently of each other. If deposition is carried out at 760 torr and a 25ºC temperature, the MTS thermodynamically behaves as if it were 173 torr, the vapor pressure of MTS at that temperature.

$$25\left(\frac{cm^3{}_{MTS}}{\min}\right)*\frac{1}{22{,}400}\left(\frac{mole}{cm^3{}_{MTS}}\right)*149.48\left(\frac{g_{MTS}}{mole}\right)*\frac{40.1}{149.48}\left(\frac{g_{SiC}}{g_{MTS}}\right)=0.0448\left(\frac{g_{SiC}}{\min}\right) \qquad 3\text{-}3$$

If deposition is 100% efficient then the 0.0448 g/min of silicon carbide could be deposited from MTS. After calculating how much silicon carbide is actually deposited in an experimental run an efficiency calculation can be made for the Georgia Tech LCVD system. Appendix A-5 provides a chart for the available silicon carbide versus temperature given an MTS flowrate of 25 sccm.

Methane mass flow rates are far simpler since methane is metered directly into the system. For this investigation, the molar ratio of methane to hydrogen was 3:1 with 300 sccm of methane. At standard atmospheric pressure and temperature, the density of methane is $6.612*10^{-4}$ g/cm^3. This would give 0.1984 g/min of methane. Since the weight percentage of carbon in methane is 75%, there are 0.1488 g/min of carbon available for deposition. Again, an efficiency calculation can be performed to characterize the Georgia Tech LCVD system. Appendix A-6 gives the table for methane's density relationship to pressure for a temperature of 22ºC. The temperature of the tanks and vaporizer are typically maintained around 22ºC and any variance produces a negligible effect on the density calculations.

III.8. Codeposition Experiments

Another set of composite experiments was performed to investigate structures composed solely of codeposited material, as opposed to single material laminates or functionally graded materials. For the process variables of pressure, temperature and scan rate, walls constructed by eight or six passes (16 or 12 layers) were constructed. In the case of fibers, pressure and temperature were investigated. Table 3-2 displays the factorial setup for codeposition. In the

wall experiment, pressure aliased temperature and scan rate. Midpoint experiments were also carried out for further investigation. For each experimental run, two walls and two fibers were produced. Walls and fibers were subjected to SEM analysis.

Table 3-2 Codeposition factorial experiment setup.

Wall	Temp	Pressure	Scan Rate
Experiments	ºC	torr	in/min
1	1200	790	0.1
2	1200	300	0.2
4	1350	300	0.1
7	1350	790	0.2
Fiber			
Experiments			
1	1200	790	
2	1200	300	
4	1350	300	
7	1350	790	
Wall Midpoint			
Experiments	1275	550	0.15
Fiber Midpoint			
Experiments	1275	550	

III.9. Stress Modeling

An attempt to model the stress with the program I-DEAS was attempted to no avail. The investigation was going to focus on how thermal stress due to cooling would result in stress levels that would initiate the cracking that has been observed. This was to be accomplished by modeling the thermal profile induced by the laser, then modeling the shrinkage of crystals formed at their local temperature and the associated stress from this deformation. A secondary effect that was going to be modeled was how the mismatch in thermal coefficients between silicon carbide and carbon would contribute to the thermal stress. However, the level of computing power required for the stress analysis was greater than the abilities of I-DEAS. ANSYS would be a better tool for analyzing the stress problem encountered in

LCVD. Such work would be useful for determining how the temperature profile can be manipulated to reduce stress.

CHAPTER IV

EXPERIMENTAL RESULTS

IV.1. Modifications to Experiments

IV.1.1. Thermal Imager

The limitations of the thermal imager greatly influenced the execution of the experiments and the results. Originally the plan was to investigate the influence of temperature on growth characteristics for a temperature range of 300ºC. The steep thermal gradients within the laser spot can produce localized temperatures that are outside the range of measurement for a particular thermal image filter. When an average temperature is calculated, these zones are given values for the maximum temperature. This source of error can be significant because the peak temperature can be 200ºC higher than what the imager is able of recording.

This error plays a significant role when measuring the average temperature with two different filters. Table 4.1 gives the temperature ranges that can be seen by the three filters used in the experiments.

Table 4.1 Thermal imager filter temperature ranges

Filter	Low Temperature ºC	High Temperature ºC
R1Z4.5	955	1255
R2Z4.5	1190	1600
R3Z4.5	1495	2170

When a laser spot is viewed with RZ14.5 and if an average temperature of 1400ºC is recorded, then the same laser spot can have a recorded average temperature of 1600ºC if

RZ24.5. The inconsistencies in average temperature recordings led to using only one filter (RZ24.5) for the experiments, to maintain the best possible consistency.

However, using only one filter restricted the temperature range that could be investigated. This relegated the experiments to an average temperature range of 1200 to 1350ºC. It was also intended to run the experiments for different temperature ranges for the respective gases. From past experience, it is known that silicon carbide deposition with MTS can be achieved at lower temperatures (~1050ºC) than carbon deposition from methane. Also, higher temperatures (~2000ºC) used to deposit carbon are not as thermodynamically favorable for silicon carbide deposition. It would have been desirable to have used different temperature ranges for the deposition of carbon and silicon carbide, however, using one filter to maintain consistency led to a smaller range to run experiments.

IV.1.2. Gas Jet Reagent Delivery

After four experiments were conducted it was decided that the use of the gas jet for reagent delivery was necessary. Using an optical microscope, significant volcano effects or trace deposits were discovered in these four previous experiments. Three of the remaining experiments were conducted with the gas jet engaged since the volcano effect was viewed to be the result of a diffusion limited process. The three experiments using the gas jet were runs 1, 4, 7 from Table 3-1. Two of these were low temperature experiments, and the other (#7) was performed at a high temperature set point. To compensate, the midpoint experiments were amended to using a temperature of 1325ºC. Since deposition rate and volcano effects had been an issue in previous experiments, the pressure was increased to 650 torr to provide

more reagent gas. The scan rate was kept at 0.15 in/min. The reagent flow time before the laser was turned on was set to 1.5 minutes.

When the gas jet was used in runs 1, 4, and 7 the reagent flow time was first switched to 1.5 minutes. Using the gas jet for deposition greatly changes the process for functionally graded materials. The gas jet delivers the reagent directly to the substrate so the incoming reagent begins to dominate in the deposition reaction sooner than the former reagent. Functionally graded material deposits with a gas jet are probably more feasible by altering the flow of both reagents during co-reagent flow as opposed to sequential reagent flow.

IV.1.3. Substrate Surface Polishing

The first experiment conducted (#3 from Table 3-1) used substrates that were polished with 220 grit and polished again with 400 grit. This experiment required higher levels of power than in previous work so it was deduced that the polished surface finish had enhanced the reflection of the laser radiation. Also, the AXQ substrate has a lower porosity than the SK-85, which enhances the conduction of heat away from the heated region on the substrate. AXQ was of interest because of its lower porosity. Lower porosity should provide a more consistent interaction between the substrate surface and the laser. However, the increased need for power led to the decision to only polish with 220 grit.

IV.2. Preliminary Results: Optical Microscope

Deposits were first examined with an optical microscope. Based upon the deposit shape, decisions on how to examine walls and fibers were made. Walls with uniform heights were suitable for facial cross sections for layering analysis. If a wall did not have too severe of a

volcano effect, a longitudinal cross section was made to view the planarity of the layers. Other walls were used for external examinations to obtain more geometric data on the deposit shape and volcano effects. Because of the significant number of volcano flaws, the investigation emphasized obtaining an understanding of how these flaws occur and identifying process conditions that minimize or eliminate the volcano effect.

Another flaw encountered was trace deposits, i.e. minimal deposition. These deposits required the maximum power to provide the highest temperature possible, but the achieved temperature was still below the desired temperature. Usually this phenomenon was encountered on the first attempted wall in a series of experiments, but this was not always true. Some experimental runs did not have any trace deposits (Experiments 1, 4, and 6). Trace deposits could be due to a "flaw" in the substrate surface that causes less heat to accumulate. Another possible suggestion is that the laser and optical assembly was not working in an appropriate manner and required some time to work in a suitable manner. This could be a reason why the flaws seemed to occur on the first run during an experiment.

IV.3. Thermal Imager Profile Testing

A follow-up experiment was conducted to study the laser profile for various cases. Since LCVD is a thermally driven process, there should be a strong correlation with deposition rate and temperature. The goal of the follow-up experiments was to record thermal images and match the images with cross-sectional profiles. The strongest point of interest was the examination of volcano peaks.

From the previously mentioned optical investigation, many of the walls had a volcano effect that basically resembles a valley running down the middle for the length of the wall.

By preparing a polished cross section across the volcano effect, the scanning electron microscope provides a clear and measurable image of the wall. The peaks of the deposit which straddle the valley can be matched to a corresponding temperature. Knowledge of this temperature provides ample guidance for future composite laminate experiments.

The follow-up experiments consisted of fabricating four composite walls for the process conditions of average temperature and scan rate for the set points listed in Table 3-1. Reagent flow time and pressure were considered to have a negligible significance in the formation of volcano effects and temperature distribution variances. The average temperature obviously has the greatest influence on the temperature profile. Scan rate can also have an effect on temperature profile, because a slower scan rate will allow the substrate and deposited material more time to absorb more thermal radiation.

The laminates consisted of only two layers of material. Either silicon carbide or carbon was deposited for a 0.2 inch pass for a total of 3 passes, followed by deposition of the other material for the same pass length and number of passes. During the deposition process, several temperature profiles were recorded for both carbon and silicon carbide. The gas jet was disabled for this experiment so that forced convection would not interfere with the temperature profile and because most prior experiments were conducted with the gas jet disengaged.

These thermal images were examined at the pixel level. Each pixel represents 3.5 μm and the temperature zones were accounted for how many pixels in width these colored temperature zones could be measured. The distance of a color band's distal and proximal edge to the center of the laser spot were easily calculated on an Excel spreadsheet.

The distance from the volcano center the deposit peak was measured via SEM. Assuming that the center of the laser spot corresponded with the center of the volcano, the measured distance from the volcano center to the deposit peak should correlate with the temperature band that produced the peak deposition rate. To ensure greater effectiveness of the measurements, both of the center-to-peak measurements were used as well as peak-to-peak measurements. Appendix A-7 quantifies the image analysis used for all follow-up experiments.

IV.4. Experimental Results

The experimental results of greatest interest are deposit shape, material composition, and deposit integrity. Overall, the deposits suffered from severe volcanoes and poor sequential material lamination, but there was some limited success. The lamination runs are discussed first, followed by the codeposition runs. After all of the experimental runs are discussed; trends in the data are presented in the following chapter. A summary of all measurements can be found in appendix A-8.

The nomenclature for the following trials signifies the trial run, the substrate, and the order of the wall deposition. 1-2-2 is the wall from the first trial listed in Table 3-1, on the second substrate and is the second wall deposited on that substrate. Walls listed as substrate 3 come from the codeposition experiments. Substrate 3 also uses F# to denote a fiber as opposed to a wall. For example 7-3-F2 refers to a fiber deposition.

IV.4.1. Laminated Deposition: Trial 1

The walls in Trial 1 were deposited using low temperature, low pressure, low scan rate, and the reagents were flowed to attempt functionally graded materials. The gas jet was also

engaged for this trial. During the trial, the temperature achieved a steady range near 1200ºC. The only issue that developed was at the last laser passes of runs 1-1-1 and 1-1-2, where the temperature began to fluctuate because the laser voltage needed to maintain the temperature was low (1.0 V). Adjustments made by the online control system would overcompensate periodically and cause the laser to shut down or induce temperatures significantly above the desired set point. The walls on the second substrate did not incur this problem.

Even though achieving and maintaining the desired temperature was not an obstacle for most of the trial, only a thin deposit was produced. The walls on substrate 1 were so scant that they were not even considered for SEM. The walls on substrate 2 faired better with at least some significant deposit. Run 1-2-2 yielded the best deposit from this trial and is shown in Figure 4-1.

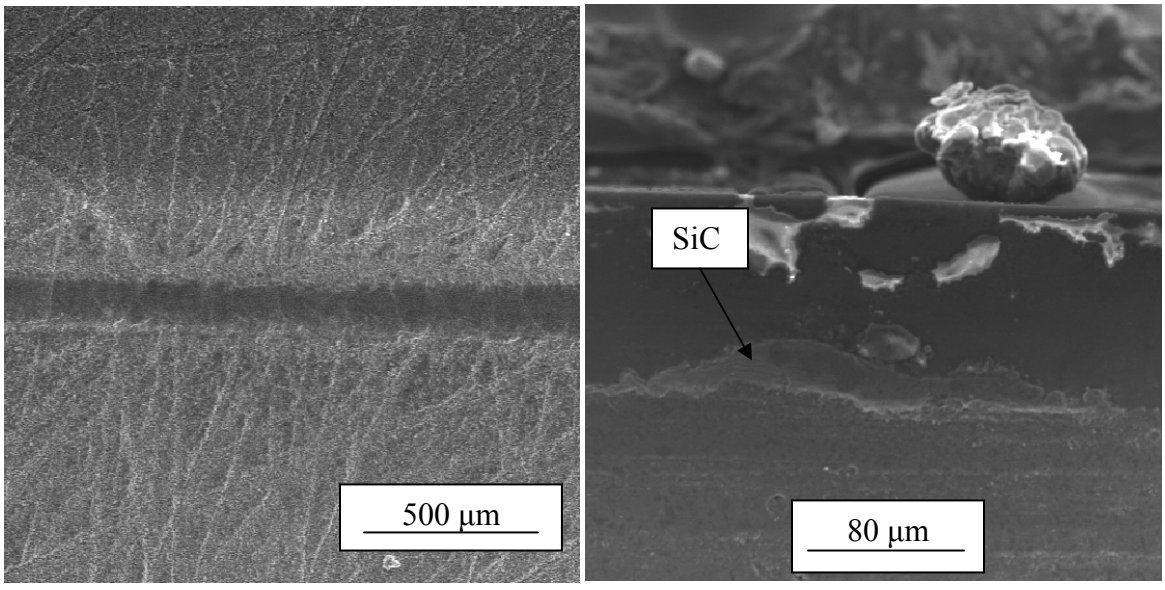

Figure 4-1A. (Left) An SEM micrograph of wall 1-2-2 showing the top of the deposit.

Figure 4-1B. (Right) An SEM micrograph of wall 1-2-2 showing the deposit's cross section.

The walls in from the second substrate had a smooth outer morphology compared to other trials. The volcano effect was very slight and hardly detectable from the outer view, except for the crack line running down the volcano middle as is normal for volcanoes. The wall began with carbon deposition, but there is no evidence of a carbon deposit. Apparently only silicon carbide deposition was achieved as noted by 4-1B. On the external view, it can be observed that the surface finish can have a negative impact on the deposit. Scratches on the surface interrupt the continuity of the deposit. From an integrity perspective, walls 1-2-1 and 1-2-2 have less cracking on the surface and the cross sectional view shows an intact deposit with minimal voids or separation between layers.

IV.4.2. Laminated Deposition: Trial 2

The goal of Trial 2 was to create walls at 1200ºC, 790 torr, a 0.1 in/min scan rate, and the reagents were purged for single material deposition. The gas jet was not used for this run. As in trial 1, there were some stability concerns in the final passes of the laser for all walls, except wall 2-1-1. Walls 2-1-1 and 2-2-1 exhibited very little deposit and were not examined with the SEM. SEM micrographs for walls 2-1-2 and 2-2-2 were attempted, but 2-1-2 could not be distinguished from the substrate and the 2-2-2 cross section was so thin that it could not be found.

Using the optical microscope, very thin deposits could be seen and the surface finish played a detrimental role in the experiment. The scratches would not accept any or very little deposit. The best deposit was 2-2-2, which was vertically jagged, but did not have a volcano effect. The jaggedness was related to the substrate scratches. Overall the scant deposits were

probably solely silicon carbide and their thinness made them indistinguishable from the substrate.

IV.4.3. Laminated Deposition: Trial 3

This trial attempted deposits at 1225ºC, a 0.25 in/min scan rate, functionally graded material, and a 790 torr chamber pressure. The gas jet was turned off and both substrates were polished with 220 and 400 grit sandpaper. The temperatures during the experiment were easily achieved and remained stable during the deposition process. The order of trials was randomly distributed and this trial was performed first.

Run 3-1-1 was a failed deposit attempt. For all the trials, the first deposit was more likely than all others to fail. This suggests that the laser itself could have issues with proper performance at the beginning of a run. Wall 3-1-2 was a very flat deposit with a grainy morphology. The volcano did not have any cracks running down the middle of it. The edges of the deposit were not uniform and had nodular deposits on them.

The cross section of wall 3-2-2 shows a symmetrical deposit. The deposit thickness was relatively uniform with a slight volcano effect. This wall exhibited a characteristic not seen in other walls. While both silicon carbide and carbon were deposited, the silicon carbide make up the bulk of the peaks, while the material under the volcano was carbon The reason for this occurrence is that carbon deposition is more favorable at lower temperatures found in the laser spot center and silicon carbide is more favored at the temperatures achieved in the laser spots outer half. The solution to the issues surrounding thermal gradients in addressed in the Recommendations chapter. The integrity of wall 3-2-2 was compromised, especially in the left peak which has significant delamination and cracks running through layers of carbon.

Wall 3-2-1 was examined using a cross section along the long axis of the deposit. Only two layers seem to have deposited, the first and second silicon carbide attempts. The deposit was started with silicon carbide, but apparently the carbon deposition attempt failed to materialize. The following layer of silicon carbide was successful, but the silicon carbide was poor in its integrity.

IV.4.4. Laminated Deposition: Trial 4

The fourth trial wan an attempt to grow walls at 1200ºC, a 0.2 in/min scan rate, single material materials, and at a pressure of 300 torr. The gas jet was used for this experiment. The operation of this experiment went according to plan. The temperature profiles did not have any problem achieving or maintaining 1200ºC for the duration of the four fabricated walls. The results of this trial were very similar to the results of Trial 1, which used the same conditions for temperature, gas jet, and pressure.

The only failed wall was run 4-2-1. All other attempts managed to produce some deposit. Wall 4-1-1 was a trace deposit that showed a smooth morphology, but only this carbon coating seems to have been deposited. Wall 4-1-2 shared the same results as the former wall.

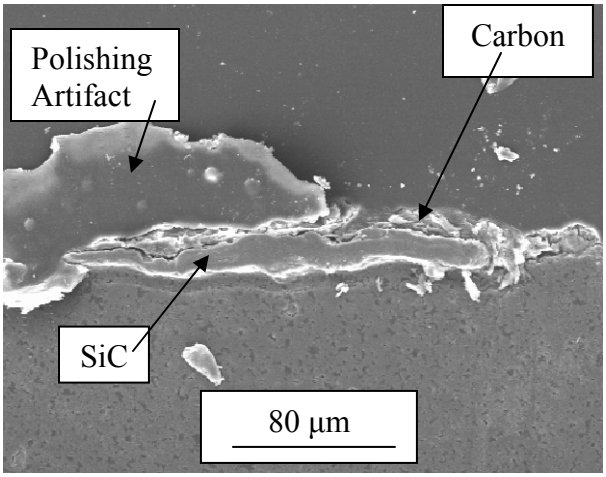

Figure 4-2. Cross sectional view of wall 4-2-2.

Perhaps a higher temperature was needed to initiate growth. Wall 4-2-2 successfully produced a laminated deposit of both silicon carbide and carbon. The first two material layers failed to yield a deposit, but the second carbon pass and the following silicon carbide succeeded.

The cross section in Figure 4-2 shows a carbon layer with a large crack on the left side with a silicon carbide layer on top. The silicon carbide is very flawed with cracking or pores throughout the layer. The whole layer had a very non homogenous look to it and this random growth pattern is probably undesirable with respect to mechanical properties. The positive benefit to this wall is that the thickness, especially for carbon, is relatively uniform compared to the other walls. It is possible that higher temperatures could increase the deposition rate without producing significant volcanoes.

IV.4.5. Laminated Deposition: Trial 5

Trial 5 sought to produce walls at 1450°C, a scan rate of 0.1 in/min, functionally graded materials, and a pressure of 790 torr. The gas jet was not used for this experiment. This was the second set of walls that was attempted. The optical investigations of the prior walls (Trial 3) suggested that the deposition rate was lower than expected. Since it was possible that the reflectivity of the substrate was causing the lower deposition rate, substrate 5-1 and all other substrates for experimental trials were polished with a 220 grit sand paper. 5-2 was polished with 220 grit and polished again with 400 grit sand paper.

The experiment began with wall 5-2-1 and the laser could only achieve a temperature of 1350°C for the first carbon run. The same result occurred for the second carbon run. The silicon carbide attempts could only produce temperatures of 1225°C. This all resulted in a

barely perceivable trace deposit. Wall 5-2-2 yielded better results even though the set point temperature was not achieved until the second carbon layer and third overall layer was attempted. The last layer, silicon carbide, was a failure in that the stages jumped to the wall's side, but the set point temperature of 1450°C was achieved.

Substrate 5-1, with the amended polishing procedure was able to produce more substantial deposits and this led to substrates for all other trials being polished in the same manner. Run 5-1-1 also had only slight trouble in achieving the set point temperature. The carbon passes could only achieve 1435°C and the silicon carbide achieved 1385°C. 5-1-1 did have a problem where the stages jumped during one of the passes, producing a volcano shaped deposit with a mound like deposit beside it.

Wall 5-2-2 is only two layers thick, beginning with carbon. A temperature of only 1375°C was achieved for the carbon layer and the silicon carbide was only able to a reach 1300°C. Despite similar problems with achieving set point temperature, it seems that a rougher surface is more desirable for achieving higher deposition rates. Although from previously discussed trials, the surface roughness should be uniform because the scratches do have a negative influence upon the morphology of the deposit.

While run 5-2-1 did not yield a deposit, run 5-2-2 yielded a respectable deposit despite the stage jumping. This wall is shown in Figure 4-3A. The carbon layer on top of the substrate has a very cauliflower like appearance. The flakes on either side of the wall are indicative of silicon carbide deposition, but ultimately have no major intrinsic importance. They do indicate that the first round of silicon carbide was successfully deposited.

The volcano is very narrow and steep, plus it is symmetrical about the long axis. Asymmetry has been noted in the deposits where the gas jet was engaged. This is one of the

few deposits where the volcano does not show cracks running down the middle of the volcano as depicted in Figure 4-3B. It is plausible that a narrower volcano should have less cracking as a deposit cools. When a deposit with a large volcano cools the peaks will tend to contract toward the centers of the peaks, placing a tensile stress on the volcano middle. If a deposit with a mound like deposit cools, the contraction acts toward the center so that the previous stress scenario does not occur. Wall 5-2-2 confirms this hypothesis since the volcano is not as prominent and the cracking did not occur.

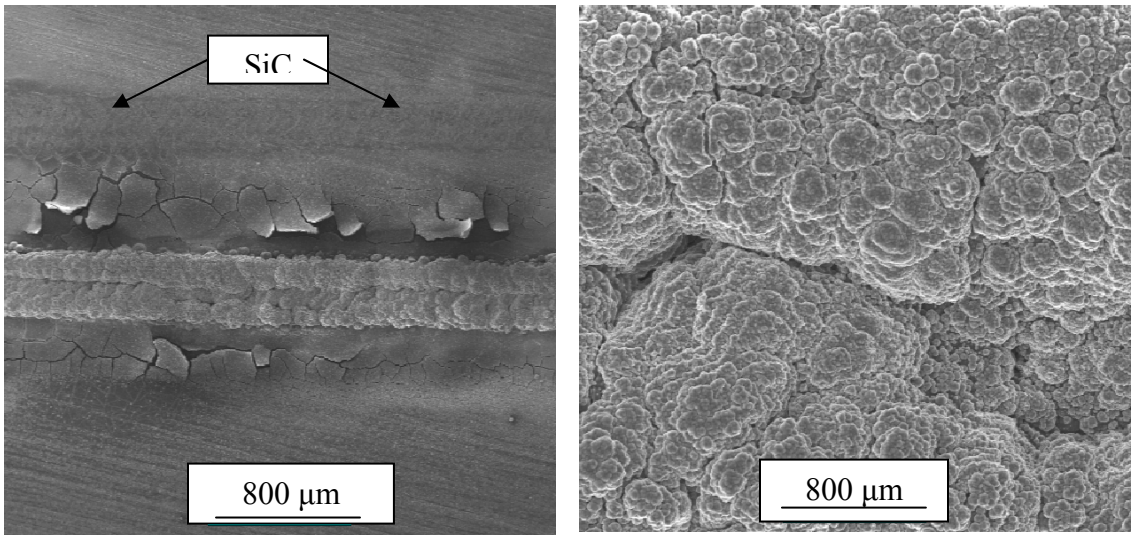

Figure 4-3A. (Left) External view of wall 5-2-2 with a trace SiC layer the besides the wall.

Figure 4-3B. (Right) Overhead view showing the narrow and steep volcano with no cracks.

Wall 5-1-1 showed some profitable results despite the stage jumping during the deposition. In fact it had the potential to be the best deposit of the whole series of experiments up to that point. A cross sectional view of the deposit is displayed in Figure 4-4. Wall 5-1-1 began with the alternating process with carbon. A relatively rectangular cross section of carbon can be seen in the right portion of Figure 4-4. On top of this is a layer of silicon carbide with a

very wide deposition zone that leans to the left and has a relatively small volcano effect. The following carbon layer leans even more to the left and at some point the deposition of carbon forms the base of the process flaw on the left. The final silicon carbide layer exudes a pronounced volcano with asymmetry along the longitudinal axis. The silicon carbide growth is out of control and this is probably attributable to the unorthodox growth initiated by the second carbon layer where the stage jump occurred.

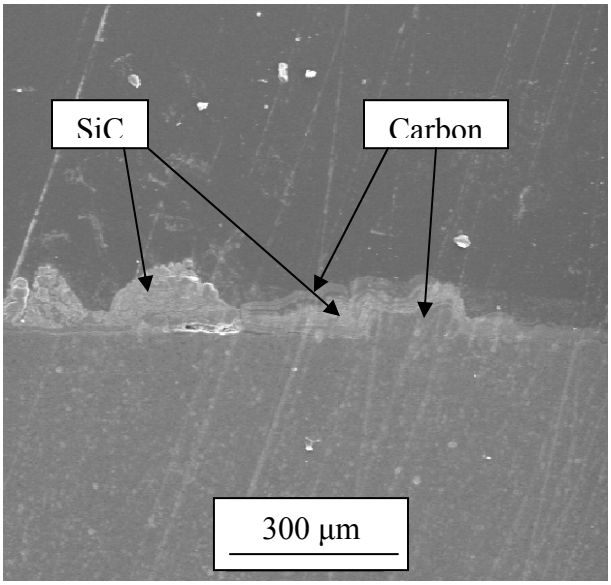

Figure 4-4. Transverse cross section view of wall 5-1-1 showing the original deposit (right) and the process flaw (left).

IV.4.6. Laminated Deposition: Trial 6

This trial attempted walls that were fabricated at 1425°C for carbon and 1375°C for silicon carbide, with a scan rate of 0.1 in/min, a chamber pressure of 300 torr, and purging the system to produce single materials in series. The gas jet was disengaged for this trial. During the experiment, the set point temperatures were achieved and maintained. This trial produced the most promising set of laminated structures as well as growth characteristics.

Wall 6-1-1 was analyzed by SEM for both external and transverse cross section views. Wall 6-1-1 was very asymmetrical along the longitudinal axis. The volcano effect was quite severe and broad, including cracks in the center. The lateral sides of the peaks have a nodular formation down the whole length. These formations are detrimental to the deposit quality because the nodular formations serve as stress risers and a smaller continuous cross section to support stress. Figure 4-5 shows the flaws of the nodular growth and the cracks in the volcano.

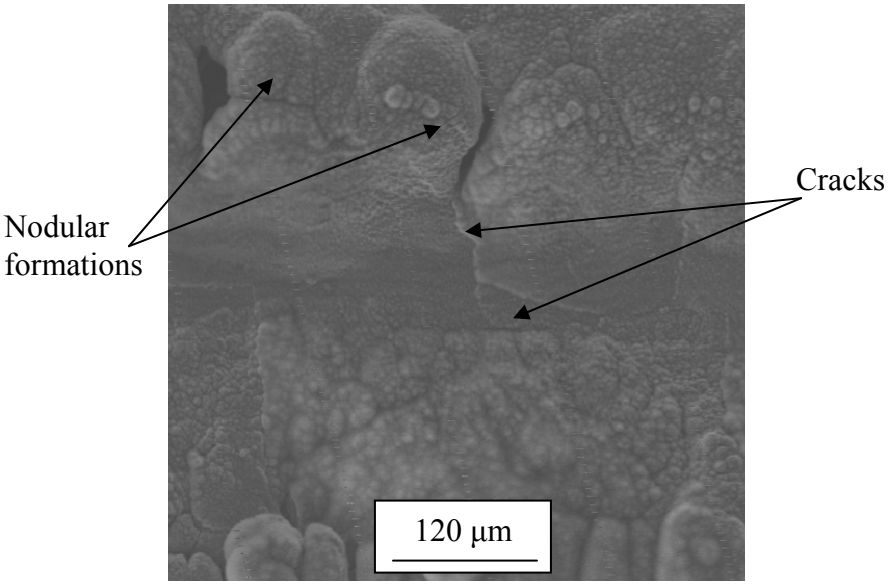

Figure 4-5. Wall 6-1-1 with nodular formations and volcano cracks.

From the cross sectional view, it was apparrent that the first carbon layer failed to materialize for wall 6-1-1. The two silicon carbide layers produced relatively strong yet uncontrolled deposition rates of silicon carbide. The second carbon layer could only be detected by a thin vein of carbon. The erratic growth of the silicon carbide is probably the reason for the asymmetric nature of the deposit. Through the thickness cracks are evident in

he left peak as shown in Figure 4-6. Altogether this deposit shows promise in producing laminates if greater process control can be attained.

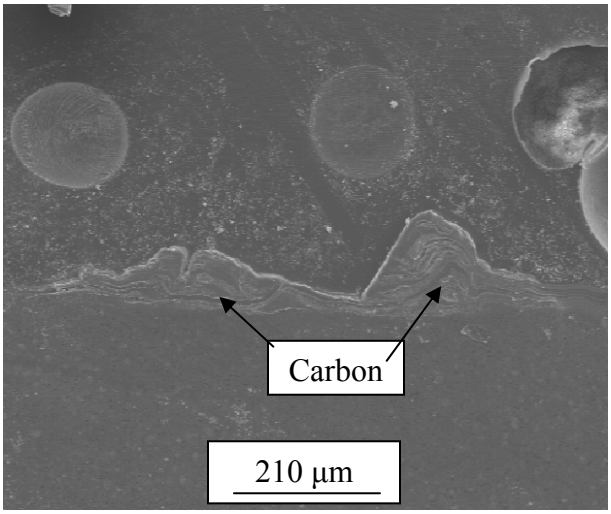

Figure 4-6. Transverse cross section of wall 6-1-2, largely a silicon carbide deposit with a carbon vein.

6-1-2 was analyzed both transversely and externally. This wall resembles 6-1-1 with even more pronounced nodular formations, asymmetry, and volcano cracks. Also, the

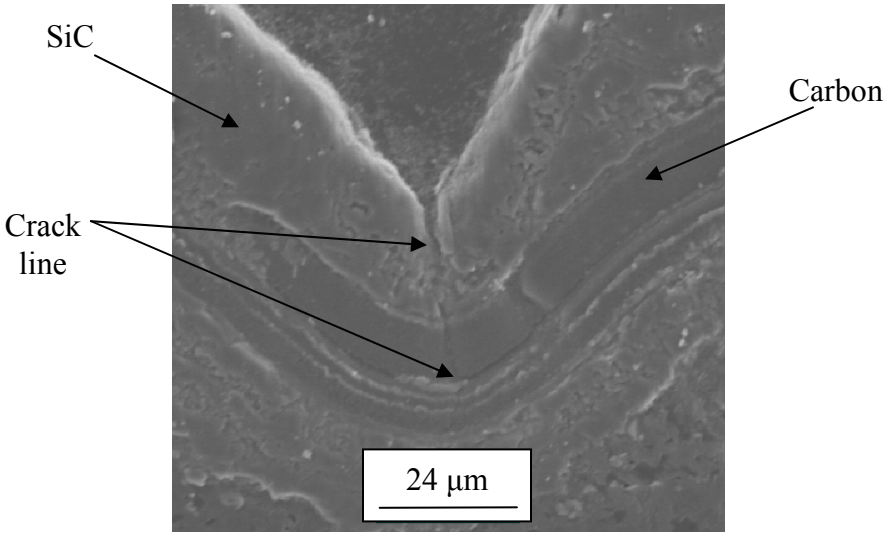

Figure 4-7. Through-the-thickness cracks in wall 6-1-2.

first layer of carbon failed to deposit, and the silicon carbide exhibited the same uncontrolled growth. Internally the structure suffers from delaminations and the volcano crack is very prominent as it cuts through the top silicon carbide layer and the vein of the carbon below. This crack is apparent in Figure 4-7.

Only the cross sectional view of wall 6-2-1 was examined with SEM. From this trial of experiments, this deposit exhibited the best shape. The cross section shape was very smooth and symmetrical, but the volcano effect was quite deep so that there was hardly any deposit in the center. Despite the smooth and symmetrical shape of wall 6-2-1, the deposit was even more silicon carbide weighted than its predecessors. The deposit began with silicon carbide and should have and internal layer and a top layer of carbon. The only trace of carbon was a small vein that separates the silicon carbide deposits. However, what the vein lacks in width, it did make up for with consistency. The vein was distinct and exists across the cross section. The silicon carbide is subject to voids, particularly at laser pass interfaces. The cross sections and EDS report can be viewed in Appendix A-11.

Wall 6-2-2 is definitely the most successful of the trials. Like wall 6-2-1, wall 6-2-2 shows a very symmetrical deposit. Wall 6-2-2 has an even more pronounced flaw in the volcano center. Not only does the center have a slower deposition rate, but the laser etched into the substrate by at least 30 μm. The center of the laser was so hot that it vaporized part of the substrate and filled the etched substrate with deposit. The success of this deposit lies in the laminated features that are distinctly exhibited. Silicon carbide was deposited followed with carbon. The cross section and EDS analyses are displayed in Appendix A-12. The silicon carbide suffers from cracks and delaminations in both sections. The carbon layers

have a very smooth texture absent of voids. Overall, Trial 6 shows some encouraging regions for silicon carbide deposition.

IV.4.7. Laminated Deposition: Trial 7

Trial 7 attempted to produce laminated walls where both materials were deposited at 1350°C, at a scan rate of 0.2 in/min, and at 300 torr chamber pressure. The reagents were coordinated to attempt functionally graded materials. The gas jet was engaged for this trial. With only one exception (7-2-1), all walls had trouble achieving the desired temperature. This could be due to the scan rate and perhaps the gas jet had detrimental effects on the temperature profiles. The attempt to produce wall 7-1-1 languished with temperatures at around 1225°C and only produced a barely noticeable deposit.

Run 7-1-2 had trouble achieving the set point temperature for only the first carbon layer. The deposit is very asymmetrical along the longitudinal axis. The gas jet clearly

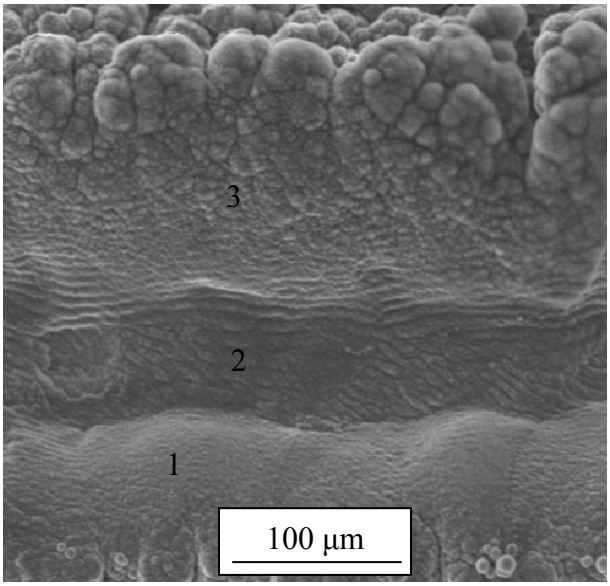

Figure 4-8. Overhead view of wall 7-1-2 exhibiting different morphologies.

enhanced the deposition of the distal peak. This pattern is clearly repeated in other trials and is illustrated later. Only the external morphology was examined by the SEM, there were no cross sections made. Wall 7-1-2 does have multiple textures as demonstrated in Figure 4-8.

The sections identified in the figure were examined by EDS. Section 1, is grainy in appearance and shows a composition of silicon carbide. The second section has a striated morphology with a composition of silicon carbide with excess silicon. Lastly, the third section has a very columnar appearance with composition of mostly silicon with some silicon carbide. For LCVD to produce superior deposits, it would be profitable for the microstructures to be homogenous throughout the deposit. This issue will be further addressed in the recommendations section.

Wall 7-2-1 despite being the only deposit that achieved and maintained its temperature for the duration of the experiment, suffered from low growth. In a cross sectional analysis, the small deposit is almost symmetric, despite the use of the gas jet. The distal peak seems to have nominal edge in deposition rate. The center is almost devoid of material and for the most part the deposit is only silicon carbide.

Wall 7-2-2 proved to be little better than wall 7-2-1. The gas jet effect on the distal peak is more pronounced. The structure had delaminations and voids, especially in the base layer of silicon carbide. Altogether, Trial 7 demonstrated the need for a more careful execution of the gas jet and the negative influence it can have on the deposit shape. Trial 7, while not a good region for both materials to be deposited from, does show room for improvement in silicon carbide. Better control over temperature profiles could lead to deposits that have a more rectangular cross section.

IV.4.8. Laminated Deposition: Trial 8

This trial was an attempt to fabricate walls where pure carbon and pure silicon carbide were deposited at 1350°C. The scan rate for the process was 0.2 in/min with a chamber pressure of 790 torr. The gas jet was disengaged for this experiment. Run 8-1-1 was not able to reach and maintain 1350°C until the third layer, which was also the second carbon layer. Run 8-2-2 did not reach 1350°C for just the first layer, which was carbon. Runs 8-2-1 and 8-2-2 did not have any process setbacks in the temperature profile.

Since wall 8-1-1 was only a trace deposit, it was not examined by SEM. Wall 8-1-2 was only given an external analysis with the SEM. The deposit itself was very substantial, comparatively. The nodule like growth (noted in trial 6) was also seen in this deposit, but to a lesser extent.

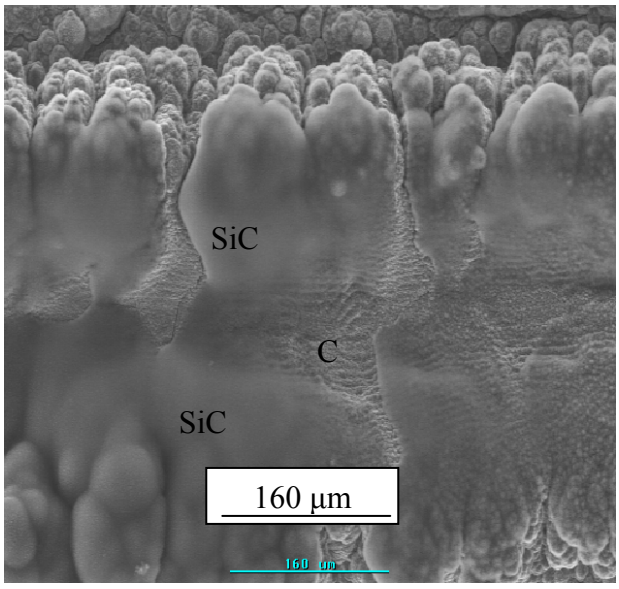

Figure 4-9. Volcano effect of wall 8-1-2 with stratified carbon microstructure and patchy deposits of silicon carbide.

The volcano was broad and deep, but the morphology that exists was what makes this deposit interesting. Both carbon and silicon carbide are exposed on top of the volcano surface. The carbon was seen in the stratified surface. This layered behavior likely is a result of carbon's hexagonal crystal structure, which gives carbon a plate like appearance. The silicon carbide shows up in smooth white patches. This was the first wall where this morphology was observed. The stratification, which can be seen in Figure 4-9 shows orderly growth characteristics and denotes that the experimental conditions have potential for further investigation.

Wall 8-2-1 was another substantial deposit in size and was examined using an external view and a cross sectional analysis. The sequential deposition began with silicon carbide and the content of the wall was largely just silicon carbide. From the external view the volcano had a columnar surface structure, typical of deposits of silicon carbide. Interestingly, the center did not exhibit cracking in the volcano. The volcano keeps narrowing until the top coating of silicon carbide ceases to bridge the sides of the volcano as shown in Figure 4-10.

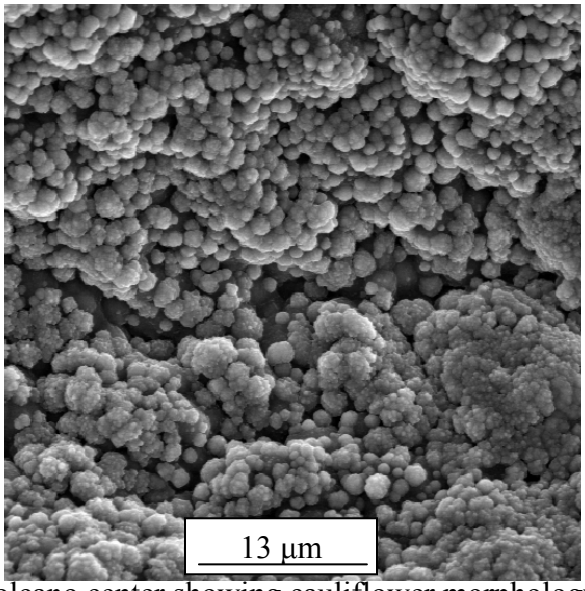

Figure 4-10. Volcano center showing cauliflower morphology.

Wall 8-2-1 had successful silicon carbide growth in both runs. Carbon, however, failed to produce substantial deposits. A trace 8 μm vein of carbon can be located in the middle of the deposit. The second carbon layer should have topped off the deposit, but there is no evidence of any carbon deposition from either the external or transverse cross section views. The transverse cross section view shows that the deposit leans to the left. With the gas jet disengaged and previous issues from the stages jumping during deposition, this leaning deposit could be a result of the stage path being slightly askew as the stage traverses its path. The deposit contained voids and cracking along the layers. Figures 4-11A and B respectively show both the cross section and a magnification of the carbon layer and the cracking in the deposit.

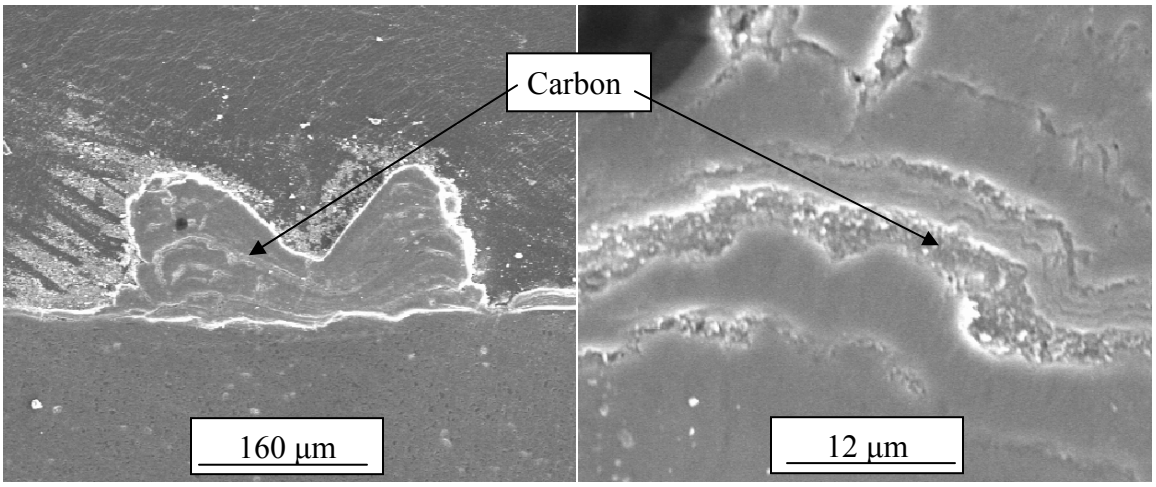

Figure 4-11A. (left) Wall 8-2-1 cross section of a silicon carbide deposit with a carbon vein.

Figure 4-11B. (right) Higher magnification of the voids and cracks near carbon vein.

Wall 8-2-2 was only examined externally. Even from the external view, both materials were successful in the deposition process. The volcano, seen in Figure 4-12 shows a number

of outer morphologies. White patches of silicon carbide, noticed in wall 8-1-2, also appeared in this deposit. The cauliflower morphology of silicon carbide is present and so too are the nodular growths, which are likely as detrimental to deposit quality as the volcano effect. Stratified carbon appears near the center of the volcano.

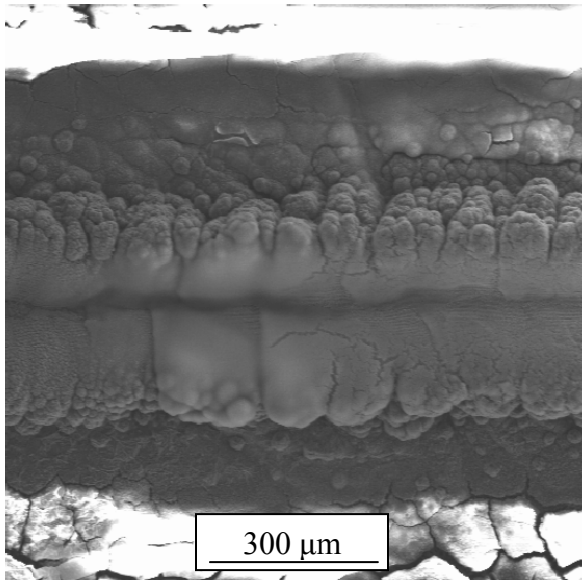

Figure 4-12. Volcano effect and multiple morphologies of wall 8-2-2.

IV.4.9. Laminated Deposition: Midpoint Trial

The midpoint trial was an attempt to investigate the process variables at their average values. However, since the gas jet was engaged with only one high temperature and no high pressures, the average temperature was biased on the high side at 1325°C and the pressure was biased at 690 torr. The scan rate was set to 0.15 in/min and the reagents were not purged and the new incoming reagents were flowed for 2.5 minutes. These laminates were constructed with only two layers. Silicon carbide was deposited to provide the base layer for two walls and carbon was deposited as the base layer for the other two walls.

Run MP-1-1 began with carbon, but the temperature only reached 1250°C. The silicon carbide deposition easily attainted 1325°C. From the cross sectional view, the carbon failed to deposit giving a solid silicon carbide wall. The distal peak in the deposit was larger, as has been the case with deposits produced with the gas jet. The volcano had a stratified appearance, but when magnified the stratification seem to be made of columnar mounds. When carbon appears stratified, hicher magnification shows a plate- like sub-structure. The stratification and the columnar mounds are shown in Figure 4-13A and B.

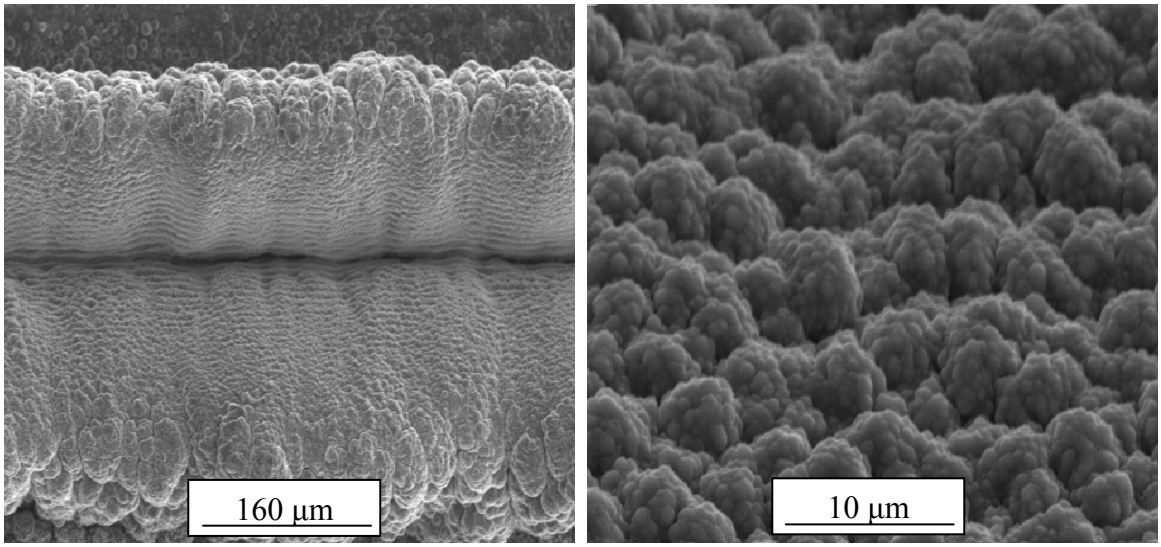

Figure 4-13A. (left) Stratifications in volcano for wall MP-1-1.

Figure 4-13B. (right) Globular substructure of the stratifications in wall MP-1-1.

Run MP-1-2 began with a successful silicon carbide run at 1325 °C. The control voltage range the laser required for this temperature profile was 4.5-6 V out of a 9 V available. The following carbon layer achieved only 1300°C with a control voltage of 8 V. Neither the external or transverse cross section SEM micrographs showed evidence of carbon deposition. It is unclear what caused the power requisite to be so different for silicon carbide and carbon

deposition. Since the deposition of silicon carbide is endothermic, the enthalpy of reaction is not thought to be a contributing factor. The silicon carbide appeared dense and contained fewer voids and cracks than most deposits.

Run MP-1-3 began with silicon carbide, but the end result produced a deposit similar to wall 8-1-2. The carbon run struggled to even achieve 1250°C with a control voltage of 8.5 V. The silicon carbide run easily achieved 1325°C with a 4 V control voltage. Again this deposit was solidly silicon carbide. From an external perspective, the deposit had a huge volcano effect, with practically no deposit in the middle. The transverse cross section view of the deposit revealed many large cracks, especially in the distal peak.

Run MP-2-1 finally achieved parity in the control voltage needed to maintain 1325°C. Both silicon carbide and the following carbon run required only 4 V. However the deposition produced mixed results. The external view showed different morphologies, where the volcano center exhibits a plate like stratification consistent with carbon. However, the transverse cross section showed a deposit with no evidence of carbon. Both these views are shown in Figure 4-14 A and B. The best explanation for this deposit is that carbon requires a significantly higher temperature for deposition. With peak temperatures above 1600°C in the volcano center, only a scant deposit of carbon could be achieved. From an integrity view, the deposit suffers from voids at sub-layer interfaces and cracks that originate from the outer edges of the deposit.

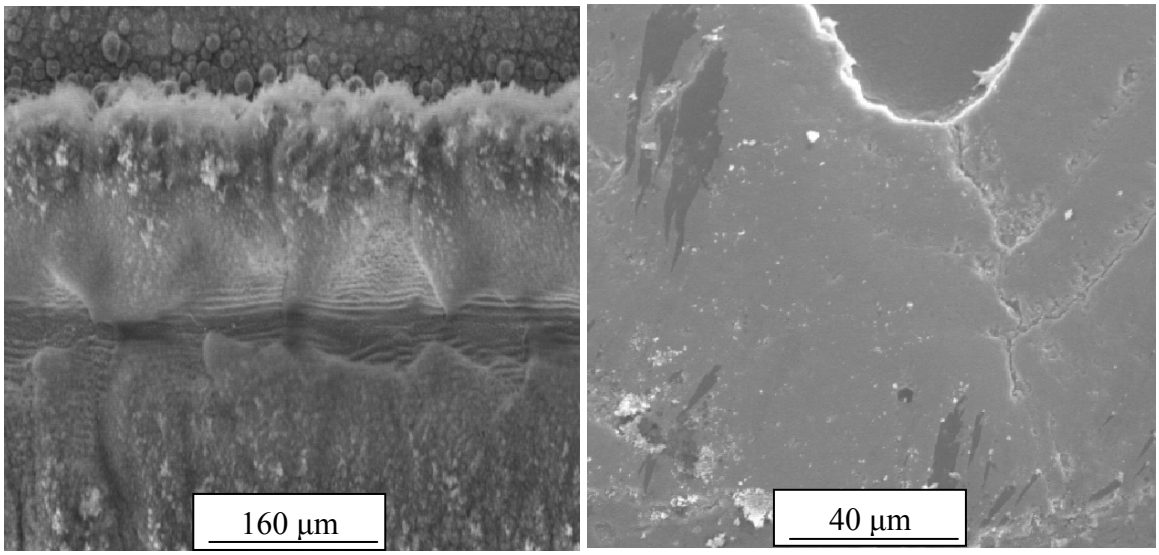

Figure 4-14A. (left) Volcano of wall MP-2-1 with evidence of carbon deposition in the volcano center.

Figure 4-14B. (right) Volcano center showing no evidence of carbon deposition.

Wall MP-2-2 is one of two walls where the goal was to produce single material walls. This silicon carbide wall was successfully grown, even with the gas jet disengaged. The only thing significant to note about this deposit is the presence of crack deflection, shown in Figure 4-15. The crack originates from the deposit edge and travels down the sub-layer interface. The crack reaches the volcano center, where thermal stresses have caused through-the-thickness cracks. Then the crack begins to run through the underlying layer, but as it reaches the next interface, the crack is deflected. After the deflection, the crack again penetrates another sub-layer, but the crack terminates half way through the layer. Here, the laminated process reveals an advantage where more energy is required to cause through-the-thickness cracks.

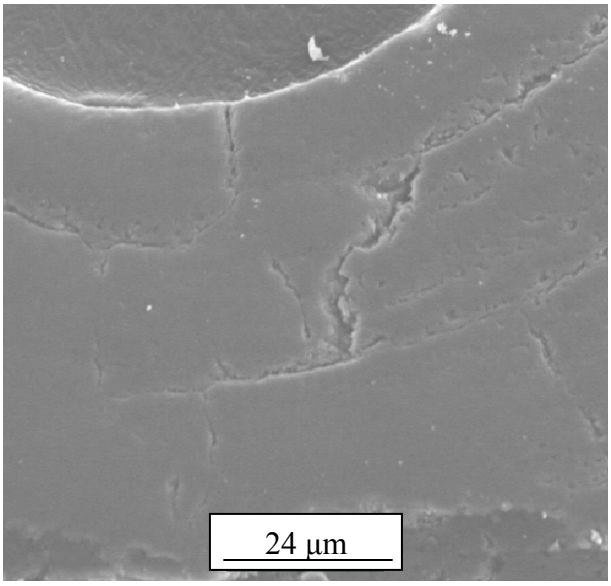

Figure 4-15. Crack deflection in wall MP2-2.

Wall MP-2-3 further exposed the weakness in carbon deposition. The temperature profile could only manage 1250-1300°C with a control voltage of 8 V. Only a bare trace deposit was observed. Overall the midpoint trial shows a promising condition for silicon carbide with improved process control. Carbon definitely needs a higher temperature distribution to begin substantial deposition.

IV.4.10. Codeposition: Trial 1

This codeposition experiment evaluated walls fabricated at 1200°C, in a 300 torr chamber pressure, and a scan rate of 0.2 in/min. Fibers were also investigated, but the only process variable setpoints used were the pressure and temperature previously mentioned. During this experiment the walls and fibers were fabricated at the set point temperatures.

Wall 1-3-1, which was constructed using 8 passes (16 sub-layers) left a small trace deposit that was examined by SEM externally. While an outline of a deposit seems to exist,

the scratches on the substrate surface suggest only a spotty and insignificant coating was achieved. The lines that mark what could be edges of the coating could have been produced by the laser singeing the substrate. Wall 1-3-2 was non existent and was not even analyzed.

The fiber runs yielded greater success. Fiber 1-3-F1 can be viewed in Appendix A-13. This was clearly the best of the codeposition fibers. A tricky aspect of producing fibers is that the control voltage required to maintain temperature is constantly decreasing. As the fiber grows, less power is needed because the fiber "bottlenecks" the heat transfer by way of conduction. In order to control the laser at lower powers, the control gain and signal correction had to be frequently adjusted. Growth was terminated when the adjustments could no longer be made safely. Otherwise a flare of power in the laser beam from the control loop might obliterate a section of the fiber because of thermal shock which has occurred from previous experience.

Fiber 1-3-F1 was grown for 16.5 minutes and reached a height or 538.4 μm. The promising attributes of this fiber is the lack of the volcano effect. While the tip is not without defect, the temperatures profile proved to be a appropriate region for testing. The major flaw of the fiber is that the base must have sustained a laser power flare and the fiber has to begin to growing again from the point of the defect. This explains the wedge-shaped deposit flaw seen in Appendix A-13.

From an integrity viewpoint, Fiber1-3-F1 is quite suspect. While no major cracks are seen, the nonhomogenous structure does not suggest an orderly deposition has taken place and the material is probably weak. EDS of the deposit showed the material to be carbon throughout the whole fiber. The other fiber, Fiber 1-3-F2, was a misshapen failure, so SEM was not performed.

IV.4.11. Codeposition: Trial 2

This codeposition experiment focused on walls that were to be grown at 1200°C, at a pressure of 790 torr, and a scan rate of 0.1 in/min. The fibers were grown at the same temperature and pressure. Temperature stability existed throughout the entire experiment. Fibers, 2-3-F1 and 2-3-F2 took 10 and 10.5 minutes respectively to complete deposition before the low laser control voltage became unstable. The gas jet was disengaged for this experiment.

Run 2-3-1 produced a deposit that was barely discernable and was not examined. Run 2-3-2 yielded a more substantial deposit, but the growth was not controlled and produced a peculiar morphology. The trace deposit was relatively smooth and marked with tubular growths. This was the only occurrence of this morphology and is shown in Figure 4-16.

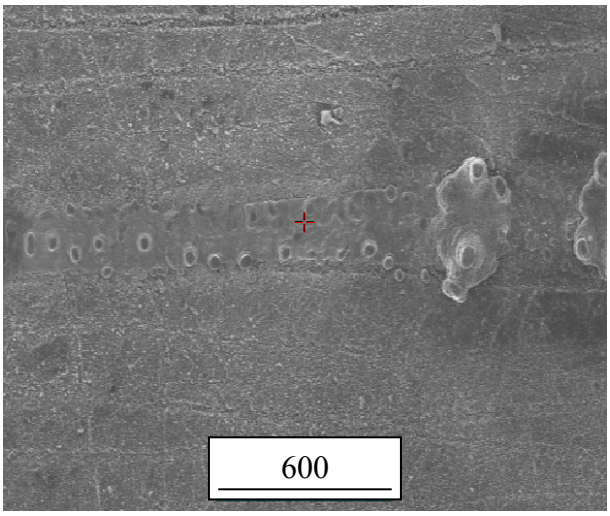

Figure 4-16. Wall 2-3-2 with tubular growths on trace deposit.

The fibers (2-3-F1 and 2-3-F2) in this experiment achieved mixed results. Both achieved deposits, but the growth was undisciplined. Figures 4-17A and B display fiber 2-3-F1 and

fiber 2-3-F2, respectively. Fiber 2-3-F1 was able to eventually achieve stable growth midway through the process while run 2-3-F2 failed to achieve the correction. Considering that previously mentioned fiber 1-3-F2 was also severely flawed and unexamined and that fiber 1-3-F1 had a poor fiber base, these four trials would suggest that beginning fiber deposition at a temperature of about 1200°C is not a high enough temperature to initiate controlled growth. Perhaps initiating growth at 1275°C, then lowering the temperature steadily to 1200°C would work better. With the thermal imager, observing fiber growth is a trivial matter and the procedure can be easily established.

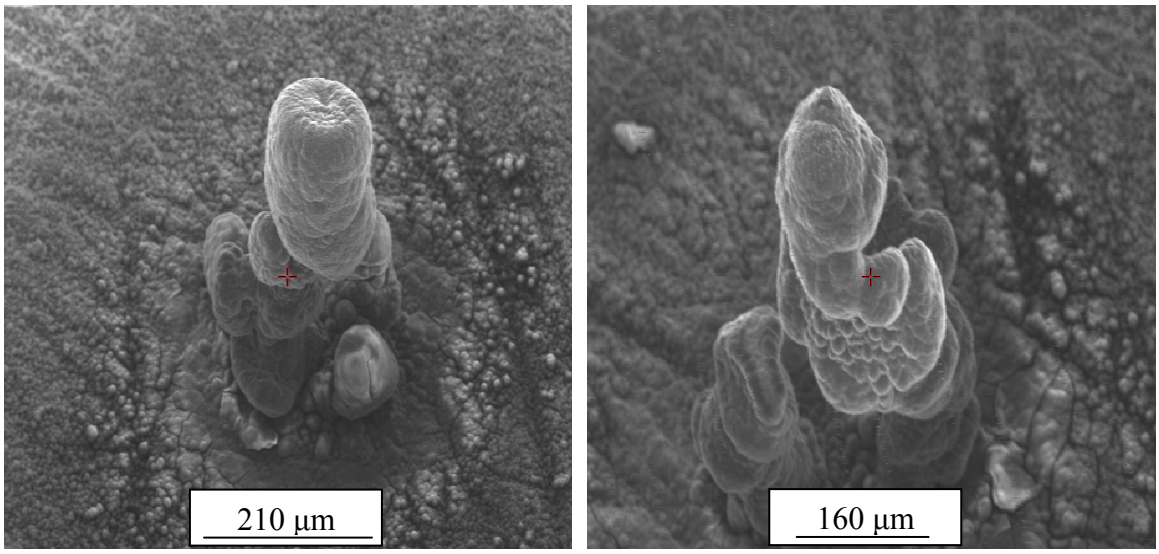

Figure 4-17A. (left) Fiber 2-3-F1 changes from out-of-order to controlled growth.

Figure 4-17B. (right) Fiber 2-3-F2 remains a flawed deposit throughout process.

Fiber 2-3-F1 was examined further since controlled growth was achieved. The top portion of the deposit exhibited a consistent radius and very little volcano effect. Figure 4-18 shows a micrograph taken at the tip of the fiber. This stalactite-like growth pattern was not

observed in other deposits. This pattern is probably of great use for fiber growth because it demonstrates an orderly growth in the direction of the fiber's long axis.

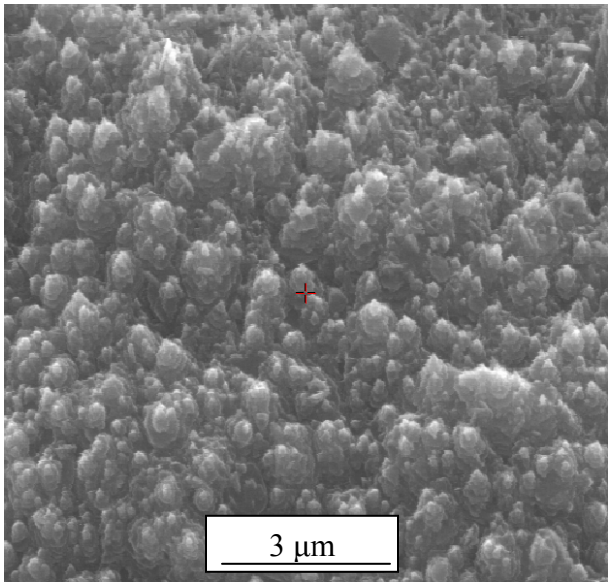

Figure 4-18. Stalactite growth from the tip of 2-3-F2.

IV.4.12. Codeposition: Trial 4

This trial attempted to produce walls at 1350°C in a chamber pressure of 300 torr, and 0.1 in/min scan rate. The fibers were grown at the same temperature and pressure. The gas jet was engaged for this experiment. During this process, both the two walls and two fibers were only able to achieve 1285°C.

Wall 4-3-1 was examined for transverse cross sectional and external views with the SEM. Both views show a very flat deposit with a volcano effect severe enough that no deposit existed in the center. The peaks have different shapes due to the gas jet enhancing the distal peak. Wall 4-3-2 was examined for the transverse cross section only. The same results occurred for this wall as was recorded for wall 4-3-1. Fiber 4-3-F1 produced no deposit and

the SEM micrograph shows "singed" carbon from the laser. The spot itself is well defined and has a diameter of 230 μm. Fiber 4-3-F2 was not examined with the SEM since the process yielded no identifiable results, when viewed with an optical microscope.

IV.4.13. Codeposition: Trial 7

Trial 7 produced the best walls of the codeposition experiments. These walls were grown at 1350°C, in a 790 torr chamber pressure, with a scan rate of 0.2 in/min. The fibers were grown at the same set point temperature and pressure. The gas jet was engaged for these experimental trials. Both walls and fibers achieved and maintained the set point temperature for the duration of the experiment. Fibers 7-3-F1 and F2 were grown for 5.85 and 5.4 minutes respectively, before growth was terminated when the control voltage became unstable.

Fiber 7-3-1 was examined for both internally and externally with an SEM and is displayed in Figure 4-19A and B. The wall is broad and flat and represents the best wall produced with only a small volcano effect. The top of the wall shows a morphology that is consistent across the width. This feature, coupled with the lesser volcano effect, demonstrates that the deposition conditions were more uniform across this wall than in other walls. This occurrence is desirable and uniform deposition conditions should be the primary goal of process control improvements.

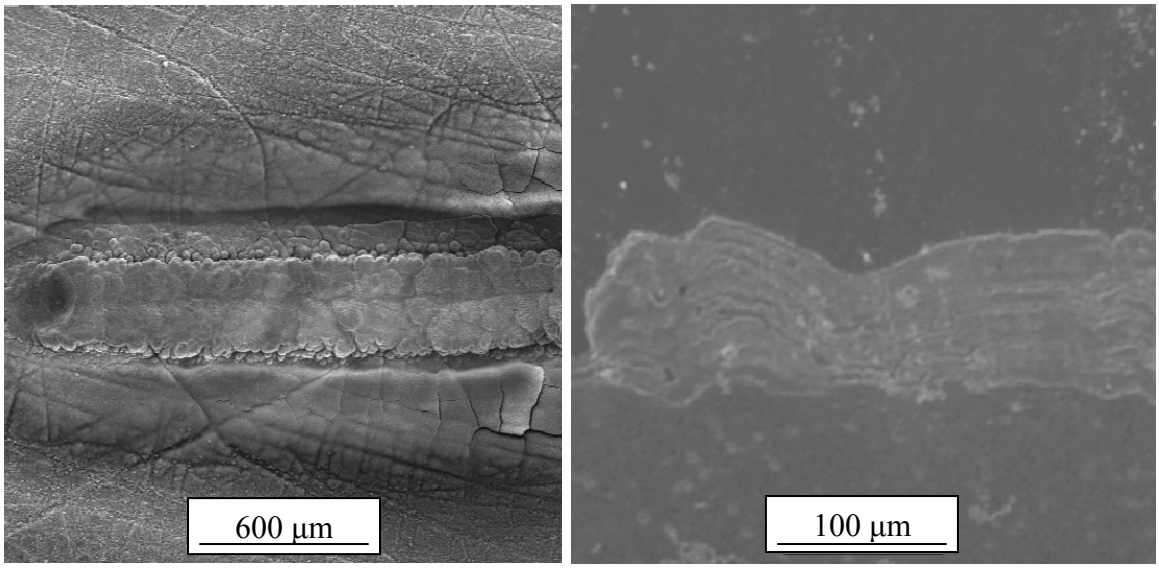

Figure 4-19A. (left) Plan view showing minimal volcano and consistent morphology in wall 7-3-1.

Figure 4-19B. (right) Transverse cross sectional view shows layered growth of wall 7-3-1.

Structurally the deposit is quite sound relative to other walls since there is an absence of cracks, voids, or delaminations. The interfaces between laser passes consist of softer material as indicated by the faster erosion of material during the polishing process. The passes of the laser are quite distinct and the thickness of material produced by each laser pass was 11 μm. Wall 7-3-2, while examined externally only, showed similar volcano and morphological traits.

Wall 7-3-1 was given other forms of SEM investigation. A backscattering electron method was used to produce micrographs where the image was influenced by the atomic weight of the elements present for the area exposed to the electron beam. Also carbon and

silicon maps were produced to show the density of the particular element present for an are under investigation. These images and maps are displayed in Appendix A-14.

The backscatter images show more distinctly the boundaries of the deposited material. The darker material is carbon while the lighter material is silicon carbide. The silicon and carbon maps graphically the regions of both. Since carbon is present in both deposits, this elements map is more uniform. The silicon map shows areas devoid of silicon which correspond the areas in the back scatter plots where carbon is found.

What is interesting is that the materials alternate in their deposition despite the fact that the incoming reagents are at a constant composition. To fabricate this wall, 12 laser passes were used, yet more than 12 layers is discernable. Even within one pass of the laser, both materials were deposited in an alternate fashion. The only suggestion for this occurrence is that the scan rate of 0.2 in/min is slow enough for the reagents to alternate deposition. Perhaps when one form of deposition is more favorable, the associated reagent is locally consumed to the point that the other material becomes more favorable. However the switch in deposition occurs over the same area still affected by the laser beam, hence multiple layers per laser pass.

Fiber 7-3-F1 was 560 μm in height and had a diameter of 370 μm. The volcano effect was quite pronounced and furthermore the gas jet caused the fiber to have a slanted growth in the direction of the reagent flow. Another flaw is that the base was malformed and could be due to a power flux in the laser beam. The depth of the volcano effect reaches approximately the top quarter of the fiber height. The volcano walls are relatively thin compared to the fiber diameter. One positive point about the volcano interior is that the surface has a layered appearance suggesting that the deposition conditions could support controlled growth if

uniformly applied. Figure 4-20A and B show the entire fiber and the deposit interior, respectively.

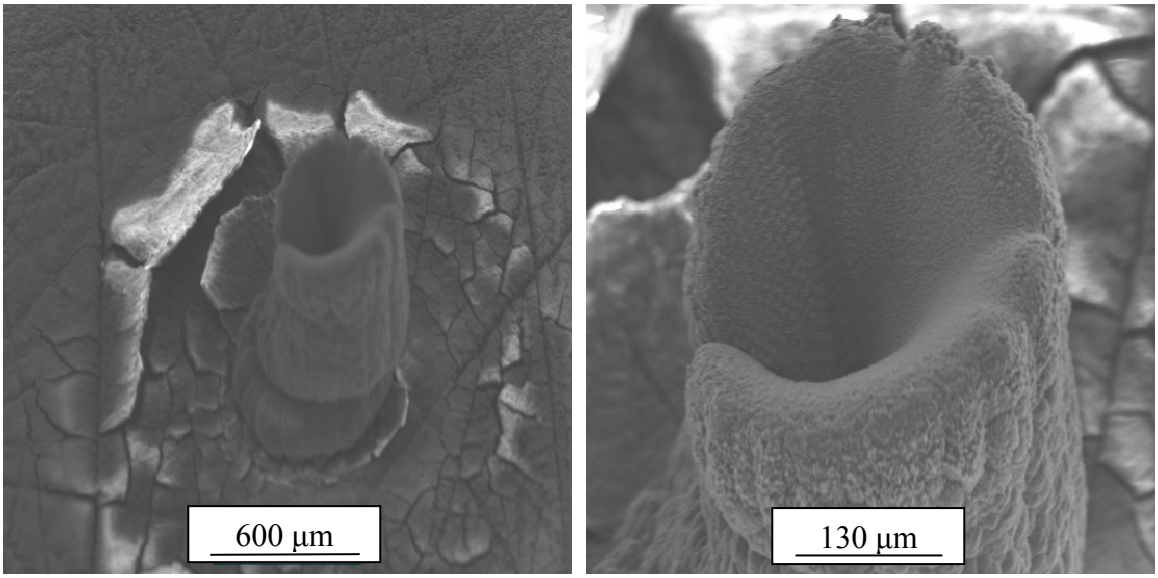

Figure 4-20A. (left) Fiber 7-3-F1 with pronounced volcano effect.

Figure 4-20B. (right) Stratified inner surface of volcano in fiber 7-3-F1.

Fiber 7-3-F2 had similar results to its predecessor. It did have one peculiar morphology that was observed in one other wall. Bristle-like growths emerged from the usual columnar

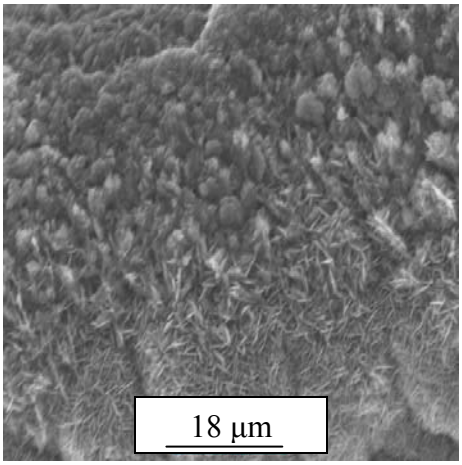

Figure 4-21. Bristle-like formations emerging from columnar morphology.

morphology as shown in Figure 4-21. Perhaps this morphology indicates a growth condition that are suitable for desired crystallinity. Regardless, this morphology should be noted because it is readily noticed and can be used an indicator for underlying properties once they are characterized. It is also interesting to note that the size of these bristle formations were around 1 μm in width

IV.3.14 Codeposition: Midpoint Trial.

The midpoint deposition experiments were conducted at 1325°C, in a chamber pressure of 650 torr, and the wall processed with a 0.15 in/min scan rate. The gas jet was engaged and the laser was made to undergo 6 back-and-forth passes. The walls struggled to achieve the set point temperature, but were eventually able to maintain 1325°C. The control voltage over the course of the experiment required 8.5 V to produce 1300°C and eventually tailed off to 3.5 V once the set point temperature was achieved. The fibers, MP-3-F1 and MP-3-F2, required 4.15 and 4.45 minutes, respectively, before the laser was shut off due to control instability. The micrographs and EDS data for all of these deposits can bee seen in Appendix A-15 through A-18.

Wall MP-3-1 was a substantial deposit with a lesser volcano effect than typical. The gas jet could be responsible for the volcano shape which tends to fluctuate along the length of the pass. Some areas have deep and narrow volcano shapes, while other areas are shallow, but exhibit cracks at the saddle of the volcano. The morphology also fluctuated between a columnar morphology and a stratified morphology along the long axis.

Internally, the deposit showed signs of delamination and cracking. Some layering was observable, but the areas of layering were where the deposit integrity was weakest. The area

near the mass centers of the peaks appears as a homogenous and non layered material and probably is the area of greatest strength. Wall MP-3-2 basically demonstrates the same qualities as its predecessor.

Fibers MP-3-F1 and MP-3-F2 were the best fibers produced in the codeposition experiments. The only significant flaw was the volcano effect that was less pronounced than for the fibers produced in Trial 7. The instability in the base growth still existed, but to a lesser extent than for the other fibers. The fibers leaned away from the source of the reagent flow. The growth along the long axis resulted in a consistent diameter of 400 μm. Despite the growth time being half of that for other successful fibers, the fibers grown at the midpoint condition achieved almost twice as much height, standing at 900 μm. The inner surface of the volcanoes was stratified but the stratifications had mixed substructures of plate-like and columnar growths. The tips of the fibers had bristle-like growths observed in Trial 7.

Internally, the deposits show weakness at the base with crack origins from the bottom surface. The cracks terminate where the fiber begins to assume a more orderly growth. The outer area of the fibers had a rough cross section and suggested that cooling leads to regions of high stress and cracked material. The internal area of the fiber exhibits a homogenous structure with some layering just above the base. Throughout the fiber's cross section, micropores were present.

CHAPTER V

DISCUSSION OF RESULTS AND CONCLUSIONS

Several measurements made on SEM deposits were used as a means of judging deposit quality. Images of the external view permitted obtaining measurements of deposit width and volcano crack width. The internal cross section views were used to catalogue width, peak-to-peak, peak-to-center, height, crack width, and layer thickness. Trends in the data which were identified by regression analysis aided in planning future designed experiments. Recommendations for modifications to the LCVD rapid prototyping system were also made.

V.1. Laminate Conducive Conditions

Laminates were produced in the trials and associated experimental conditions listed in Table 5.1. From the data listed in the table, the conditions that would most likely produce a laminated deposit would be functionally graded material walls fabricated at 1350ºC, with a scan rate of 0.2 in/min, in a chamber pressure of 790 torr, and no gas jet.

Table 5.1 Experiments which produced laminates.

Trial	Temperature	Scan Rate	RST	Pressure	Gas jet
3	Low	High	Single Material	High	Off
4	Low	High	FGM	Low	On
5	High	Low	Single Material	High	Off
6	High	Low	FGM	Low	Off
8	High	High	FGM	High	Off

These conditions correlate with Trial 8, which produced laminated deposits. The least successful conditions would most closely correspond to Trial 1, which would only differ by

the reagent switch time and also did not yield laminates.

Based on the assumptions made prior to the investigation, it would seem peculiar that the gas jet did not help produce laminates in Trials 2 and 7. Trial 2 could have been affected by the lower temperature setting which did inhibit growth. Trial 7 was marked with failures to achieve the higher set point temperature. The other oddity is that the faster scan rate was more effective. Perhaps Trial 3 was aided by the higher pressure, Trial 4 was aided by the gas jet, and Trial 6 was driven by the higher temperatures so that the scan rate was inconsequential. Overall, the temperature variable was found to be the most important variable in this research. Improved process control is certainly desired.

V.2. Variable Effects

V.2.1. Temperature

The temperature variable easily proved to be the most critical of all the process conditions. In laminate and codeposition trials, the average temperature directly increased the deposit height, width, peak-to-peak, and peak-to-center measurements. The temperature also had a positive effect on fibers by increasing the fiber diameter. Locally, the temperature and deposition rate have an exponential dependence, i.e. an Arrhenius relationship. The peaks of the deposits typically occur at local temperatures of approximately 1400ºC for silicon carbide. The peaks that occurred are more attributable to silicon carbide because bulk deposition with carbon was not as easily achieved as it was for silicon carbide. The peaks in carbon deposition are nothing more than carbon layers following the contours of the previously deposited silicon carbide.

No relationships between crack width and temperature or the existence of cracks and temperature were found. Typically any cracks that occurred were usually around a micrometer in width. Some deposits had minor crack densities and others had major crack densities, but both situations occurred regardless of temperature. While cracking and delamination were not strongly dependent on the average temperatures, it is reasonable to believe that temperature gradient and resulting non-uniform cooling and shrinkage have a significant influence on crack formation.

V.2.2. Scan Rate

The scan rate proved to be the second most important variable. A slower scan rate provides the reagents a greater residence time for deposition to occur. Also a slower scan rate exacerbates the volcano effect. While the volcano effect is likely produced by the temperature distribution, a slower scan rate permits increased growth to occur across the cross section. Since there are different local deposition rates across the width, the effects of these deposition rates are negatively exploited and the volcano becomes deeper. Also, a slower scan rate produces wider deposits for similar reasons; the lower growth rates on the lateral edges are allowed to grow more. Curiously, in the codepostion experiments, the scan rate had no noticeable effect. This could very well be an aberration of a series of experiments marked by mixed results.

A critical concern for LCVD is the ability to control the width of layers. If uniform temperature distribution can be achieved, the temperature will be the primary variable for controlling growth rates. Then, control with more finesse can be gained with adjustments in the scan rate.

V.2.3. Reagent Switch Time

The reagent switch time did not seem to have any primary effect on increasing the deposition rate or changing any other growth characteristics. However, when examining the measured data there was evidence that the reagent switch time and the temperature factors were interacting. At low temperatures, an attempt to produce functionally graded materials increased the deposit height, peak-to-peak, and peak-to-center values. For high temperature conditions, the single material attempts produced deposits with larger heights, peak-to-peak, and peak-to-center values. Overall, the reagent switch time factor is more of a finesse variable than the other factors and when better deposits are produced as a result of improved control over the other variables then attention should be focused on the reagent switch time.

V.2.4. Pressure

For laminate deposition, the pressure factor had no discernable primary or interaction effects. More effort should be placed on temperature and scan rate control before the pressure variable is examined further. For codeposition experiments, the pressure did seem to increase the deposition rate.

V.2.5. Gas jet

The gas jet was only used in three of the eight laminate trials. As a result, there were insufficient data, especially at high temperatures, to make a good assessment of its effect. The gas jet was used for three of the four codeposition trials. The gas jet did have a significant factor in increasing the deposit rate based on the difference in peak sizes. However, this might dictate that the gas jet should be used so that the gas flow is in the same plane as the laser and the same plane of the stage movement. This would ensure that the

flow is evenly distributed across along the deposit width. This would also require a mobile gas jet system, or multiple gas jets to cover multiple stage movements.

V.3. Regression Analysis

The deposit measurements were analyzed with linear regression to correlate deposit height, width, volcano effect, and overall deposit quality with processing conditions. The volcano effect and overall deposit quality are subjective measurements on an arbitrary value scale. For the volcano effect a value of 1 represents a severe volcano effect marked by little to no deposit in the center or etching of the substrate. A value of 2 represents a moderate volcano effect where the volcano shape maybe deep, but there was still significant deposition in the center. A value of 3 was awarded to deposits having a minor volcano. A value of 4 represents deposits with no volcano effect such that the deposits were flat or rounded. The same scale and value definitions was used for the overall deposit quality, however a value of 0 was assigned to deposits that were noted as trace deposits. A value of 4 was assigned to the best deposits. A detailed listing of each deposit's measurements is given in Appendix A-19. The ANOVA tables are displayed in Appendix A-20.

The ANOVA for the overall deposit quality indicated that, based on a significance of 10%, the only variable that had a meaningful role in determining the deposit quality was the reagent switch time. The negative coefficient obtained for this variable indicates that a mixed reagent atmosphere is advantageous for deposition. According to the analysis, the temperature variable was not significant in controlling deposit quality; however, the only condition that changes across the deposit width is the temperature profile. The ANOVA analysis is misleading for the temperature variable because this factor can cause deposit

flaws on both the high and low setting. Low temperatures are more likely to lead to trace deposits and high temperatures are more likely to produce severe volcanoes.

The volcano effect ANOVA yielded different results. The temperature and the reagent switch time factors were both significant. Decreasing the temperature reduced the effect of the volcano. This correlates with the idea that the high local temperatures in the center of the laser spot decreases the local deposition rates. If the average temperature is lower, then the area affected by detrimental temperatures is smaller, thus making the volcano effect less severe. The conclusions for the reagent switch time agree with the findings of the ANOVA of the overall deposit quality. A mixed atmosphere is advantageous for increasing deposit rate in the volcano.

For the dimensional ANOVA, the width and height were significantly affected by only the temperature variable. An increase in the average temperature increased the size of the region where the temperatures were high enough to cause appreciable deposition. As for the height dimension, increases in temperature increased the effective laser spot size and the most favorable temperature ranges for growth exist over a larger area. To some extent increasing the area favorable for deposition will naturally increase the deposit rate.

V.4. Overview

Overall, the temperature variable was found to be the most crucial variable. The next most important variable, in increasing the deposition rate, was a lower scan rate. The deposit shape was very much influenced by the gas jet; the reagent flow enhanced the size of the distal peak. The reagent switch time and the pressure variables had the least effect. Continued emphasis should be placed on establishing greater control over the temperature

and the scan rate. The recommendations made in the following chapter detail how improved control can be exercised, especially with regard to the temperature profile.

CHAPTER VI

RECOMMENDATIONS

The key issues revealed in this research are the necessity for better process control (repeatability) and the shortcoming of the Gaussian distributed laser power. The radial temperature distribution zone spanning approximately half of the laser spot proved to be counter productive for uniform material deposition. This is evident from the cross sectional volcano-like profiles and the changing morphology across the width of the substrate. The only variables that were changing across the width were the temperature profile and the reagent concentration. The former is believed to be the most important and was a cause for the latter . This chapter will present a solution to not only provide a more uniform temperature profile, but the suggestions should also increase the ability of Labview to control the average temperature. Also, a design of experiments to effectively utilize the proposed laser improvements is presented.

VI.1. Square Temperature Profile

VI.1.1. Concept

A square temperature profile should be a more suitable laser spot shape than the more circular Gaussian distribution. If this square flat profile can be achieved, the conditions in the deposition zone would become more uniform leading to comparable deposition rates across the laser spot. Increasing the uniformity of the deposition rate will produce deposits

that are not only more rectangular in their transverse cross section, but should also increase the repeatability of wall construction. While the current LCVD system has produced some walls of higher quality, the repeatability has remained an active concern.

V1.1.2. Implementation

The square-flat profile can be achieved with modest improvements to the current LCVD system. According to Lu,[32] a Gaussian laser can be split into 4 separate beams by a four-facet prism. These beams would be Gaussian in their power distribution and the centers of the beams would mark the four corners of a square. Via conduction and heat generation, the square area would be heated and the result would be nearly a square-flat temperature distribution at steady state. Square-flat temperature profiles are currently used in medical lasers, so the implementation of this improvement is readily feasible.

With the current LCVD equipment, modest efforts would be required to adjust the system. First, the appropriate prism must be acquired. The material of the prism must be transparent to the laser so that minimal power is absorbed by the prism. A zinc selenide prism would probably suffice. A holder can be designed to fit inside the chamber. This can be constructed from a wire frame and anchored into the chamber sides. Calculations would be required to verify the position of the prism so that the correct height is obtained to achieve the desired temperature distribution.

V1.1.3. Advantages

If the above equipment modification is successfully realized, the square-flat temperature profile will enable the thermal imager to calculate average temperatures with smaller

minimum/maximum temperature bands. The average temperatures will be more indicative of the conditions that are occurring at the laser spot. Greater reliability in the temperature measurement, should accompany even greater control over the laser. The deposits grown with this innovation will be exposed to less thermal stress because of the smaller thermal gradients in the deposition zone. Less cracking and delamination should be observed. The repeatability of future experimental work should be increased by using the square-flat temperature field. Currently, the literature does not show prior use of square-flat temperature profiles as a means of manipulating LCVD deposits.

VI.2. Design of Experiemtents.

VI.2.1. Laminated Composites

In order to utilize the square field laser, an appropriate design of experiments should be constructed to analyze process variables. The results of this thesis provided a good basis for design of subsequent tests. The atmospheric pressure process should be studied further since it yielded more deposit than runs made at lower pressures. The midpoint scan rate, 1.5 in/min, yielded the best deposits. The temperature should be varied systematically to evaluate changes in growth rate and deposit morphology over a range of temperatures. Two sets of experiments are desired; one with the gas jet on and one with it off. To maximize the use of the gas jet, the longitudinal axis of the wall and the gas jet should be appropriately aligned to ensure even growth.

From a material perspective, single deposits of both carbon and silicon carbide should be attempted first. The goal is to first learn material growth characteristics, then apply what has

been learned to the deposition of laminated composites. Table 6-1 details the experimental trials for each material. Each experimental trial should include 4 walls made with 8 laser passes in order to provide sufficient samples for multiple cross sections and mechanical tests. The post processing should focus on the testing and characterization discussed in Chapter III. This includes SEM analysis to measure layer thickness for individual laser passes, deposition rates, and deposition efficiency. It is also suggested that nano-indentation be used to characterize hardness and residual stresses.

Table 6-1. Initial design of experiments for square-field laser.

Material	Temp °C	Gas-Jet	Material	Temp °C	Gas-Jet
SiC	1150	On	C	1350	On
	1150	Off		1350	Off
	1250	On		1450	On
	1250	Off		1450	Off
	1350	On		1550	On
	1350	Off		1550	Off
	1450	On		1650	On
	1450	Off		1650	Off

The goal of the next phase of experimentation should be to understand the relationship of the scan rate with growth characteristics. Single material deposits using the same chamber pressure should be fabricated at the more profitable temperature regions with scan rate adjusted at levels from 0.5 to 2.5 in/min in 0.5 in/min increments. A decision on how to use the gas jet should be made based on the results of prior experiments. The same post processing of walls should apply.

The last single material test would focus on the use of the gas jet to change the growth characteristics. Hopefully, the first experiment will conclude that the gas jet played a significant factor in positively influencing the growth characteristics and lead to adjustments

that will provide uniform enhancement across the deposit. The best deposit conditions based upon growth characteristics and mechanical analysis from the previous temperature and scan rate experiments should be used. The gas jet flow rate should be varied from 0 to 2000 sccm using 400 sccm increments. Again, the same post processing should be used to quantify experimental results.

Now that substantial experimental characterization has been accumulated for both materials, this characterization should be applied to producing quality deposits. Prime temperatures and scan rates should be known for each material and layer control by means of the gas jet might be realizable. The laminates should be constructed first from single material with full purges of the chamber before initiating a change in reagents. Producing functionally graded materials is a finesse refinement of the process and should wait until mastering the deposition of single material laminated deposits. The number of passes for each material can be selected at that time, but it would be advisable to make the walls from four separate material layers; two from each reagent. The gas jet should be the only process variable that is changing. At this point, further planning of composite experiments should be guided by the results of these experiments. The experiments will provide not only information on deposit characteristics, but will also provide other unforeseeable insight on how to improve the lamination process.

VI.2.2. Codeposition

For the codposition of carbon and silicon carbide, the following recommended design of experiments is suggested. The walls should be investigated in a similar manner as the laminated composite walls. For a scan rate of 0.15 in/min and atmospheric pressure, the

reagents should be metered in equal mass flow rates. The average temperature should be varied from 1150 to 1650ºC at every 100ºC intervals. For each temperature set point a trial with multiple replicates should be made for the gas jet being engaged and disengaged. The analysis of these deposits should be the same as employed in the laminate trials.

The next series of trials should use temperatures that were considered more successful for deposition. The scan rate should be varied from 0.5 to 2.5 in/min at 0.5 in/min intervals. Each trial should be processed with the gas jet engaged and disengaged. The chamber pressure should be held at atmospheric pressure. Another round of characterization will occur to verify the best zones of deposition based on material properties, geometry, morphology, and integrity. Lastly a series of experiments using the most promising condition should be performed with variance in the gas jet flowrate as noted in the laminate deposit design of experiments. The gas jet could possibly be the tool to achieve control over layer thickness more readily than other variables, without affecting thermal stress or mechanical properties. Eventually manipulation of the reagent composition can lead to further investigations of material properties and deposition performance.

The codeposition fibers are simpler to investigate. The first suggested series of experiments requires atmospheric pressure and equivalent mass flow of reagents. The temperature should be varied in the same manner as the codeposition wall counter parts. Once the fibers are examined (including beam bending tests), promising temperature regions will be known. Using these temperature set points, the vertical stage can be adjusted to investigate the effect it might have upon the growth characteristics and mechanical properties. Lastly, once the desirable set points for temperature and vertical scan rate are known, the mass flow rate can be adjusted to investigate if the fiber's growth can be

controlled with finesse. All of the suggested experiments should be processed with multiple replicates to verify repeatability.

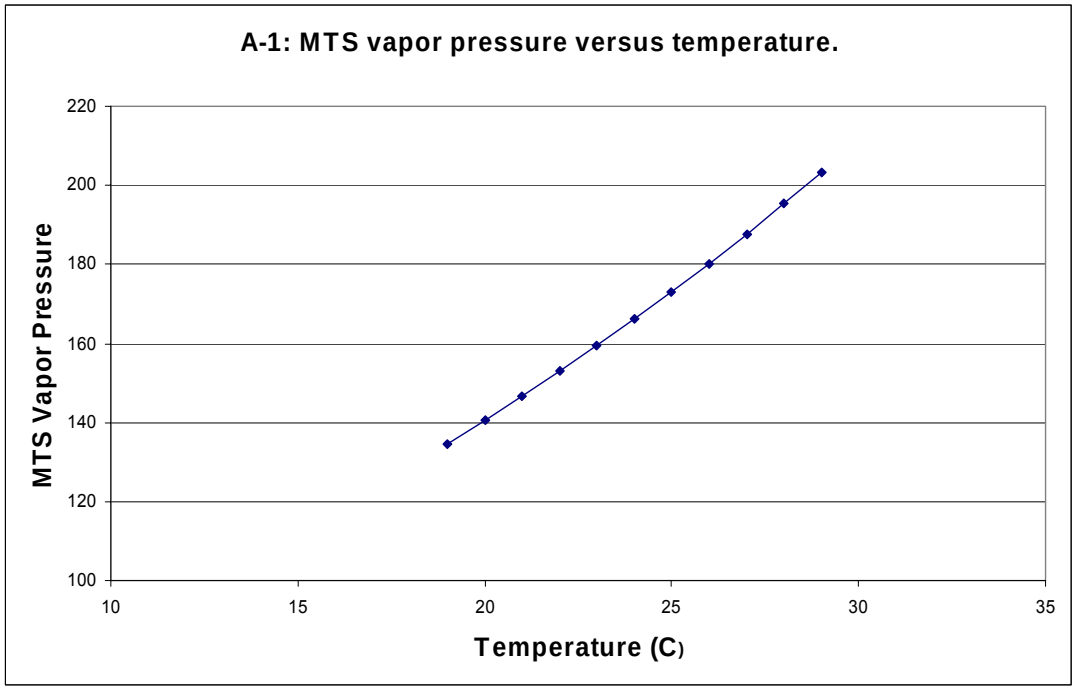

Temperature (ºC)	19	20	21	22	23	24	25	26	27	28	29
Pressure (torr)	134.7	140.6	146.8	152.9	159.4	166.1	173.0	180.2	188	195.3	203.2

A-2: Hydrogen flowrates to obain 25 sccm MTS flowrate at a 20:1 hydrogen to MTS molar ratio.

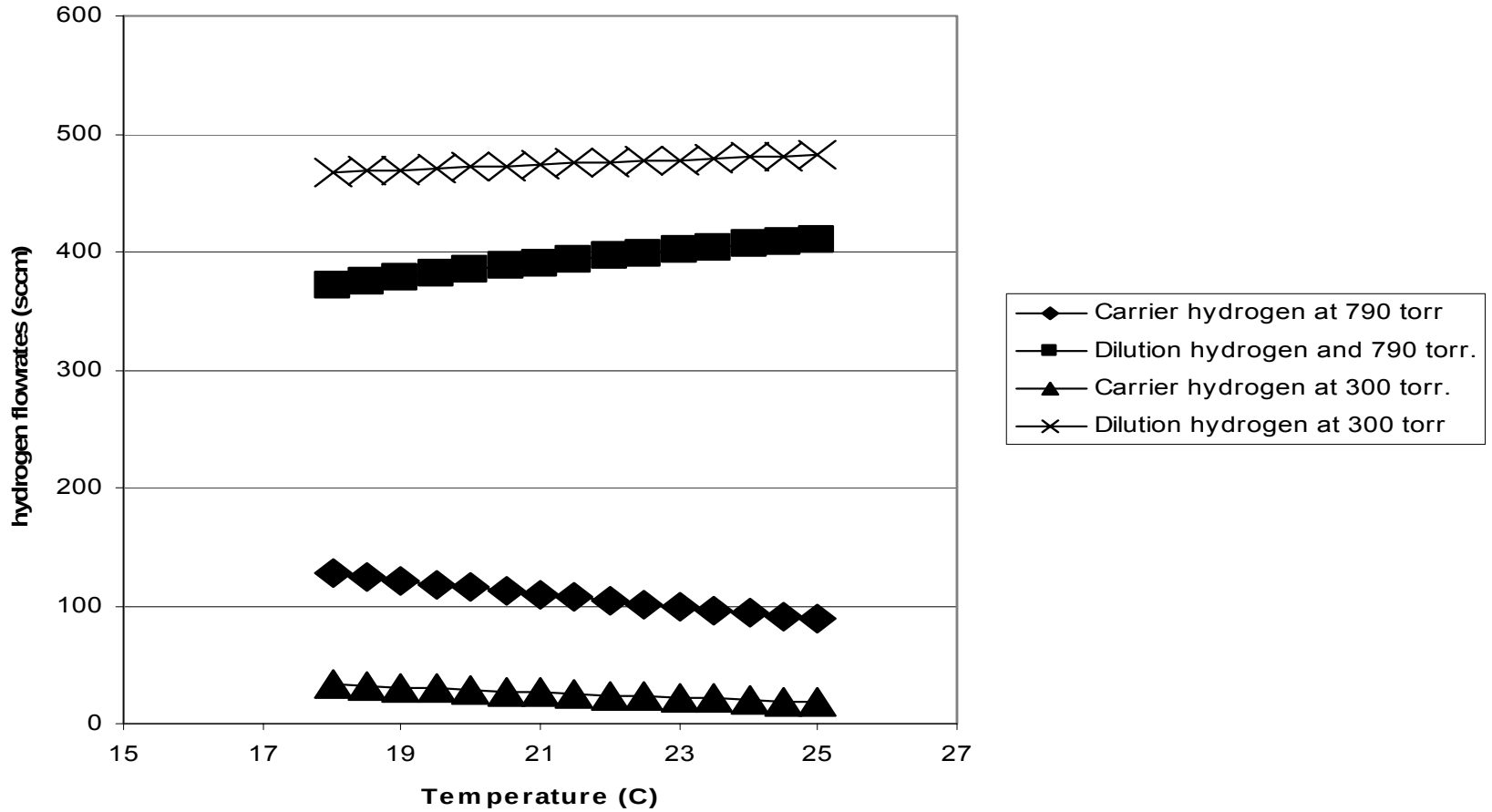

	A-3: Hydrogen mass flowrates used for associated vaporizer temperatures and pressures.														
MTS volumetric flowrate = 25 sccm															
Hydrogen:MTS ratio = 20:1															
Vaporizer Pressure = 300 tor															
Temperature (ºC)	18	18.5	19	19.5	20	20.5	21	21.5	22	22.5	23	23.5	24	24.5	25
Carrier Hydrogen Flowrate (sccm)	128	125	122	118	115	112	110	107	104	101	99	96	94	91	89
Dilution Hydrogen Flowrate (sccm)	372	375	378	382	385	388	390	393	396	399	401	404	406	409	411
Vaporizer Pressure = 790 tor															
Temperature (ºC)	18	18.5	19	19.5	20	20.5	21	21.5	22	22.5	23	23.5	24	24.5	25
Carrier Hydrogen Flowrate (sccm)	33	32	31	29	28	27	26	25	24	23	22	21	20	19	18
Dilution Hydrogen Flowrate (sccm)	467	468	469	471	472	473	474	475	476	477	478	479	480	481	482
	See Equations 3-1 and 3-2 for derivation of values.														

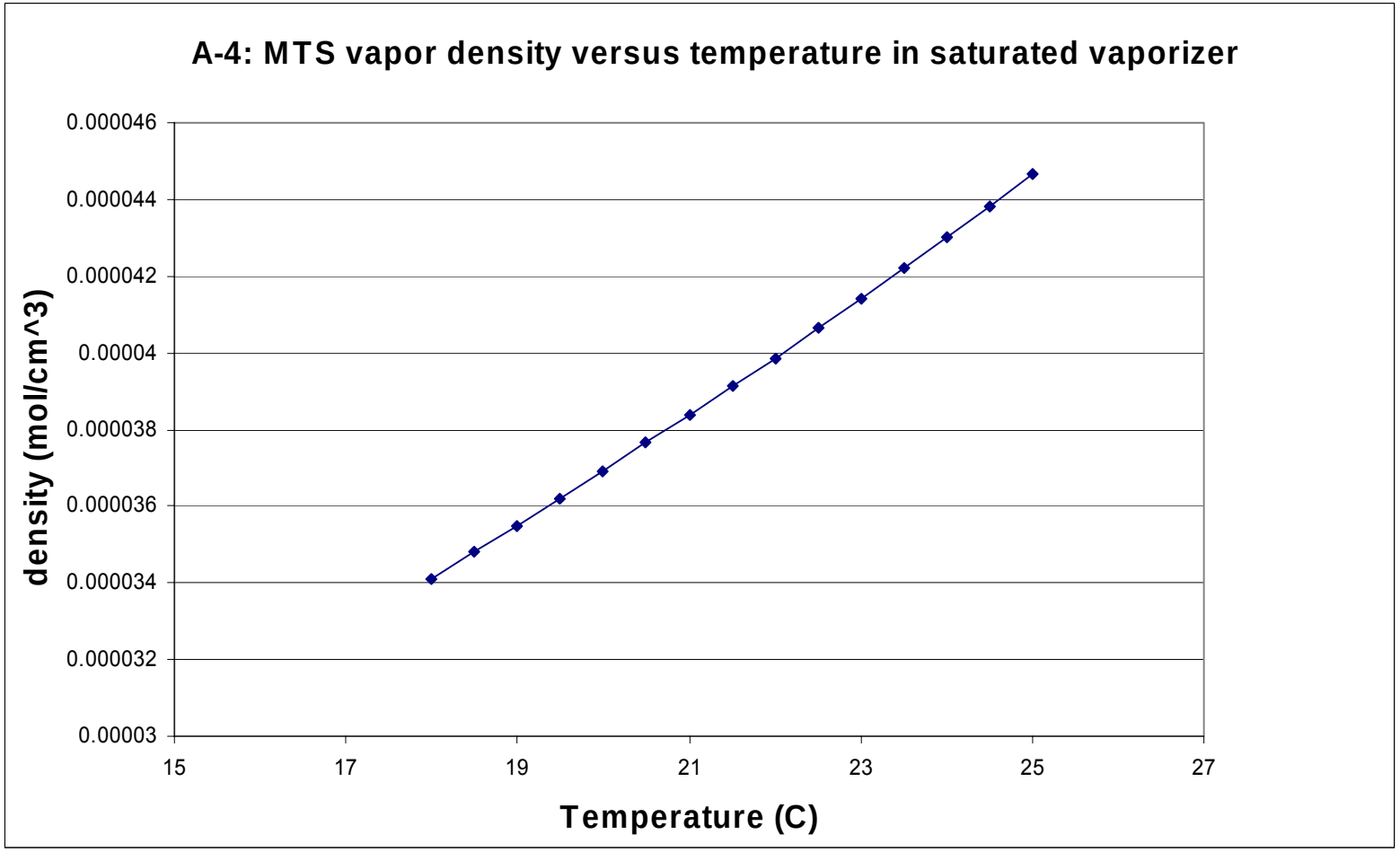

Temperature (ºC)	18	19	20	21	22	23	24	25
Mass (g)	3.41E-05	3.55E-05	3.69E-05	3.84E-05	0.0000	4.14E-05	4.3E-05	4.38E-05

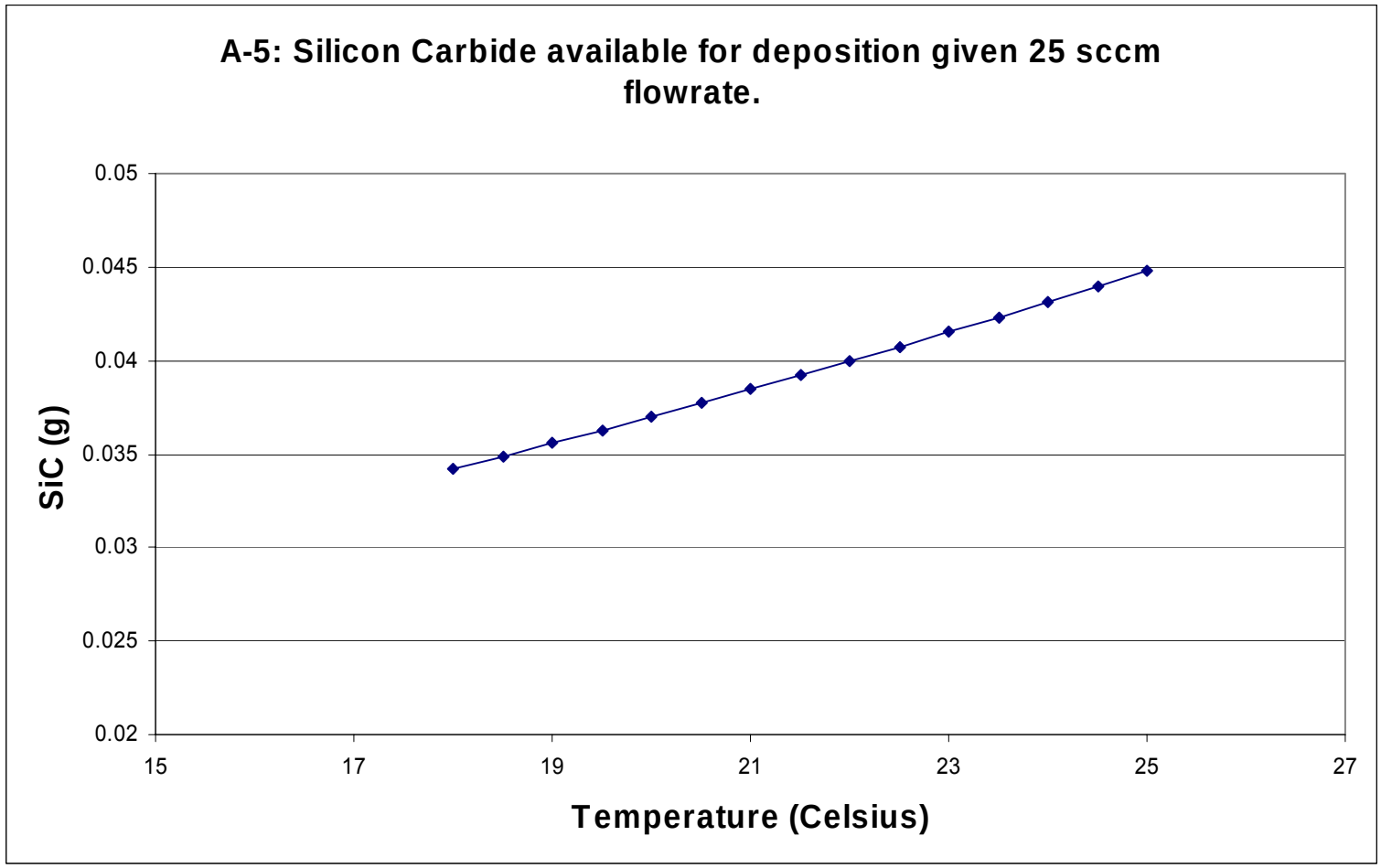

Temperature (ºC)	18	19	20	21	22	23	24	25
Mass (g)	0.0342	0.0356	0.037	0.0385	0.0400	0.0415	0.0431	0.0448

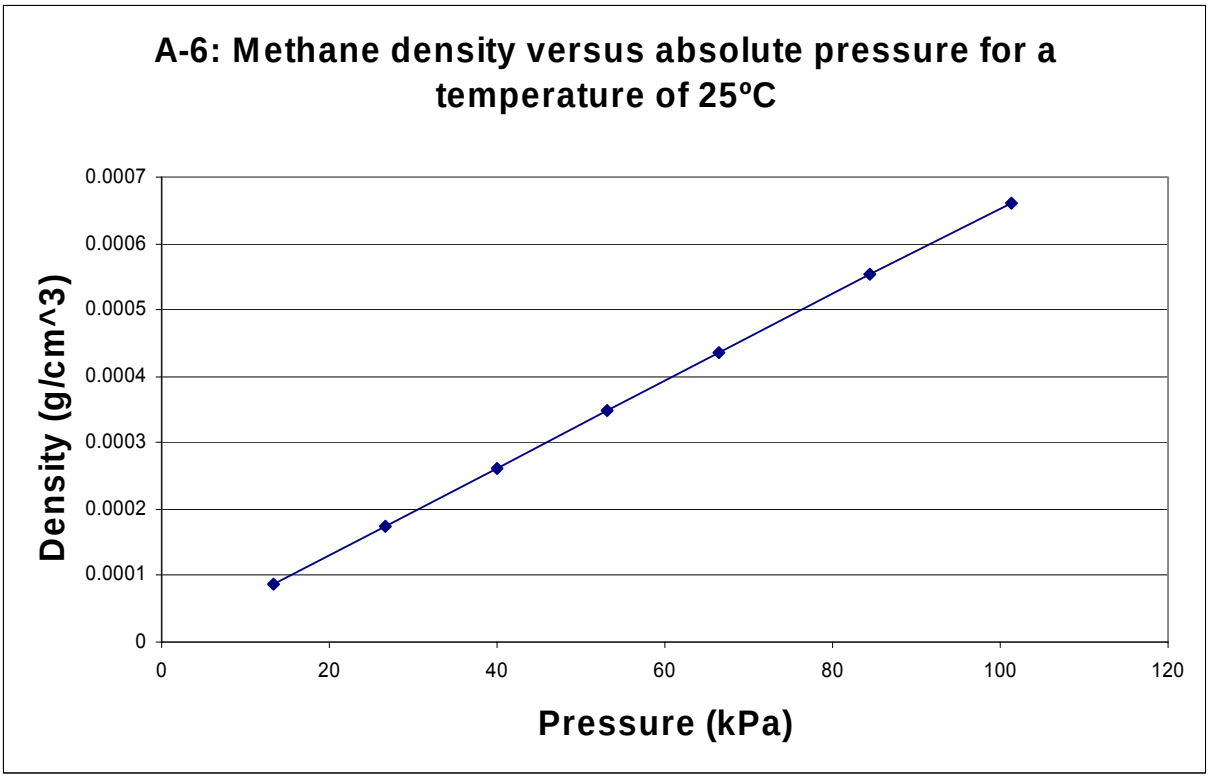

Pressure Torr	Pressure kPa	Density g/cm^3
100	13.3	0.000087
200	26.6	0.000174
300	39.9	0.000261
400	53.2	0.000348
500	66.5	0.000435
625	84.4	0.000553
760	101.3	0.000662

Data collected from Engineering Equation Solver v6.2 using the Database of Fluid and Thermodynamics (DFT) as the source for calculations.

A-7: Laser spot profile data.

Laser Spot Trials	Temperature (°C)	Scan Rate (in/min)	Experiment Trials
1	1350	0.2	7,8
2	1350	0.1	5,6
3	1200	0.2	3,4
4	1200	0.01	1,2

Zones	Low Temperature	High Temperature
	°C	°C
Blue	1190	1330
Green	1330	1420
Yellow	1420	1485
Red	1485	1600
White	1600	∞

	All measurements in microns									Diameter
Trial	Blue	Green	Yellow	Red	White	Red	Yellow	Green	Blue	
1.1.1	162.75	134.75	120.75	99.75	75.25	92.75	113.75	131.25	159.25	322
	176.75	141.75	127.75	103.25	78.75	99.75	124.25	138.25	159.25	336
	176.75	145.25	127.75	106.75	85.75	106.75	127.75	141.75	166.25	343
	171.5	143.5	126	105	77	105	126	136.5	161	332.5
	178.5	147	129.5	105	80.5	105	126	143.5	164.5	343
	162.75	134.75	117.25	92.75	64.75	89.25	110.25	124.25	148.75	311.5
	175	143.5	129.5	108.5	84	112	136.5	154	171.5	346.5
	166.25	134.75	117.25	96.25	64.75	89.25	113.75	127.75	148.75	315
Average	171.2813	140.6563	124.4688	102.1563	76.34375	99.96875	122.2813	137.1563	159.9063	331.1875

	Blue	Green	Yellow	Red	White	Red	Yellow	Green	Blue	
1.1.2	103.25	85.75	68.25	43.75	15.75	61.25	89.25	103.25	134.75	238
	108.5	87.5	70	49	0	49	70	84	108.5	217
	108.5	84	66.5	42	0	42	77	87.5	126	234.5
	108.5	80.5	63	35	0	35	63	80.5	101.5	210
	117.25	89.25	75.25	54.25	0	54.25	85.75	96.25	124.25	241.5
	110.25	85.75	64.75	43.75	0	43.75	82.25	96.25	117.25	227.5
Average	109.375	85.45833	67.95833	44.625	2.625	47.54167	77.875	91.29167	118.7083	228.0833

	Blue	Green	Yellow	Red	White	Red	Yellow	Green	Blue	
1.2.1	118.125	90.125	65.625	44.625	23.625	51.625	76.125	93.625	121.625	239.75
	103.25	75.25	57.75	40.25	22.75	54.25	78.75	99.75	131.25	234.5
	138.25	110.25	89.25	64.75	40.25	61.25	85.75	99.75	124.25	262.5
	127.75	96.25	78.75	57.75	43.75	71.75	96.25	113.75	145.25	273
	136.5	105	80.5	52.5	28	63	98	119	147	283.5
	129.5	101.5	80.5	63	49	73.5	94.5	115.5	150.5	280
Average	125.5625	96.39583	75.39583	53.8125	34.5625	62.5625	88.22917	106.8958	136.6458	262.2083

	Blue	Green	Yellow	Red	White	Red	Yellow	Green	Blue	
1.2.2	127.75	99.75	82.25	64.75	50.75	75.25	113.75	127.75	148.75	276.5
	140	112	91	70	52.5	73.5	94.5	112	133	273
	136.5	108.5	80.5	56	14	45.5	73.5	98	122.5	259
	134.75	103.25	82.25	61.25	40.25	61.25	89.25	113.75	141.75	276.5
	138.25	99.75	75.25	47.25	15.75	54.25	78.75	99.75	131.25	269.5
	148.75	117.25	85.75	61.25	40.25	57.75	99.75	120.75	148.75	297.5
Average	137.6667	106.75	82.83333	60.08333	35.58333	61.25	91.58333	112	137.6667	275.3333

	Blue	Green	Yellow	Red	White	Red	Yellow	Green	Blue	
2.1.1	133	108.5	94.5	77	63	80.5	115.5	143.5	182	315
	127.75	106.75	92.75	75.25	61.25	85.75	131.25	159.25	180.25	308
	112	94.5	84	70	59.5	84	133	164.5	189	301
	112	94.5	84	70	52.5	80.5	129.5	150.5	175	287
	122.5	101.5	87.5	73.5	59.5	80.5	119	140	168	290.5
	126	101.5	91	73.5	59.5	84	133	154	178.5	304.5
Average	122.2083	101.2083	88.95833	73.20833	59.20833	82.54167	126.875	151.9583	178.7917	301

	Blue	Green	Yellow	Red	White	Red	Yellow	Green	Blue	
2.1.2	110.25	89.25	75.25	61.25	43.75	57.75	78.75	99.75	131.25	241.5
	112	91	77	59.5	45.5	59.5	80.5	101.5	129.5	241.5
	108.5	87.5	77	63	49	66.5	98	115.5	140	248.5
	110.25	89.25	78.75	64.75	50.75	71.75	96.25	110.25	127.75	238
	112	91	80.5	66.5	49	70	94.5	108.5	136.5	248.5
Average	110.6	89.6	77.7	63	47.6	65.1	89.6	107.1	133	243.6

	Blue	Green	Yellow	Red	White	Red	Yellow	Green	Blue	
2.2.1	148.75	99.75	78.75	0	0	0	78.75	106.75	134.75	283.5
	161	119	84	52.5	0	52.5	73.5	87.5	108.5	269.5
	152.25	117.25	96.25	71.75	0	71.75	96.25	110.25	138.25	290.5
	127.75	82.25	61.25	43.75	26.25	57.75	78.75	92.75	120.75	248.5
	143.5	105	91	38.5	21	38.5	70	87.5	105	248.5
	143.5	115.5	91	38.5	21	38.5	59.5	73.5	98	241.5
Average	146.125	106.4583	83.70833	40.83333	11.375	43.16667	76.125	93.04167	117.5417	263.6667

	Blue	Green	Yellow	Red	White	Red	Yellow	Green	Blue	
2.2.2	124.25	92.75	33.25	0	0	0	33.25	57.75	82.25	206.5
	98	63	45.5	28	0	28	59.5	77	105	203
	140	108.5	28	0	0	0	28	63	98	238
	92.75	61.25	43.75	33.25	15.75	47.25	75.25	99.75	141.75	234.5
	112	77	49	31.5	0	31.5	56	84	122.5	234.5
	101.5	59.5	35	0	0	0	35	70	112	213.5
Average	111.4167	77	39.08333	15.45833	2.625	17.79167	47.83333	75.25	110.25	221.6667

	Blue	Green	Yellow	Red	White	Red	Yellow	Green	Blue	
3.1.1	77	59.5	42	21	0	21	35	45.5	66.5	143.5
	77	56	38.5	21	0	21	38.5	49	66.5	143.5
	70	52.5	42	24.5	0	24.5	42	52.5	73.5	143.5
	96.25	75.25	64.75	47.25	26.25	43.75	57.75	68.25	85.75	182
	119	94.5	84	70	56	70	80.5	91	108.5	227.5
	105	84	73.5	59.5	42	59.5	73.5	84	105	210
Average	90.70833	70.29167	57.45833	40.54167	20.70833	39.95833	54.54167	65.04167	84.29167	175

	Blue	Green	Yellow	Red	White	Red	Yellow	Green	Blue	
3.1.2	73.5	56	45.5	28	0	28	45.5	56	73.5	147
	84	66.5	52.5	35	0	35	52.5	63	80.5	164.5
	85.75	68.25	54.25	29.75	0	29.75	47.25	57.75	75.25	161
	80.5	63	52.5	28	0	28	45.5	56	77	157.5
Average	80.9375	63.4375	51.1875	30.1875	0	30.1875	47.6875	58.1875	76.5625	157.5

	Blue	Green	Yellow	Red	White	Red	Yellow	Green	Blue	
3.2.1	82.25	61.25	47.25	29.75	0	29.75	47.25	61.25	75.25	157.5
	77	59.5	45.5	24.5	0	24.5	49	63	80.5	157.5
	70	49	31.5	0	0	0	31.5	52.5	80.5	150.5
	94.5	73.5	59.5	42	17.5	38.5	49	59.5	80.5	175
Average	80.9375	60.8125	45.9375	24.0625	4.375	23.1875	44.1875	59.0625	79.1875	160.125

	Blue	Green	Yellow	Red	White	Red	Yellow	Green	Blue	
3.2.2	87.5	66.5	56	42	28	49	63	73.5	91	178.5
	91	73.5	59.5	38.5	0	38.5	56	66.5	84	175
	78.75	61.25	47.25	33.25	0	33.25	50.75	61.25	75.25	154
	68.25	50.75	40.25	29.75	15.75	36.75	54.25	64.75	82.25	150.5
Average	81.375	63	50.75	35.875	10.9375	39.375	56	66.5	83.125	164.5

	Blue	Green	Yellow	Red	White	Red	Yellow	Green	Blue	
4.1.1	89.25	71.75	57.75	43.75	19.25	40.25	57.75	68.25	89.25	178.5
	94.5	80.5	63	45.5	21	38.5	56	70	91	185.5
	87.5	66.5	49	31.5	0	31.5	49	63	84	171.5
	77	56	45.5	14	0	14	31.5	45.5	66.5	143.5
	98	80.5	70	59.5	42	59.5	73.5	84	105	203
Average	89.25	71.05	57.05	38.85	16.45	36.75	53.55	66.15	87.15	176.4

	Blue	Green	Yellow	Red	White	Red	Yellow	Green	Blue	
4.1.2	84	63	52.5	42	0	42	56	66.5	91	175
	85.75	64.75	54.25	36.75	0	36.75	61.25	71.75	92.75	178.5
	89.25	71.75	61.25	43.75	15.75	40.25	54.25	64.75	85.75	175
	71.75	54.25	43.75	26.25	1.75	29.75	47.25	57.75	78.75	150.5
	87.5	70	59.5	42	17.5	45.5	63	73.5	94.5	182
	73.5	52.5	38.5	21	0	21	42	52.5	77	150.5
	78.75	57.75	43.75	26.25	0	26.25	43.75	57.75	75.25	154
Average	81.5	62	50.5	34	5	34.5	52.5	63.5	85	166.5

	Blue	Green	Yellow	Red	White	Red	Yellow	Green	Blue	
4.2.1	84	66.5	56	42	24.5	42	56	66.5	84	168
	82.25	61.25	50.75	36.75	0	36.75	54.25	64.75	82.25	164.5
	73.5	52.5	38.5	0	0	0	38.5	52.5	77	150.5
	73.5	49	31.5	0	0	0	31.5	45.5	70	143.5
	68.25	47.25	29.75	0	0	0	29.75	47.25	71.75	140
Average	76.3	55.3	41.3	15.75	4.9	15.75	42	55.3	77	153.3

	Blue	Green	Yellow	Red	White	Red	Yellow	Green	Blue	
4.2.2	70	52.5	42	28	0	28	49	63	87.5	157.5
	82.25	61.25	47.25	22.75	0	22.75	47.25	64.75	89.25	171.5
	78.75	61.25	47.25	22.75	0	22.75	47.25	64.75	89.25	168
	59.5	42	28	0	0	0	28	59.5	87.5	147
	84	63	52.5	38.5	14	38.5	59.5	77	101.5	185.5
	92.75	75.25	64.75	47.25	29.75	54.25	71.75	85.75	106.75	199.5
	75.25	57.75	47.25	33.25	19.25	40.25	61.25	71.75	89.25	164.5
Average	77.5	59	47	27.5	9	29.5	52	69.5	93	170.5

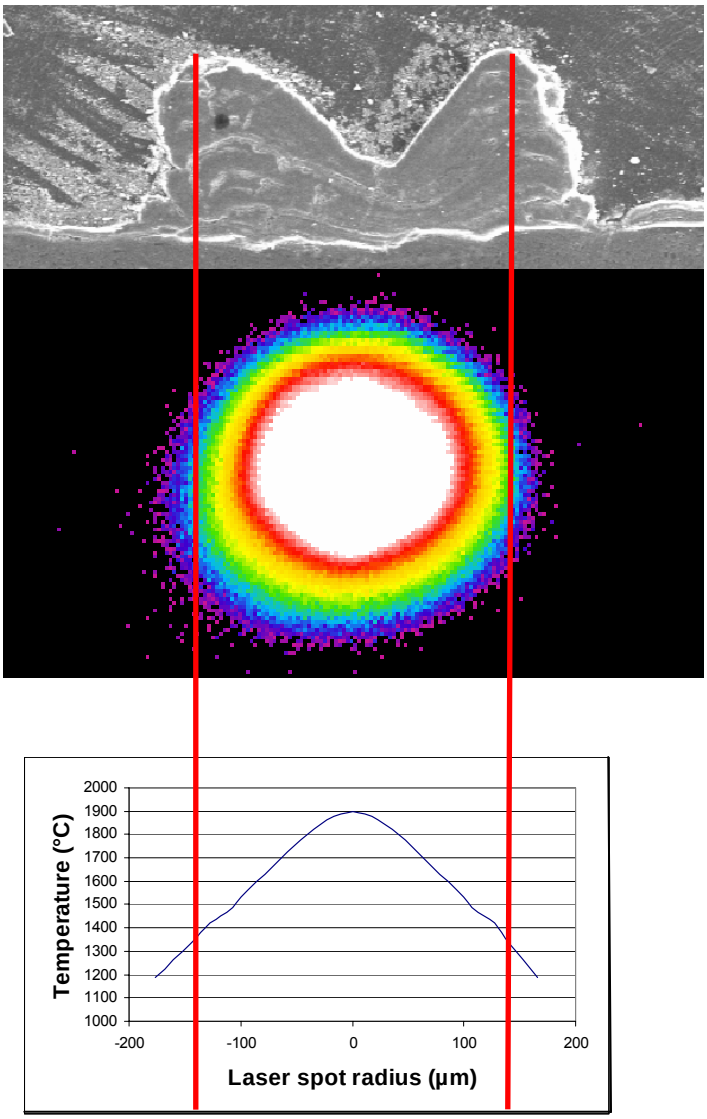
Temperature (°C)
2000
1900
1800
1700
1600
1500
1400
1300
1200
1100
1000
-200
-100
0
100
200
Laser spot radius (µm)

Laminate Walls

	Factors				All measurments in microns								
Exp	Temperature (°C)	Scan Rate (in/min)	RST	Pressure (torr)	Height	Height	Height	Height	Width	Width	Width	Width	Width
1	1200	0.1	FGM	300	30				278	156	225.8		
2	1200	0.1	Distinct	790	Trace	Trace			Trace	Trace			
3	1200	0.02	FGM	790	50.8	26.86			345	312			
4	1200	0.2	Distinct	300	5	4.5	25.3		248.9	220	210.2	213	268.7
5	1350	0.1	FGM	790	138.9	122.9			Trace	416.7	451.8	221.4	
6	1350	0.1	Distinct	300	156	129.3	100	149.1	600	468.7	575.1	609.4	
7	1350	0.2	FGM	300	87.7	49	Trace		404	Trace	404	398.4	384.4
8	1350	0.2	Distinct	790	175.1				470	380	588	414	
Midpoint	1325	0.15	FGM	650	232				327	387	382.3	381.7	

Exp	Peak-Peak	Peak-Peak	Peak-Peak	Peak-Peak	Peak-Ctr	Peak-Ctr	Peak-Ctr	Peak-Ctr	Peak-Ctr	Peak-Ctr	Peak-Ctr	Peak-Ctr
1	111.7				40.63	72.65						
2	Flat				Flat	Flat	Flat	Flat				
3	134.6				62.95	71.65						
4	Flat	Flat	Flat		Flat	Flat	Flat	Flat	Flat	Flat		
5	231.8	132.8			100.3	132.8	64.36	68.48				
6	342.2	348.4	334.4	304.7	98.43	242.2	220.3	128.1	140	193.3	146	156.8
7	203.1	244.9			86.66	131.5	114.8	130.1				
8	266.6				101.7	175.1						
Midpoint	265	238.1			108.7	155.3	96.6	141.5				

A-8: Deposit measurements.

Codeposition Walls

All measurements in microns

Exp	Temperature (ºC)	Scan Rate (in/min)	Pressure (torr)	Height	Height	Height	Width	Width	Width	Width	Width
1	1200	0.2	300	6.4	Trace		351.4	197.5			
2	1200	0.1	790	Trace	Trace		Trace	Trace			
4	1350	0.1	300	31.11	25.5		390	350	369.1	313.8	
7	1350	0.2	790				400	395			
Midpoint	1325	0.15	650	109.6	157.8	148	366.7	352	394.7	351.6	371.2

Exp	Peak-Peak	Peak-Peak	Peak-Peak	Peak-Ctr	Peak-Ctr	Peak-Ctr	Peak-Ctr	Peak-Ctr	Peak-Ctr
1	flat			flat					
2									
4	235	216.1		235	216.1				
7									
Midpoint	234.4	198	226.9	95.62	140.6	71.5	128.9	89.1	140.6

Codeposition Fibers

All measurements in microns

Exp	Temperature (ºC)	Pressure (torr)	Height	Height	Diameter	Diameter
1	1200	300	538.4	Trace	171.3	Trace
2	1200	790	465	Trace	170	Trace
4	1350	300	Trace	Trace	232	Trace
7	1350	790	563.3	542.5	371.1	337
Midpoint	1325	650	889	916.5	402.2	394.5

A-8: Deposit measurements.

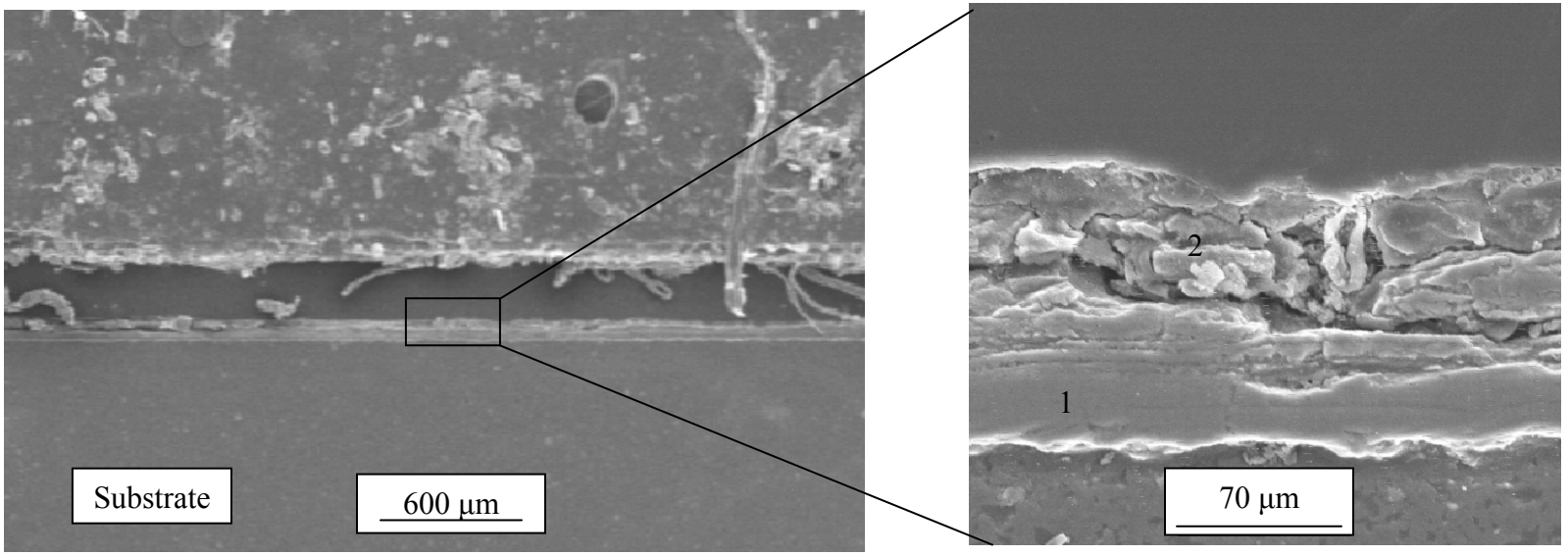

Quantitative Analysis 3-2-1 Section 1

Filter Fit Method
Chi-sqd = 22.05 Livetime = 60.0 Sec.
Standardless Analysis

Element	Relative k-ratio	Error (1-Sigma)	Net Counts	Error (1-Sigma)
C -K	0.09527	+/- 0.00347	907	+/- 33
O -K	0.01636	+/- 0.00221	229	+/- 31
Si-K	0.88837	+/- 0.00535	41379	+/- 249

Element	k-ratio (calc.)	ZAF	Atom %	Element Wt %	Wt % Err. (1-Sigma)	No. of Cations
C -K	0.0464	9.422	62.50	43.67	+/- 1.59	213.211
O -K	0.0080	8.229	7.04	6.55	+/- 0.89	---
Si-K	0.4322	1.152	30.46	49.78	+/- 0.30	103.921
Total			100.00	100.00		317.131

The number of cation results are based upon 24 Oxygen atoms.

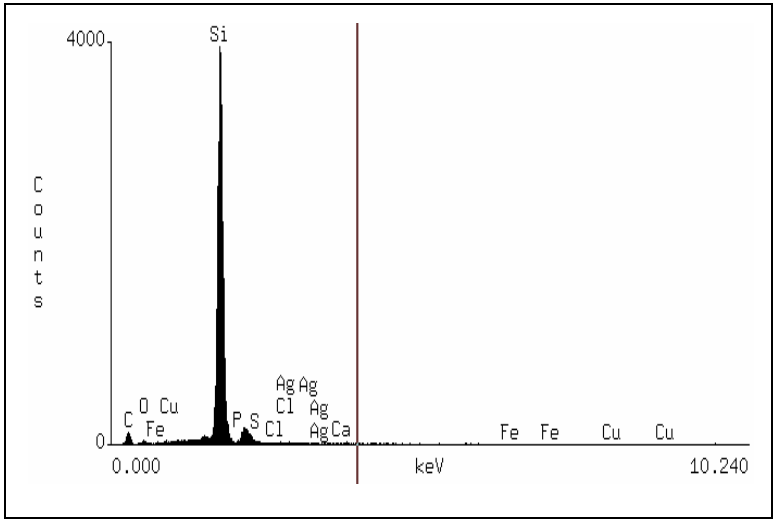

A-9. SEM micrographs of the longitudinal cross section of 3-2-1.

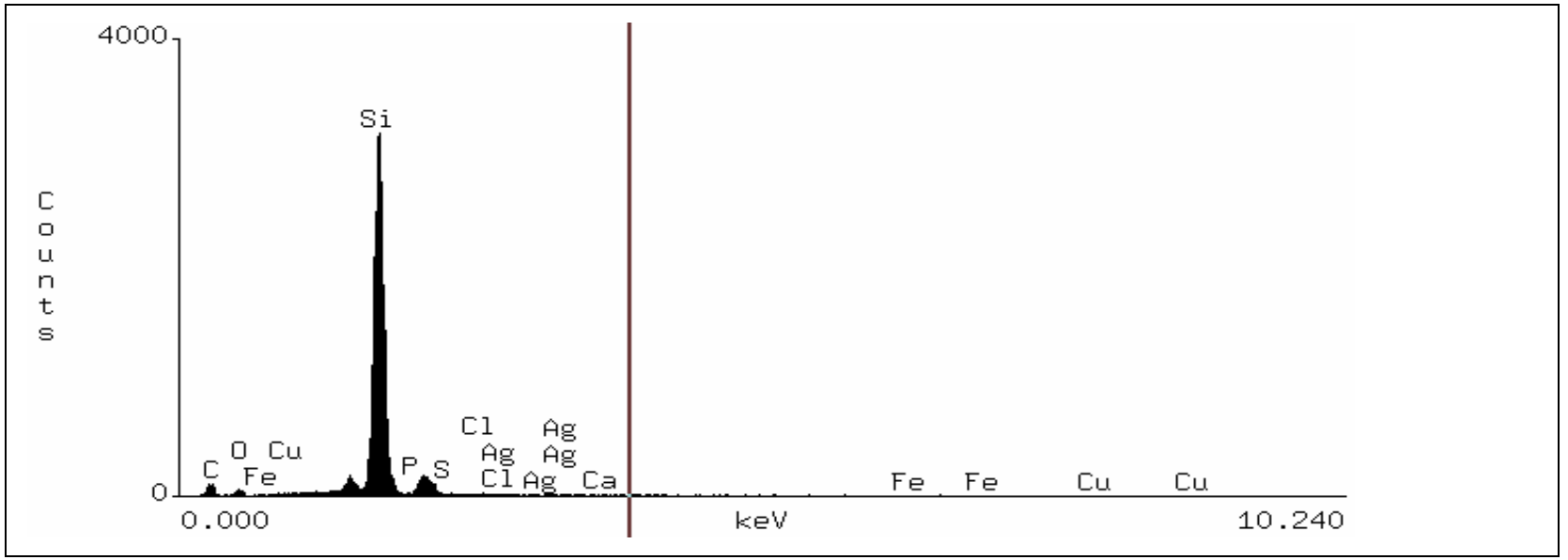

Quantitative Analysis 3-2-1 Section 1

Filter Fit Method
Chi-sqd = 36.77 Livetime = 60.0 Sec.
Standardless Analysis

Element	Relative k-ratio	Error (1-Sigma)	Net Counts	Error (1-Sigma)
C -K	0.10393	+/- 0.00401	829	+/- 32
O -K	0.02904	+/- 0.00272	342	+/- 32
Si-K	0.86703	+/- 0.00573	33875	+/- 224

Element	k-ratio (calc.)	ZAF	Atom %	Element Wt %	Wt % Err. (1-Sigma)	No. of Cations
C -K	0.0476	8.999	60.57	42.81	+/- 1.65	129.614
O -K	0.0133	7.945	11.21	10.56	+/- 0.99	---
Si-K	0.3968	1.175	28.22	46.64	+/- 0.31	60.388
Total			100.00	100.00		190.002

The number of cation results are based upon 24 Oxygen atoms

EDS Analysis of wall 3-2-1 section 2.

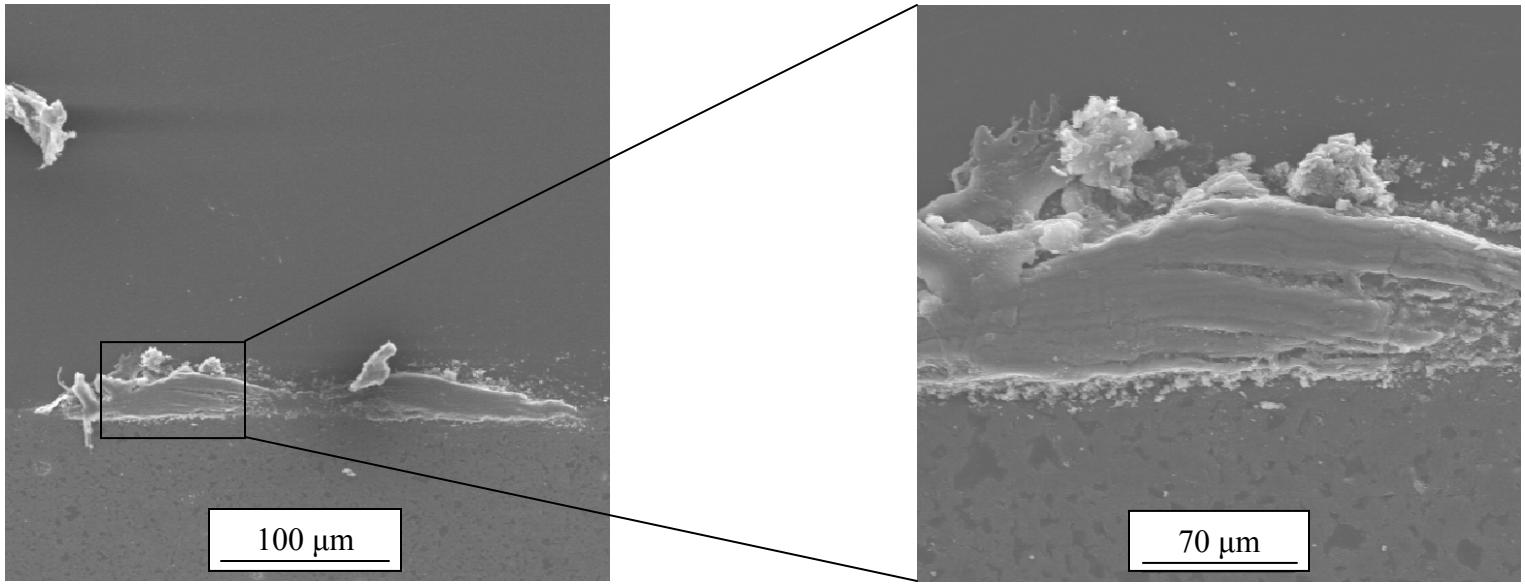

Quantitative Analysis

Filter Fit Method
Chi-sqd = 17.91 Livetime = 60.0 Sec.
Standardless Analysis

Element	Relative k-ratio	Error (1-Sigma)	Net Counts	Error (1-Sigma)
O -K	0.01243	+/- 0.00158	261	+/- 33
Si-K	0.93156	+/- 0.00514	52005	+/- 287
C -K	0.05601	+/- 0.00199	959	+/- 34

Element	k-ratio (calc.)	ZAF	Atom %	Element Wt %	Wt % Err. (1-Sigma)	No. of Cations
O -K	0.0082	4.066	4.07	3.32	+/- 0.42	---
Si-K	0.6111	1.087	46.42	66.39	+/- 0.37	273.758
C -K	0.0367	8.244	49.51	30.29	+/- 1.07	292.034
Total			100.00	100.00		565.793

The number of cation results are based upon 24 Oxygen atoms

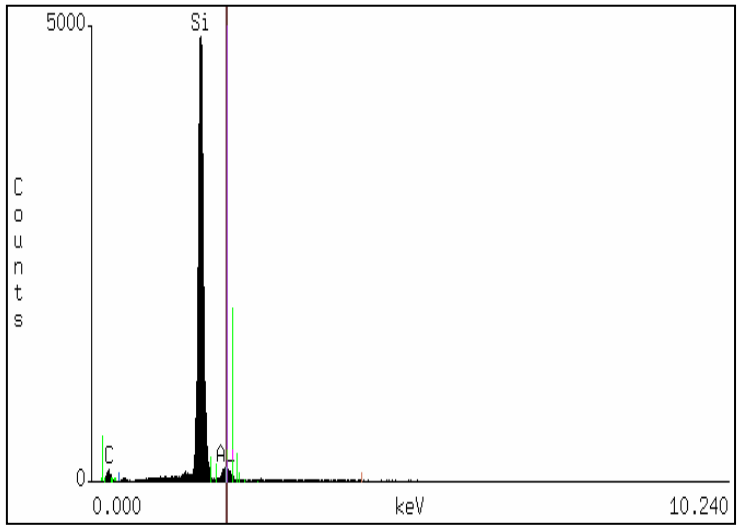

Appensdix A-10. SEM micrographs and EDS analysis for wall 3-2-2. The EDS analysis covers the left peak region.

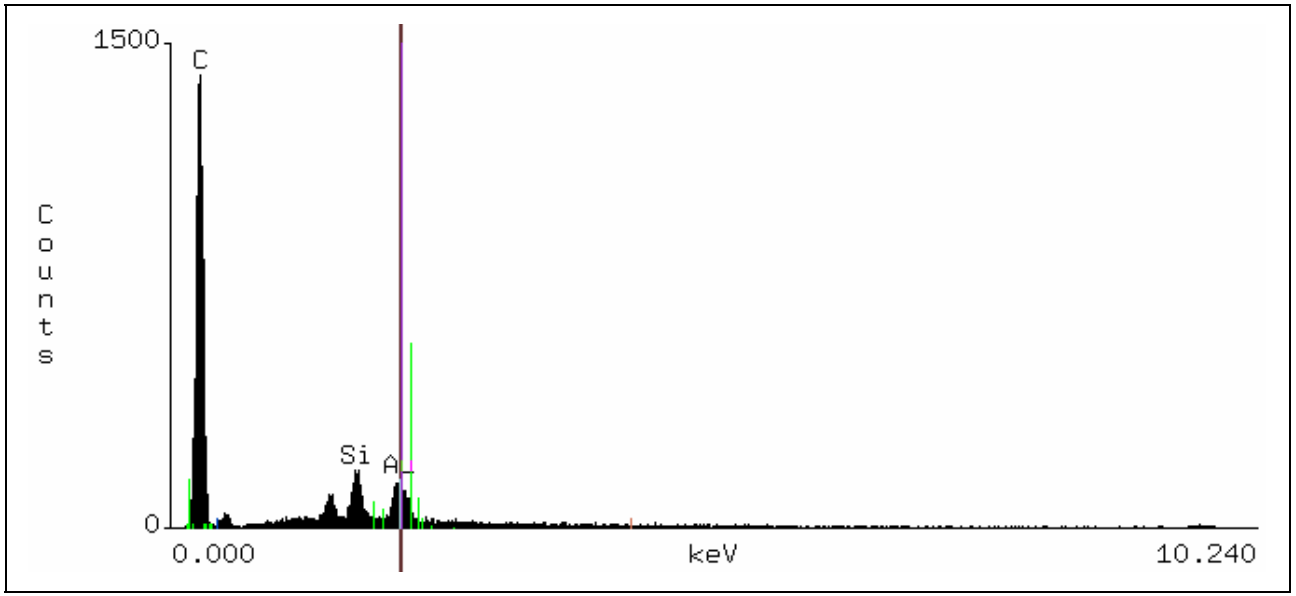

Quantitative Analysis 3-2-2

Filter Fit Method
Chi-sqd = 26.18 Livetime = 60.0 Sec.
Standardless Analysis

Element	Relative k-ratio	Error (1-Sigma)	Net Counts	Error (1-Sigma)
O -K	0.01925	+/- 0.00202	276	+/- 29
Si-K	0.03911	+/- 0.00178	1498	+/- 68
C -K	0.94164	+/- 0.00827	11042	+/- 97

Element	k-ratio (calc.)	ZAF	Atom %	Element Wt %	Wt % Err. (1-Sigma)	No. of Cations
O -K	0.0138	5.654	6.09	7.80	+/- 0.82	---
Si-K	0.0280	1.222	1.52	3.43	+/- 0.16	6.006
C -K	0.6748	1.315	92.38	88.77	+/- 0.78	363.850
Total			100.00	100.00		369.856

The number of cation results are based upon 24 Oxygen atoms

EDS Analysis for 3-2-2 showing carbon deposition under the volcano effect.

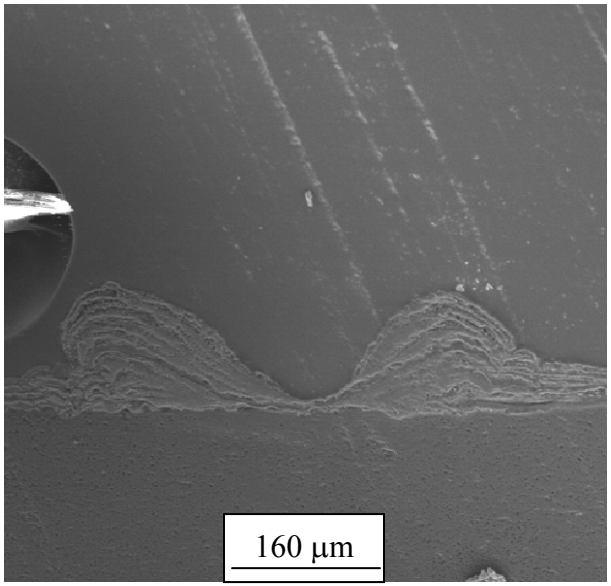

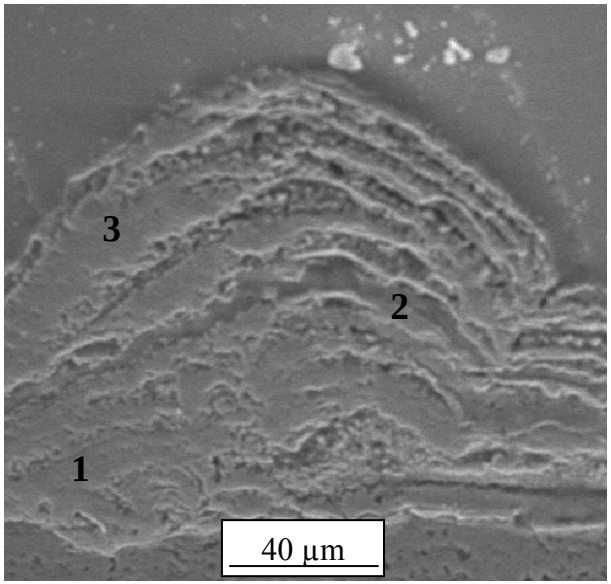

Quantitative Analysis 6-2-1 eds1

Filter Fit Method
Chi-sqd = 4.48 Livetime = 60.0 Sec.
Standardless Analysis

Element	Relative k-ratio	Error (1-Sigma)	Net Counts	Error (1-Sigma)
C -K	0.04576	+/- 0.00280	328	+/- 20
O -K	0.01534	+/- 0.00229	134	+/- 20
Si-K	0.93890	+/- 0.00716	21899	+/- 167

Element	k-ratio (calc.)	ZAF	Atom %	Element Wt %	Wt % Err. (1-Sigma)	No. of Cations
C -K	0.0312	8.549	44.91	26.65	+/- 1.63	206.598
O -K	0.0104	3.947	5.22	4.12	+/- 0.62	---
Si-K	0.6397	1.082	49.88	69.22	+/- 0.53	229.448
Total			100.00	100.00		436.046

The number of cation results are based upon 24 Oxygen atoms

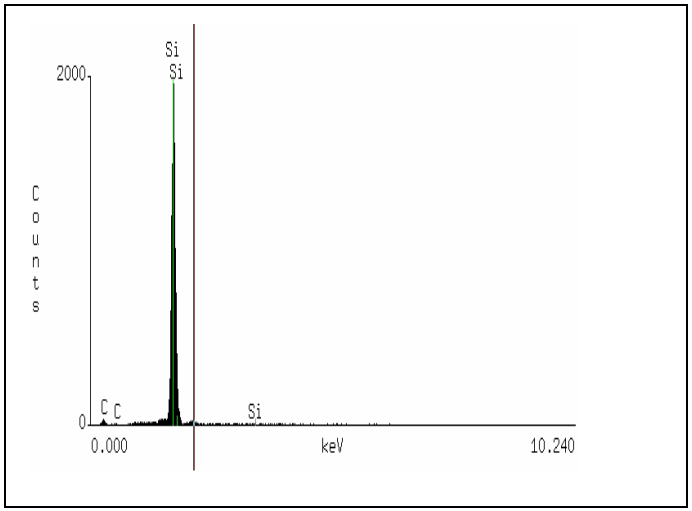

Appendix A-11. SEM micrographs and EDS reports for sections of wall 6-2-1.

Quantitative Analysis 6-2-1 EDS2

```
Refit _O -K' _O -K"
Filter Fit Method
Chi-sqd = 3.23     Livetime = 60.0 Sec.
Standardless Analysis
Element   Relative     Error        Net      Error
          k-ratio    (1-Sigma)     Counts  (1-Sigma)
  C -K    0.71380 +/- 0.01020       3429 +/-    49
  O -K    0.00307 +/- 0.00153         18 +/-     9
  Si-K    0.28313 +/- 0.00485       4438 +/-    76

Element  k-ratio    ZAF   Atom %  Element  Wt % Err.  No. of
         (calc.)                   Wt %   (1-Sigma)  Cations
  C -K    0.3356   2.485   91.88   83.39    +/- 1.19
  O -K    0.0014   5.702    0.68    0.82    +/- 0.41
  Si-K    0.1331   1.186    7.44   15.78    +/- 0.27
  Total                   100.00  100.00                0.000

   The number of cation results are based upon 24 Oxygen atoms
```

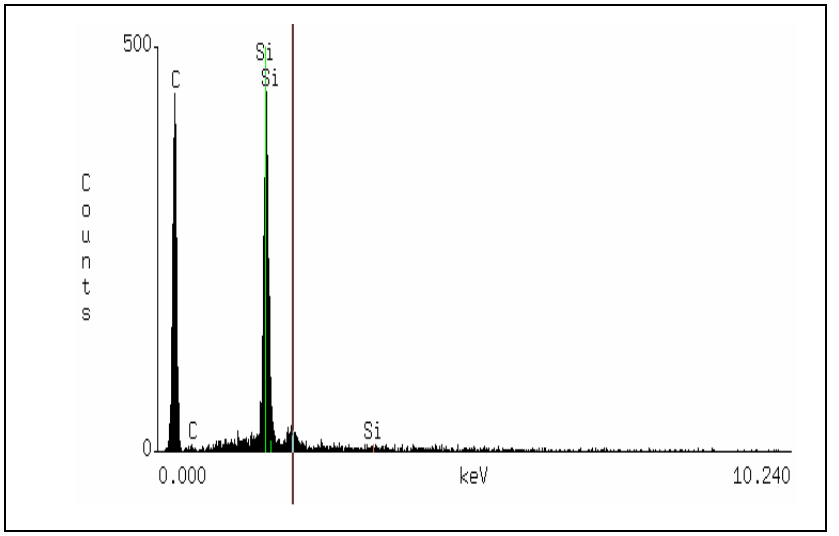

Quantitative Analysis 6-2-1 EDS3

```
Filter Fit Method
Chi-sqd = 4.48     Livetime = 60.0 Sec.
Standardless Analysis
Element   Relative     Error        Net      Error
          k-ratio    (1-Sigma)     Counts  (1-Sigma)
  C -K    0.04576 +/- 0.00280         328 +/-    20
  O -K    0.01534 +/- 0.00229         134 +/-    20
  Si-K    0.93890 +/- 0.00716       21899 +/-   167

Element  k-ratio    ZAF   Atom %  Element  Wt % Err.  No. of
         (calc.)                   Wt %   (1-Sigma)  Cations
  C -K    0.0312   8.549   44.91   26.65    +/- 1.63  206.598
  O -K    0.0104   3.947    5.22    4.12    +/- 0.62     ---
  Si-K    0.6397   1.082   49.88   69.22    +/- 0.53  229.448
  Total                   100.00  100.00              436.046

The number of cation results are based upon 24 Oxygen atoms
```

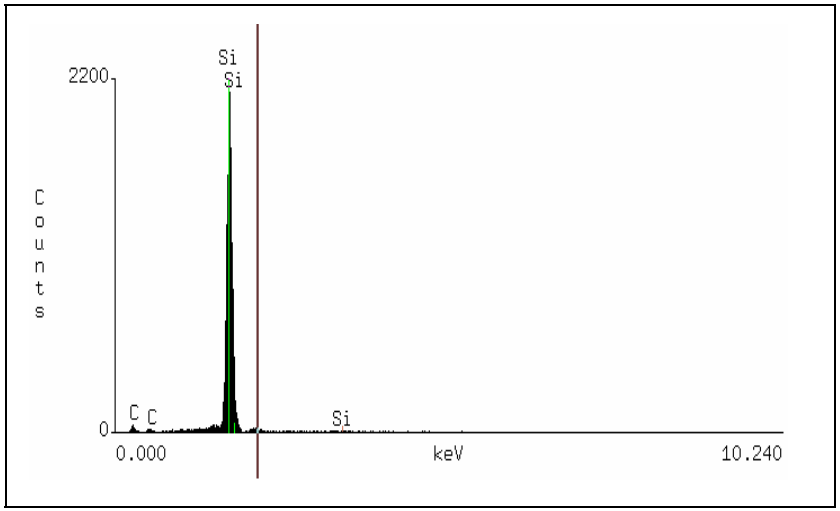

EDS reports for noted sections 6-2-1.

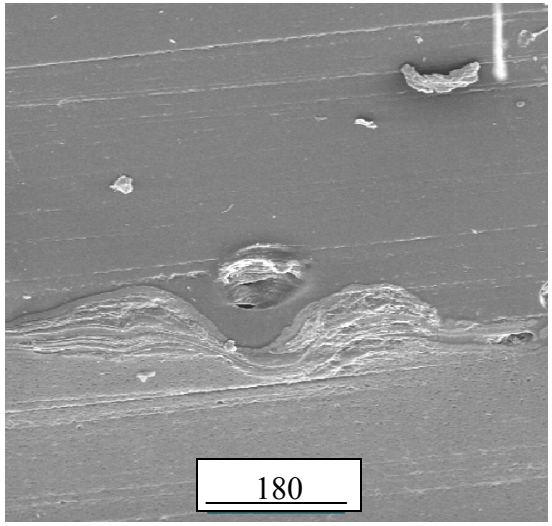

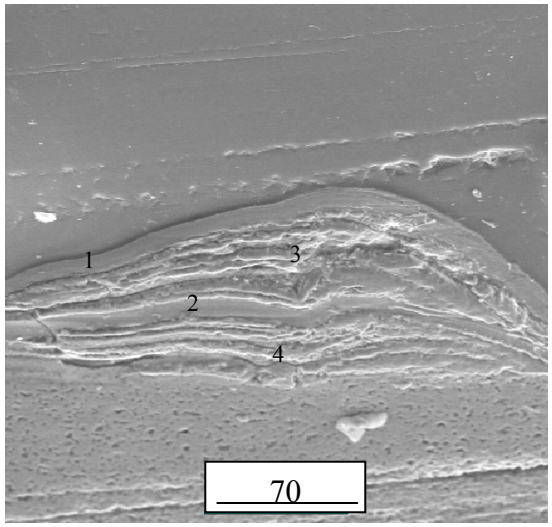

Quantitative Analysis 6-2-2 eds1

Filter Fit Method
Chi-sqd = 2.22 Livetime = 60.0 Sec.
Standardless Analysis

Element	Relative k-ratio	Error (1-Sigma)	Net Counts	Error (1-Sigma)
C -K	0.28017	+/- 0.00699	1284	+/- 32
O -K	0.02340	+/- 0.00339	131	+/- 19
Si-K	0.69643	+/- 0.00749	10409	+/- 112

PROZA Correction Acc.Volt.= 15 kV Take-off Angle=39.62 deg
Tilt = 30 deg
Number of Iterations = 12

Element	k-ratio (calc.)	ZAF	Atom %	Element Wt %	Wt % Err. (1-Sigma)	No. of Cations
C -K	0.1244	4.780	75.81	59.44	+/- 1.48	378.467
O -K	0.0104	4.835	4.81	5.02	+/- 0.73	---
Si-K	0.3091	1.150	19.38	35.53	+/- 0.38	96.753
Total			100.00	100.00		475.219

The number of cation results are based upon 24 Oxygen atoms

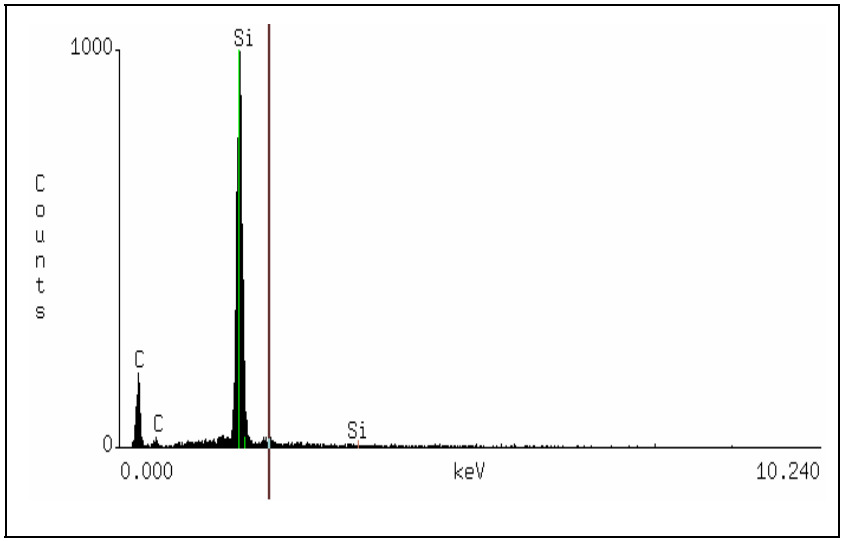

Appendix A-12. SEM and EDS micrographs for sections of Trial 6-2-2.

Quantitative Analysis 6-2-2 eds2

```
Refit _O -K' _O -K"
Filter Fit Method
Chi-sqd = 4.36     Livetime = 60.0 Sec.
Standardless Analysis
Element   Relative     Error        Net      Error
          k-ratio    (1-Sigma)     Counts  (1-Sigma)
  C -K    0.84740 +/- 0.00973       5487 +/-    63
  O -K    0.00594 +/- 0.00139         47 +/-    11
  Si-K    0.14666 +/- 0.00312       3099 +/-    66
PROZA Correction  Acc.Volt.= 15 kV  Take-off Angle=39.62 deg
Tilt = 30 deg
Number of Iterations = 13

Element  k-ratio    ZAF   Atom %  Element  Wt % Err.  No. of
         (calc.)                    Wt %   (1-Sigma)  Cations
  C -K    0.4721   1.869   93.99   88.26    +/- 1.01 1462.480
  O -K    0.0033   5.832    1.54    1.93    +/- 0.45     ---
  Si-K    0.0817   1.200    4.47    9.81    +/- 0.21   69.492
  Total                   100.00  100.00             1531.972
The number of cation results are based upon 24 Oxygen atoms
```

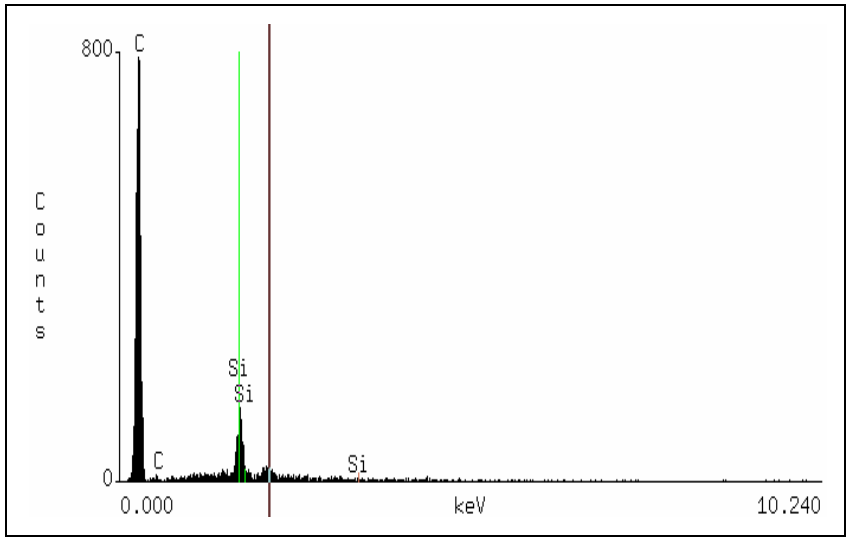

Quantitative Analysis 6-2-3 eds3

```
Filter Fit Method
Chi-sqd = 24.35     Livetime = 60.0 Sec.
Standardless Analysis
Element   Relative     Error        Net      Error
          k-ratio    (1-Sigma)     Counts  (1-Sigma)
  C -K    0.14848 +/- 0.00492        877 +/-    29
  O -K    0.06183 +/- 0.00388        446 +/-    28
  Si-K    0.78970 +/- 0.00743      15207 +/-   143
PROZA Correction  Acc.Volt.= 15 kV  Take-off Angle=39.62 deg
Tilt = 30 deg
Number of Iterations = 7

Element  k-ratio    ZAF   Atom %  Element  Wt % Err.  No. of
         (calc.)                    Wt %   (1-Sigma)  Cations
  C -K    0.0731   5.878   60.18   43.00    +/- 1.42  108.934
  O -K    0.0305   4.143   13.26   12.62    +/- 0.79     ---
  Si-K    0.3890   1.141   26.57   44.39    +/- 0.42   48.094
  Total                   100.00  100.00              157.028
The number of cation results are based upon 24 Oxygen atom
```

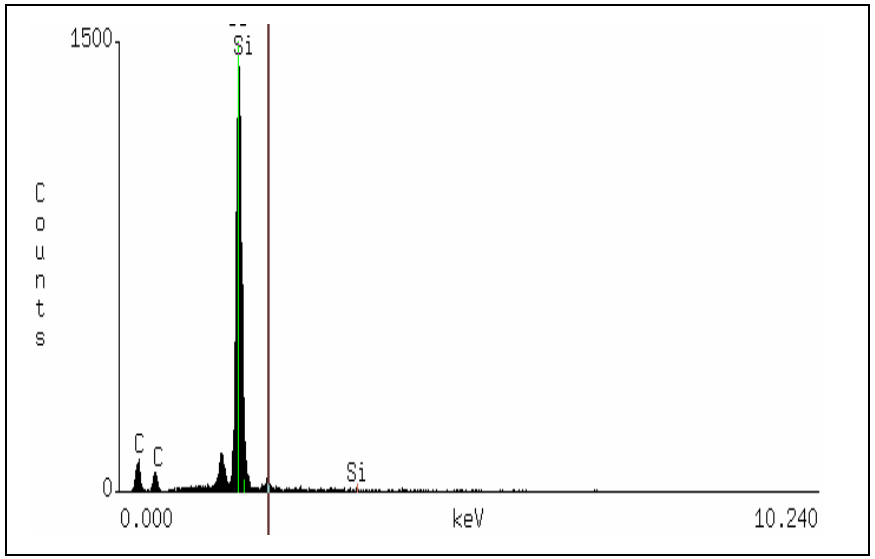

EDS Reports for sections of 6-2-2.

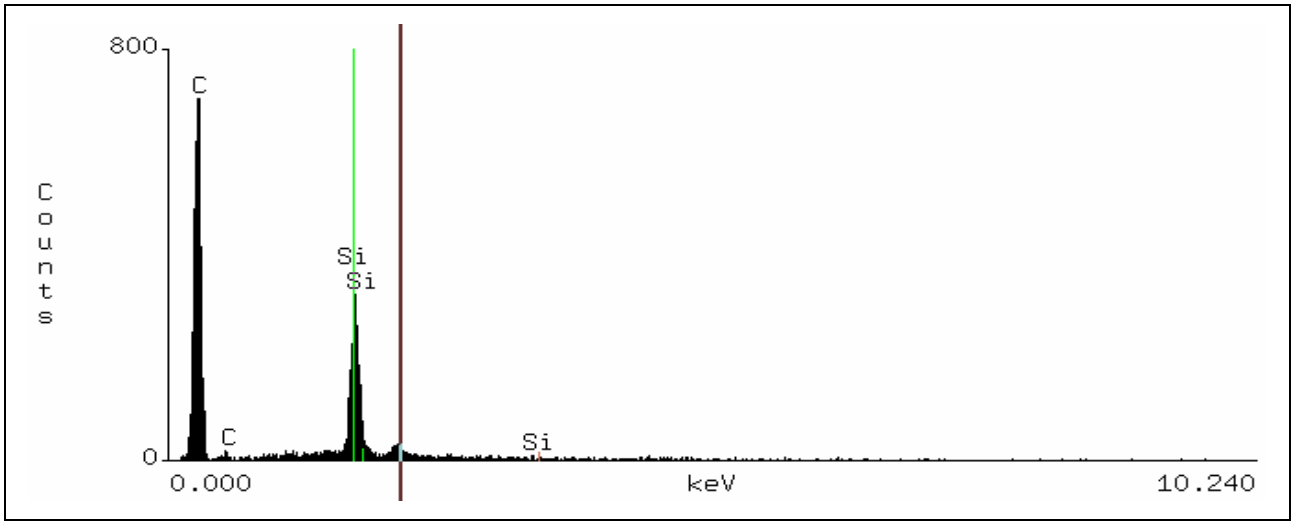

Quantitative Analysis

```
Refit _O -K' _O -K"
       Fit Method
Chi-sqd = 5.47     Livetime = 60.0 Sec.
   ndardless Analysis
Element   Relative     Error        Net      Error
          k-ratio    (1-Sigma)     Counts  (1-Sigma)
                                    5453 +/-    62
  O -K    0.00584 +/- 0.00142         52 +/-    10
                                    3115 +/-    67
                                    Take-off Angle=39.62 deg   Tilt = 30 deg


Element  k-ratio    ZAF   Atom %  Element  Wt % Err.  No. of
                                             igma)  Cations
                                              1.03 1424.540
                                              0.47     ---
                                              0.19   73.472
                                                   1498.012

                                                Oxygen atoms
```

EDS report for section 4 of 6-2-2

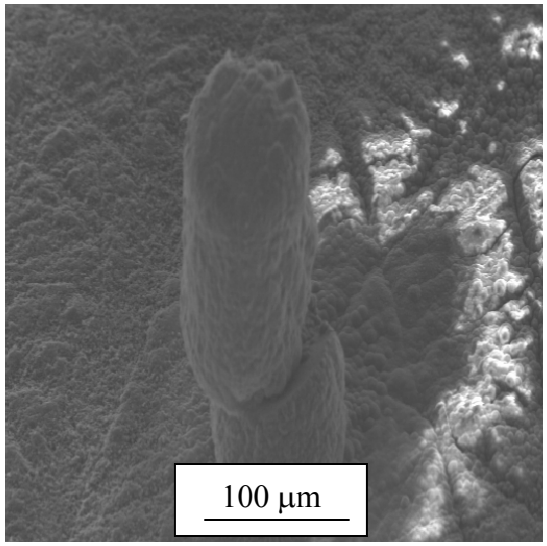

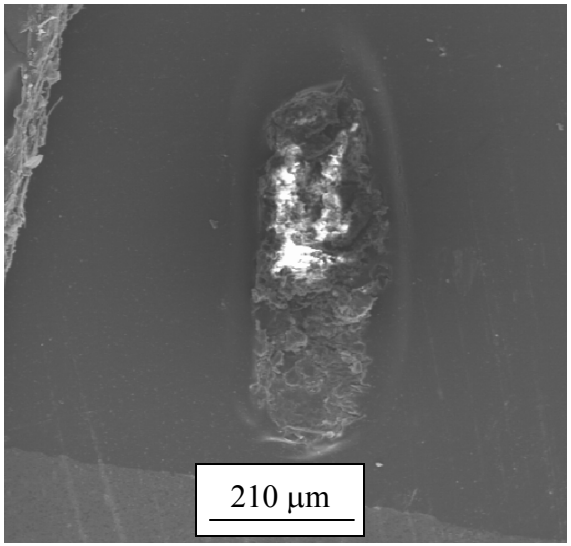

Quantitative Analysis 1-3-F1 eds1

Refit _Cl-K' _Cl-K"
Refit _O -K' _Si-K'
Filter Fit Method
Chi-sqd = 29.39 Livetime = 60.0 Sec.
Standardless Analysis

Element	Relative k-ratio	Error (1-Sigma)	Net Counts	Error (1-Sigma)
C -K	0.86295	+/- 0.01131	4654	+/- 61
O -K	0.10267	+/- 0.00516	677	+/- 34
Si-K	0.02386	+/- 0.00301	421	+/- 53
Cl-K	0.01052	+/- 0.00235	131	+/- 29

Element	k-ratio (calc.)	ZAF	Atom %	Element Wt %	Wt % Err. (1-Sigma)	No. of Cations
C -K	0.4955	1.432	77.20	70.95	+/- 0.93	85.290
O -K	0.0590	4.511	21.72	26.59	+/- 1.34	---
Si-K	0.0137	1.251	0.80	1.71	+/- 0.22	0.881
Cl-K	0.0060	1.236	0.28	0.75	+/- 0.17	0.304
Total			100.00	100.00		86.475

The number of cation results are based upon 24 Oxygen atoms.

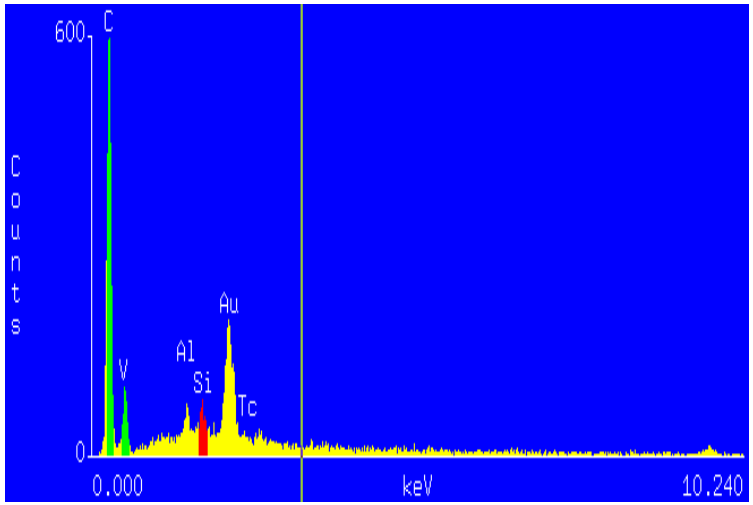

Appendix A-13. SEM micrographs (external and longitudinal) and EDS reports for Trial 1-3-F1.

Quantitative Analysis 1-3-F1 eds2

Refit _Si-K' _Si-K" _Cl-K' _Cl-K"
Refit _O -K'
Filter Fit Method
Chi-sqd = 50.25 Livetime = 60.0 Sec.
Standardless Analysis

Element	Relative k-ratio	Error (1-Sigma)	Net Counts	Error (1-Sigma)
C -K	0.87526	+/- 0.01032	5940	+/- 70
O -K	0.09848	+/- 0.00434	818	+/- 36
Si-K	0.01874	+/- 0.00154	415	+/- 34
Cl-K	0.00753	+/- 0.00187	117	+/- 29

Element	k-ratio (calc.)	ZAF	Atom %	Element Wt %	Wt % Err. (1-Sigma)	No. of Cations
C -K	0.5201	1.376	77.59	71.56	+/- 0.84	86.367
O -K	0.0585	4.527	21.56	26.49	+/- 1.17	---
Si-K	0.0111	1.252	0.65	1.39	+/- 0.11	0.720
Cl-K	0.0045	1.235	0.20	0.55	+/- 0.14	0.226
Total			100.00	100.00		87.313

The number of cation results are based upon 24 Oxygen atoms

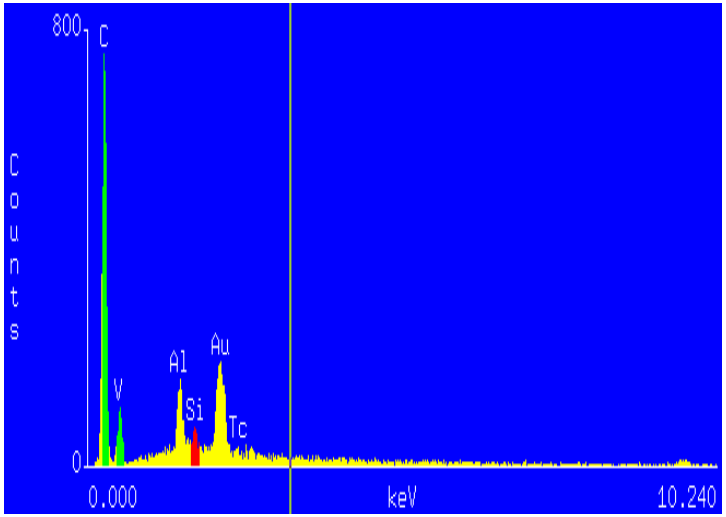

Quantitative Analysis 1-3-f1-eds3

Refit _Si-K' _Si-K" _Cl-K' _Cl-K"
Filter Fit Method
Chi-sqd = 36.68 Livetime = 60.0 Sec.
Standardless Analysis

Element	Relative k-ratio	Error (1-Sigma)	Net Counts	Error (1-Sigma)
C -K	0.89233	+/- 0.00793	12599	+/- 112
O -K	0.09791	+/- 0.00324	1690	+/- 56
Si-K	0.00454	+/- 0.00069	210	+/- 32
Cl-K	0.00523	+/- 0.00090	169	+/- 29

Element	k-ratio (calc.)	ZAF	Atom %	Element Wt %	Wt % Err. (1-Sigma)	No. of Cations
C -K	0.5616	1.275	77.29	71.59	+/- 0.64	82.806
O -K	0.0616	4.486	22.40	27.64	+/- 0.92	---
Si-K	0.0029	1.257	0.17	0.36	+/- 0.05	0.177
Cl-K	0.0033	1.232	0.15	0.41	+/- 0.07	0.159
Total			100.00	100.00		83.142

The number of cation results are based upon 24 Oxygen atoms

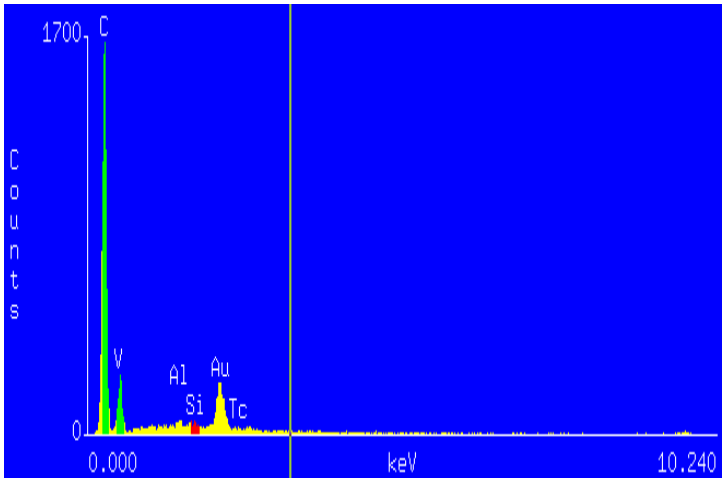

EDS Reports for sections 2 and 3 for Trial 1-3-F1.

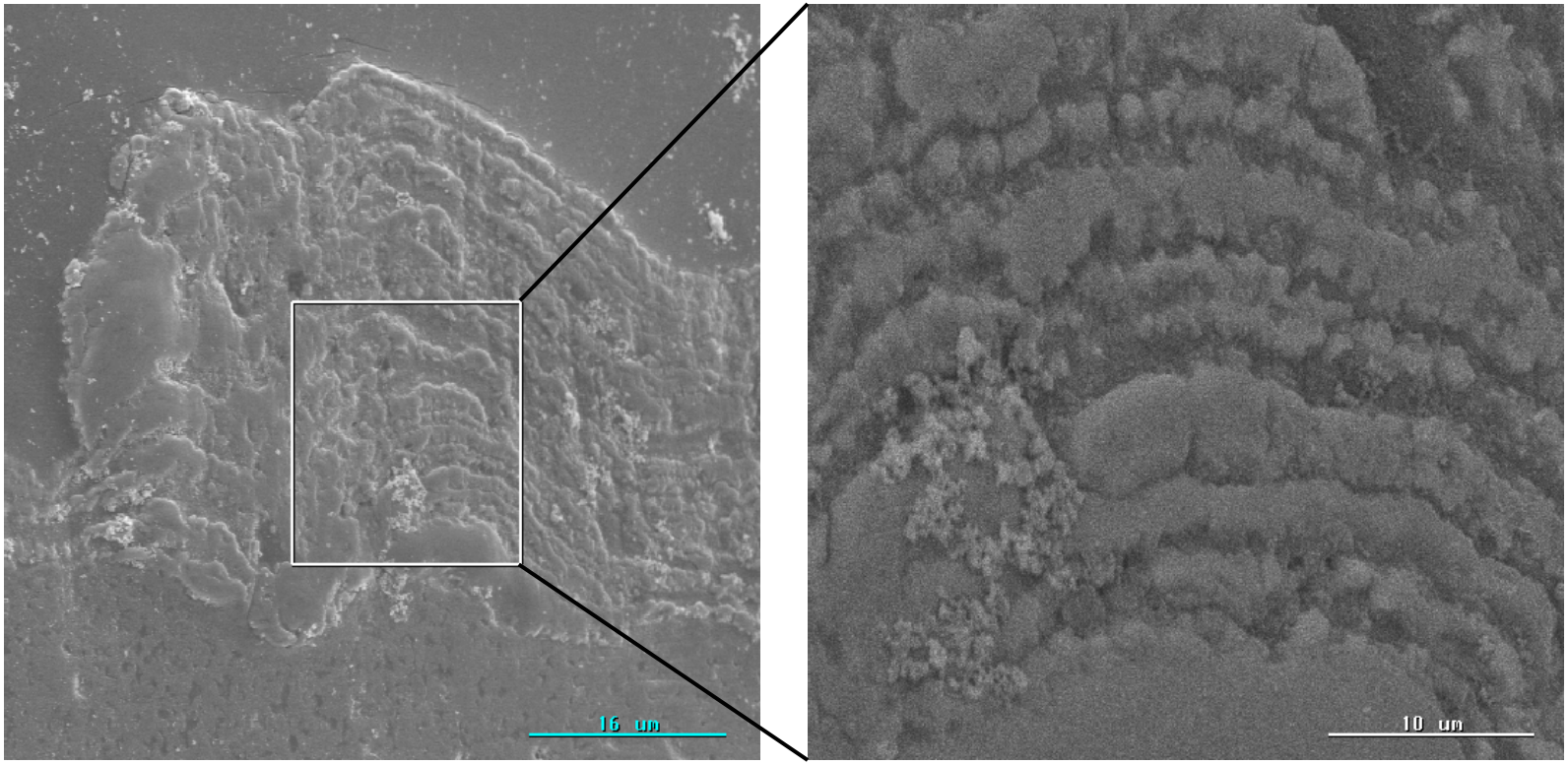

Appendix A-14. SEM micrograph (left) and back scatter image (right). The dark regions in the backscatter image denote carbon deposition and the lighter region denotes silicon carbide deposition. Despite a constant composition of reagents, alternate layering occurred. Some of there alternations occurred during only one pass of the laser.

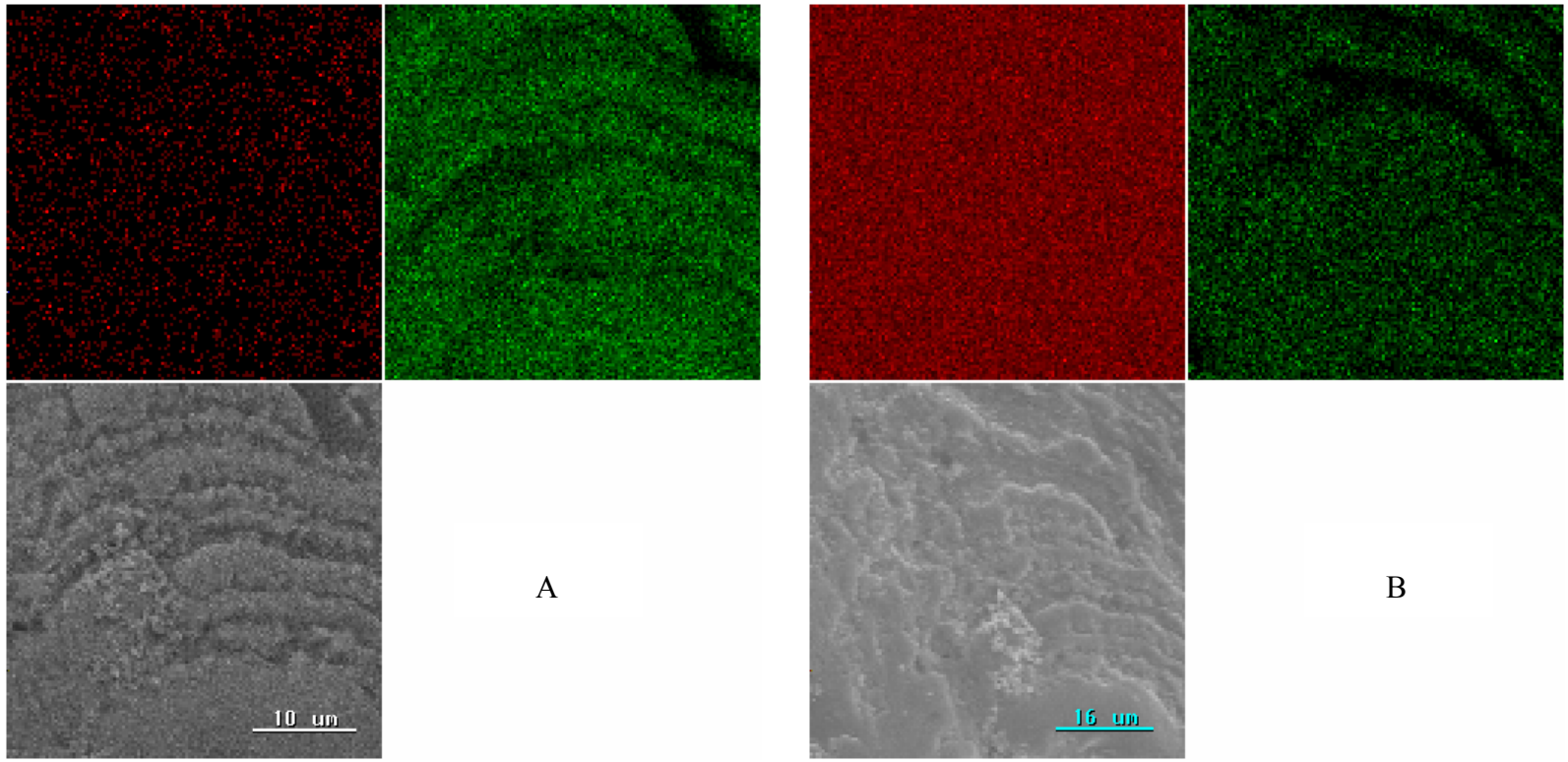

(A) Backscatter image with carbon map (red) and silicon map (green) and (B) SEM micrograph or the same region slightly offset with associated carbon and silicon maps. The carbon element is uniformly distributed, while the silicon maps show bands of absence (carbon only deposition) and is only present in the form of silicon carbide deposition.

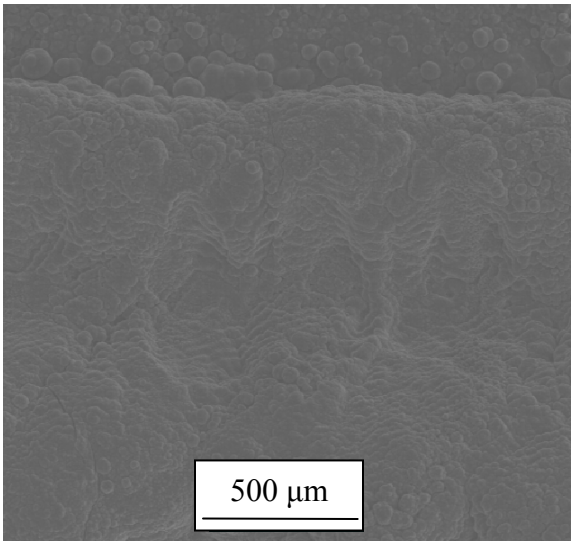

A

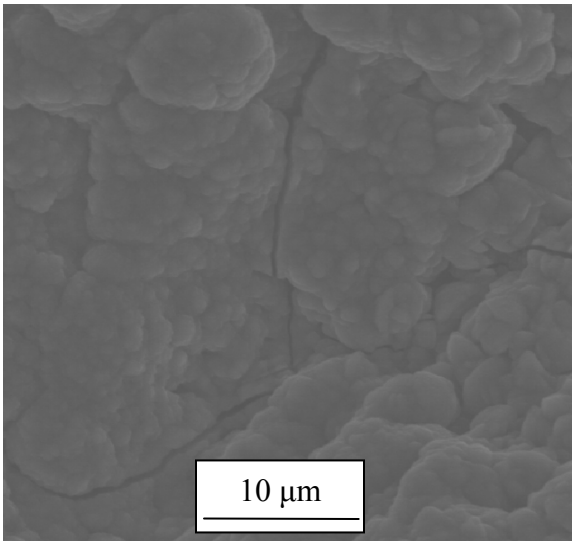

B

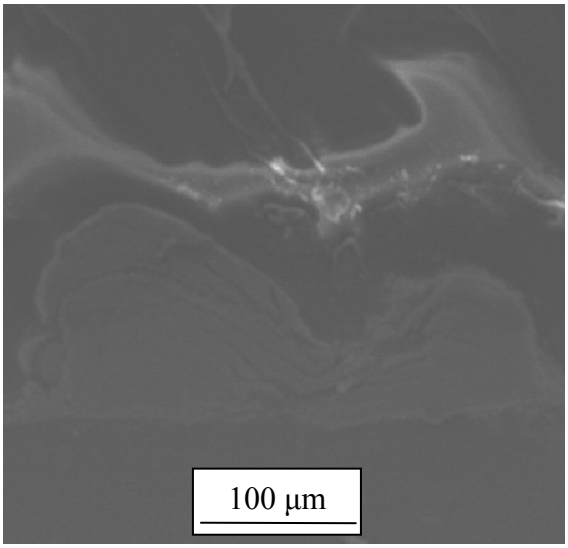

C

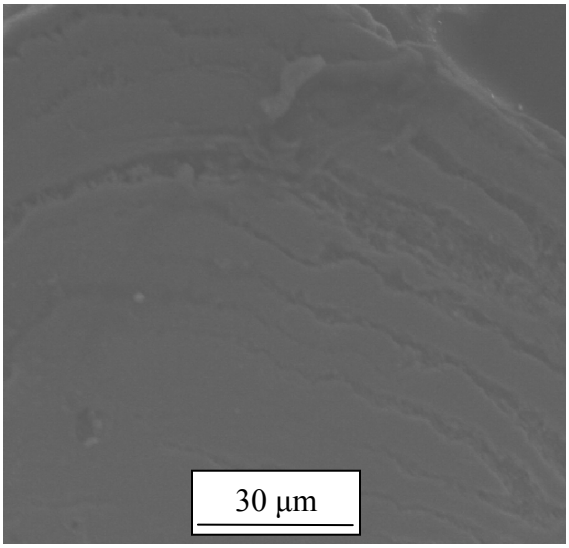

D

Appendix A-15. SEM micrograhs for MP-3-1: (A) external morphology, (B) cracks propagating in volcano, (C) transverse cross sectional view, (D) layer separation in the left peak.

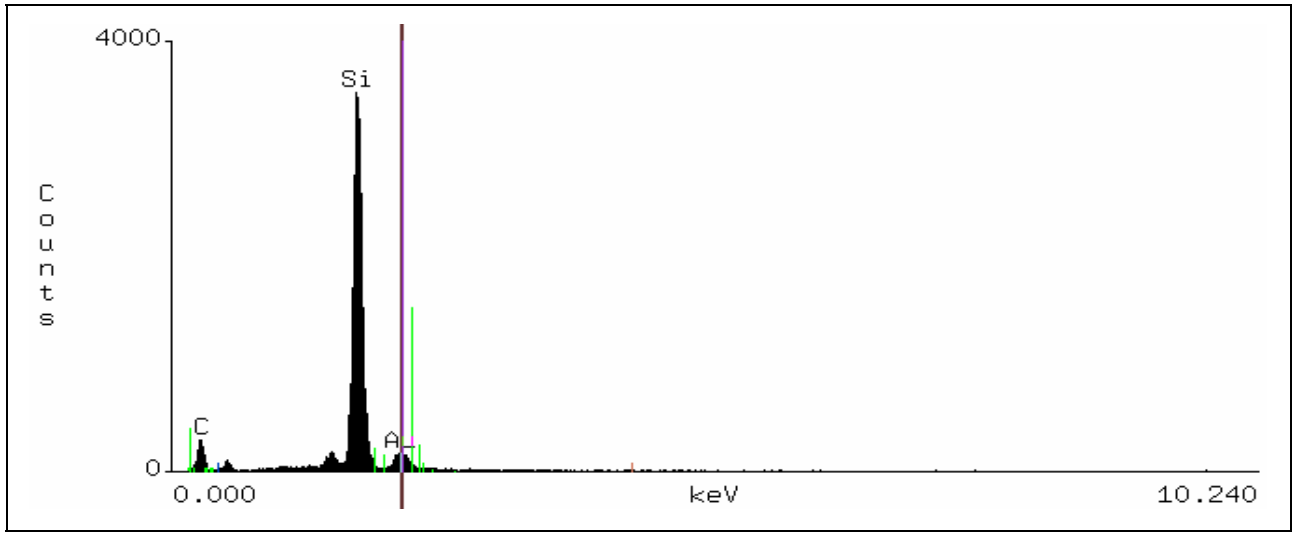

Quantitative Analysis MP-3-1

Filter Fit Method
Chi-sqd = 37.14 Livetime = 60.0 Sec.
Standardless Analysis

Element	Relative k-ratio	Error (1-Sigma)	Net Counts	Error (1-Sigma)
O -K	0.04006	+/- 0.00240	686	+/- 41
Si-K	0.79936	+/- 0.00517	36492	+/- 236
C -K	0.16058	+/- 0.00343	2247	+/- 48

Element	k-ratio (calc.)	ZAF	Atom %	Element Wt %	Wt % Err. (1-Sigma)	No. of Cations
O -K	0.0198	4.360	8.96	8.62	+/- 0.52	---
Si-K	0.3944	1.135	26.50	44.77	+/- 0.29	71.029
C -K	0.0792	5.884	64.54	46.62	+/- 1.00	172.969
Total			100.00	100.00		243.998

The number of cation results are based upon 24 Oxygen atoms

EDS Analysis for wall MP-3-1 which consists of carbon and silicon carbide.

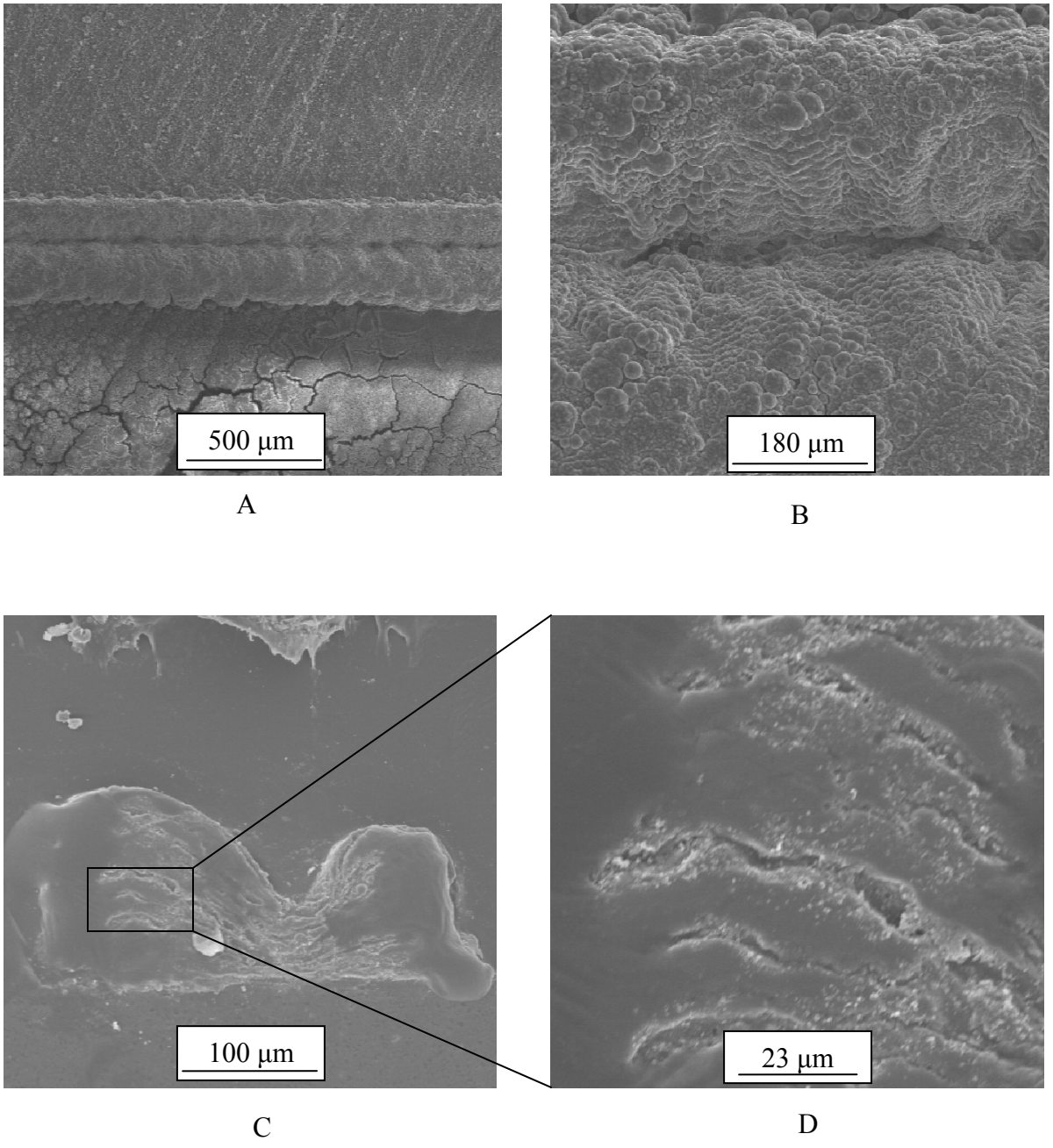

Appendix A-16. SEM micrographs of MP-3-2: (A) external view, (B) magnification of volcano, (C) transverse cross section, (D) voids or soft region in left peak

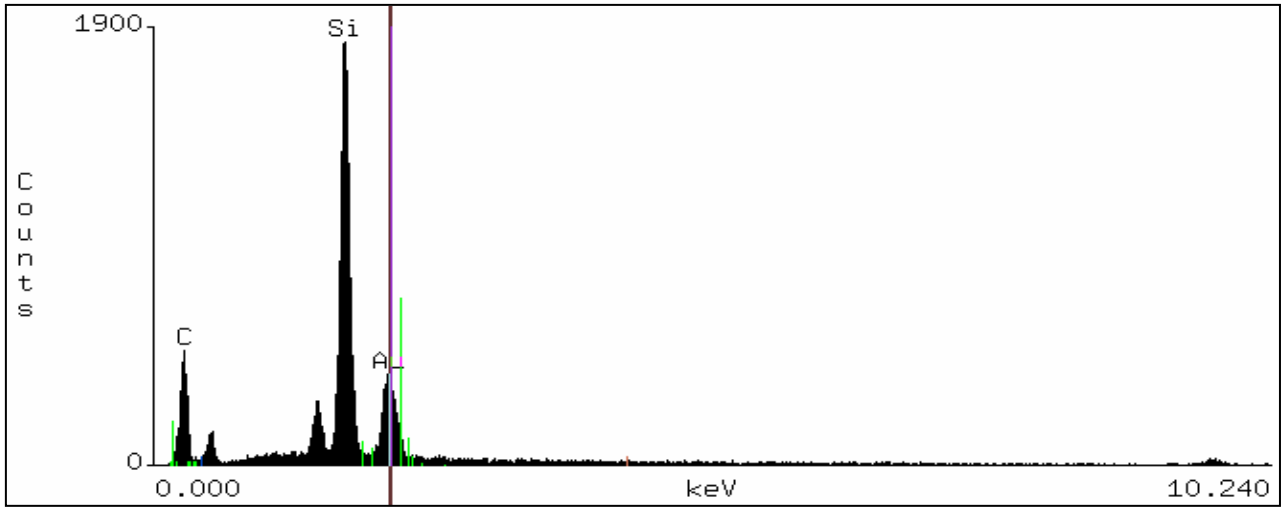

Quantitative Analysis MP-3-2

Filter Fit Method
Chi-sqd = 95.91 Livetime = 60.0 Sec.
Standardless Analysis

Element	Relative k-ratio	Error (1-Sigma)	Net Counts	Error (1-Sigma)
O -K	0.07557	+/- 0.00357	954	+/- 45
Si-K	0.55671	+/- 0.00514	18743	+/- 173
C -K	0.36773	+/- 0.00601	3793	+/- 62

Element	k-ratio (calc.)	ZAF	Atom %	Element Wt %	Wt % Err. (1-Sigma)	No. of Cations
O -K	0.0311	4.539	13.08	14.12	+/- 0.67	---
Si-K	0.2291	1.180	14.27	27.03	+/- 0.25	26.180
C -K	0.1513	3.889	72.65	58.85	+/- 0.96	133.278
Total			100.00	100.00		159.457

The number of cation results are based upon 24 Oxygen atoms

EDS Analysis of MP-3-2 showing dominant carbon deposition with minor amount of silicon carbide.

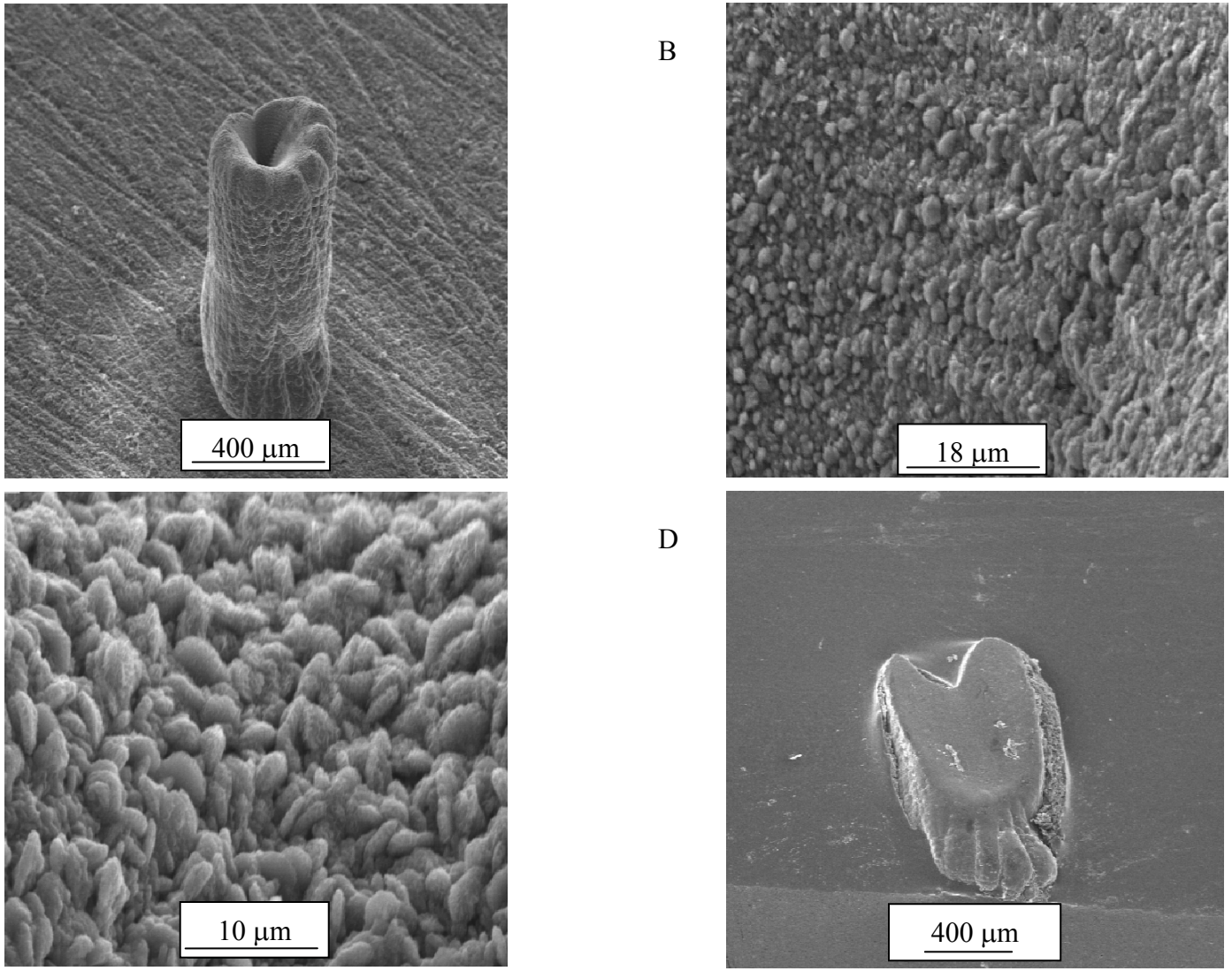

Appendix A-17. SEM micrographs of Trial MP-3-F1: (A) externl view, (B) inner surface of volcano, (C) plate-like grains on fiber tip, (D) longitudinal cross section.

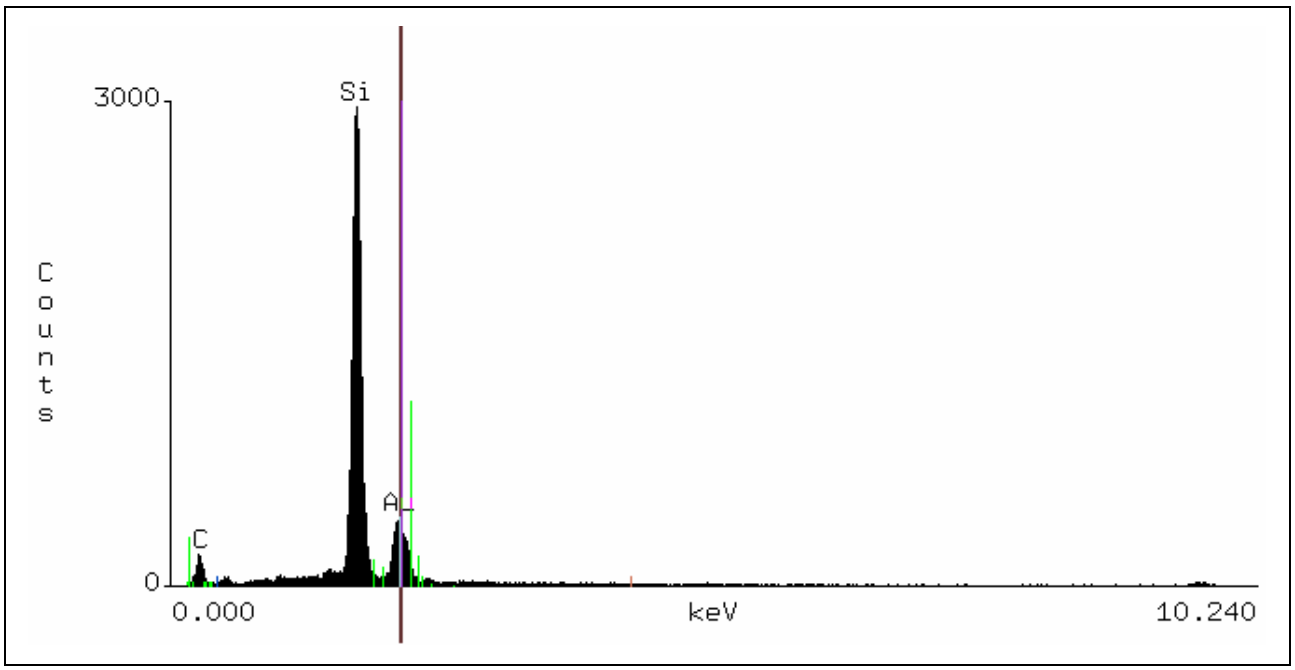

Quantitative Analysis MP-3-F1

Filter Fit Method
Chi-sqd = 57.03 Livetime = 60.0 Sec.
Standardless Analysis

Element	Relative k-ratio	Error (1-Sigma)	Net Counts	Error (1-Sigma)
O -K	0.02388	+/- 0.00277	329	+/- 38
Si-K	0.84929	+/- 0.00586	31144	+/- 215
C -K	0.12684	+/- 0.00365	1425	+/- 41

PROZA Correction Acc.Volt.= 15 kV Take-off Angle=39.62 deg Tilt = 30 deg
Number of Iterations = 7

Element	k-ratio (calc.)	ZAF	Atom %	Element Wt %	Wt % Err. (1-Sigma)	No. of Cations
O -K	0.0127	4.375	5.98	5.55	+/- 0.64	---
Si-K	0.4513	1.120	31.02	50.54	+/- 0.35	124.492
C -K	0.0674	6.515	63.01	43.91	+/- 1.26	252.901
Total			100.00	100.00		377.393

The number of cation results are based upon 24 Oxygen atoms

EDS of Fiber MP-3-F1

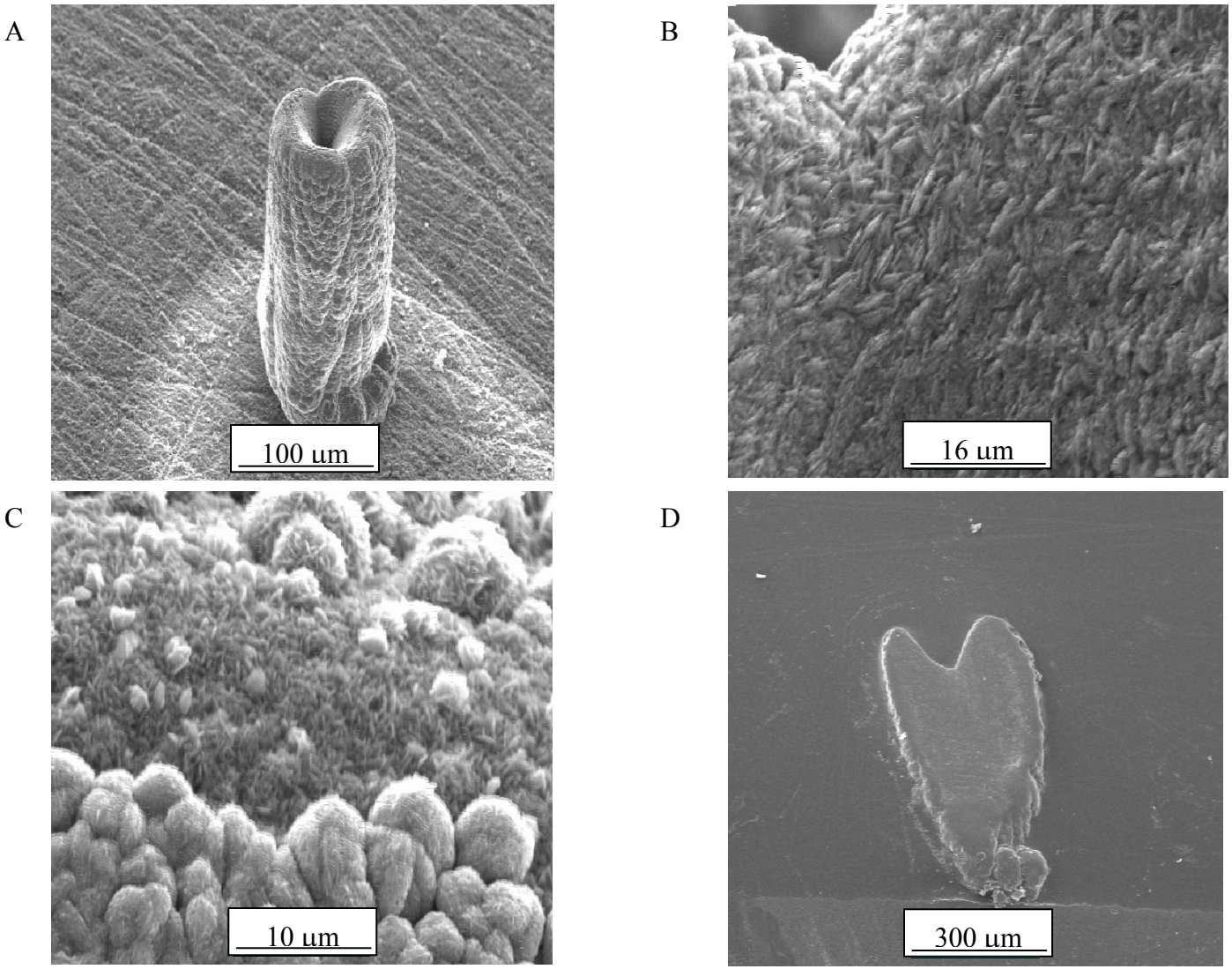

Appendix A-18. SEM micrographs of Trial MP-3-F2: (A) external view, (B) inner surface morphology, (C), fiber tip, and (D) longitudinal cross section view.

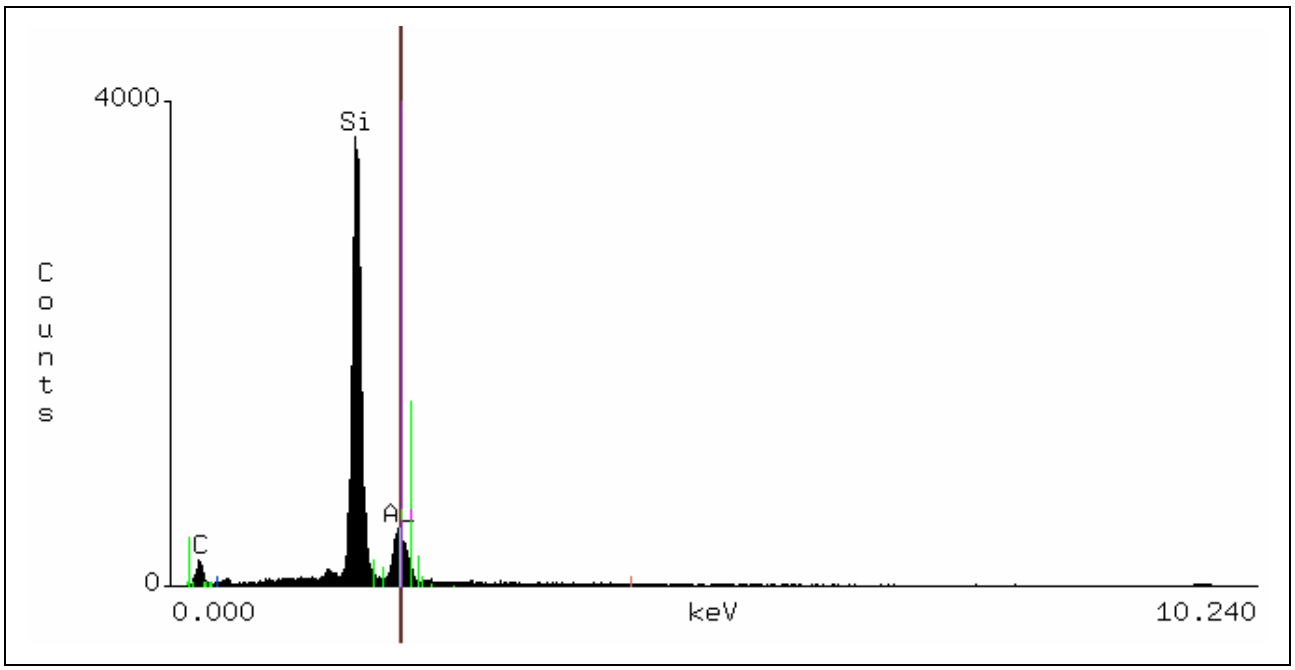

Quantitative Analysis MP-3-F2

Filter Fit Method
Chi-sqd = 69.00 Livetime = 60.0 Sec.
Standardless Analysis

Element	Relative k-ratio	Error (1-Sigma)	Net Counts	Error (1-Sigma)
O -K	0.01881	+/- 0.00243	318	+/- 41
Si-K	0.86966	+/- 0.00549	39118	+/- 247
C -K	0.11153	+/- 0.00319	1538	+/- 44

PROZA Correction Acc.Volt.= 15 kV Take-off Angle=39.62 deg Tilt = 30 deg
Number of Iterations = 7

Element	k-ratio (calc.)	ZAF	Atom %	Element Wt %	Wt % Err. (1-Sigma)	No. of Cations
O -K	0.0104	4.353	4.97	4.52	+/- 0.58	---
Si-K	0.4800	1.113	33.46	53.43	+/- 0.34	161.598
C -K	0.0616	6.831	61.58	42.05	+/- 1.20	297.424
Total			100.00	100.00		459.022

The number of cation results are based upon 24 Oxygen atoms

EDS of MP-3-F2.

Sample	Temperature	Scan Rate	Reagent Switch Time	Pressure	Grade	Height	Width
1.1.1	-1	-1	-1	-1	3		
1.1.2	-1	-1	-1	-1	0		
1.2.1	-1	-1	-1	-1	4		278
1.2.2	-1	-1	-1	-1	4	30	225.8
2.1.1	-1	-1	1	1	0		
2.1.2	-1	-1	1	1	2		
2.2.1	-1	-1	1	1	0		
2.2.2	-1	-1	1	1	2		
3.1.1	-1	1	-1	1	0		
3.1.2	-1	1	-1	1	3	245	345
3.2.1	-1	1	-1	1	4	50.86	
3.2.2	-1	1	-1	1	3	26.86	312
4.1.1	-1	1	1	-1	0	4.5	248.9
4.1.2	-1	1	1	-1	0	5	220
4.2.1	-1	1	1	-1	0		
4.2.2.	-1	1	1	-1	4	25.3	268.7
5.1.1	1	-1	-1	1	3		
5.1.2	1	-1	-1	1	3	122.9	221.4
5.2.1	1	-1	-1	1	0		
5.2.2	1	-1	-1	1	2		416.7
6.1.1	1	-1	1	-1	1	149.1	600
6.1.2	1	-1	1	-1	1	165	609.4
6.2.1	1	-1	1	-1	1	129.3	468.7
6.2.2	1	-1	1	-1	1	100	575.1
7.1.1	1	1	-1	-1	0		
7.1.2	1	1	-1	-1	1		
7.2.1	1	1	-1	-1	2	49	384.4
7.2.2	1	1	-1	-1	2	210.8	548.1
8.1.1	1	1	1	1	0		
8.1.2	1	1	1	1	2	175.1	414
8.2.1	1	1	1	1	1		470
8.2.2	1	1	1	1	2		380

Appendix A-19. Samples and data used for the ANOVA.

ANOVA for Overall Deposit Quality

	df	*SS*	*MS*	*F*	*Significance F*
Regression	4	11.125	2.78125	1.484249537	0.23464065
Residual	27	50.59375	1.873842593		
Total	31	61.71875			

	Coefficients	*Standard Error*	*t Stat*	*P-value*
Intercept	1.59375	0.241986737	6.586104751	4.58712E-07
Temperature	-0.21875	0.241986737	-0.903975162	0.374003919
Scan Rate	-0.09375	0.241986737	-0.387417927	0.701484062
Reagent Switch Time	-0.53125	0.241986737	-2.19536825	0.036912601
Pressure	0.09375	0.241986737	0.387417927	0.701484062

ANOVA for Volcano Effect

	df	*SS*	*MS*	*F*	*Significance F*
Regression	4	16.48503709	4.121259273	8.453671183	0.000604147
Residual	17	8.28769018	0.487511187		
Total	21	24.77272727			

	Coefficients	*Standard Error*	*t Stat*	*P-value*
Intercept	2.40387275	0.153623327	15.64783681	1.57992E-11
Temperature	-0.67081604	0.155531765	-4.313048503	0.000471547
Scan Rate	0.03042876	0.153073689	0.198785103	0.844788844
Reagent Switch Time	-0.42946058	0.153623327	-2.795542767	0.012421346
Pressure	0.06984785	0.152245512	0.458784337	0.652200293

ANOVA for Width Dimension

	df	*SS*	*MS*	*F*	*Significance F*
Regression	4	181947.4628	45486.8657	4.805192	0.013364201
Residual	13	123060.4883	9466.191409		
Total	17	305007.9511			

	Coefficients	*Standard Error*	*t Stat*	*P-value*
Intercept	358.238392	25.17730617	14.22862281	2.64E-09
Temperature	96.6930357	26.48607935	3.650711548	0.002933
Scan Rate	-2.49107142	26.00301	-0.095799349	0.925141
Reagent Switch Time	16.8133928	25.17730617	0.667799515	0.515943
Pressure	-30.6230357	26.48607935	-1.156193611	0.268408

A-20. ANOVA of the responces to the process variables.

ANOVA for Height Dimension

	df	*SS*	*MS*	*F*	*Significance F*
Regression	4	35399.40585	8849.851464	1.750955	0.215236498
Residual	10	50543.01079	5054.301079		
Total	14	85942.41664			

	Coefficients	*Standard Error*	*t Stat*	*P-value*
Intercept	104.700120	20.64621893	5.071152294	0.000484
Temperature	47.1733734	21.23687897	2.22129502	0.050583
Scan Rate	1.70156626	22.11480329	0.07694241	0.940187
Reagent Switch Time	-2.61409638	21.05690218	-0.124144395	0.903661
Pressure	26.2891566	22.62521209	1.161940782	0.272241

REFERENCES

1. L. S. Nelson and N. L. Richardson, "Formation of Thin Rods of Pyrolytic Carbon by Heating with a Focused Carbon Dioxide Laser," *Material Research Bulletin*, 1972, **7**, 971-976.

2. C. Duty, D. Jean, and W.J. Lackey, "Laser Chemical Vapor Deposition: Materials, Modeling, and Process Control," *International Materials Reviews*, 2001, **46**, 271-287.

3. R. C. Krutenat, and D. Scaringella, "Investigation of an Advanced CVD Process to form Creep Resistant SiC Filaments": 1993, **1**, 1-116.

4. A.J.P. Van Maaren, R.L. Krans, E. De Haas, and W.C. Sinke, "Excimer Laser-Induced Deposition of Tungsten on Silicon," *Applied Surface Science.*, 1989, **38**, 386-396.

5. D.H. Lowndes, D. Geoghegan, G. Eres, S. Pennycock, D. Mashburn, and G. Jellison, "Low Temperature Photon-controlled Growth of Thin Films and Multilayered Structures," *Applied Surface Science*, 1989, **36**, 59-69.

6. E. B. Flint, J. Messelhauser and H. Suhr, "Laser-induced Chemical Vapor Deposition of Rhodium," Institute of Organic Chemistry, *University of Tubingen*, Germany, 1991.

7. Chad E. Duty, "Design, Operation, and Heat and Mass Transfer Analysis of a Gas Jet Laser Chemical Vapor Deposition System," PH.D. Thesis, Mechanical Engineering, *Georgia Institute of Technology*, November 2001.

8. D. Tonneau, J. Bouree, and Y. Pauleau, "Photo-Assisted Metalorganic Vapor-phase Epitaxy of ZnSe on GaAs," *Applied Surface Science*, 1995, **86**, 488-493.

9. T. Baum, C. Larson, and R. Jackson, "Laser-Induced Chemical Vapor Deposition of Aluminum," *Applied Physics Letters*, 1989, **55**, (12), 1264-1266.

10. F. Wallenberger, "Inorganic Fibers and Microfabricated Parts by Laser Assisted Chemical Vapor Deposition," *Ceramic International*, 1997, **23**, 119-126.

11. K. Williams, J. Maxwell, K. Larsson, and M. Boman, "Freeform Fabrication of Microsolenoids, Electromagnets, and Helical Springs Using High-Pressure Laser Chemical Vapor Deposition", *IEEE*, 1999, 233-237.

12. R. Moylan, T. J. Baum, and C. R. Jones, "LCVD of Copper Deposition Rate and Deposit Shape," *Applied Physics A*, 1986, **40A**, 1-5.

13. J. Maxwell, M. Boman, K. Williams, K. Larsson, N. Jaikumar, and G. Saiprasanna, "High-Speed Laser Chemical Vapor Deposition of Amorphous Carbon Fibers, Stacked Conductive Coils, and Folded Helical Springs," Proc. Conf. Micromachining and Microfabrication Process Technology V, 1999, SPIE Proc. 3874, 227-235; 1999, Bellingham, Washington.

14. J. Maxwell, J. Pegna, and D. Messia, "Real Time Volumetric Growth Rate Measurements and Feedback Control of LCVD," *Applied Physics A*, 1998, **67A**, 323-329.

15. F. Petzoldt, K. Piglmayer, W.Krauter, and D. Bauerle, "Lateral Growth Rates in Laser CVD of Microstructures," *Applied Physics A*, 1984, **35A**, 155-159.

16. H. Chang, L. Lee, R. Hwang, C. Yeh, M. Lin, J. Lou, T. Hseu, T. Wu, Y.Chen, and C. Tang, "Physical and Chemical Properties of the Cylindrical Rods SiCx Grown from Si(CH3)2Cl2 by Laser Pyrolysis," *Material Chemistry and Physics*, 1996, **44**, 59-66.

17. I. Zergioti, A. Hatziapostolou, E. Hontsopoulos, A. Zervaki, and G. Haidemenopoulos, "Pyrolytic Laser-Based Chemical Vapour Deposition of TiC Coatings," *Thin Solid Films*, 1995, **271**, 96-100.

18. J. Elders and D.E.V. Voorst, "Laser Induced Chemical Vapor Deposition of Titanium Diboride and the Influence of Atomic Hydrogen," *Surface Coating Technologies*, 1991, **45**, 105-113.

19. J. Elders, and J. Van Voorst, "Laser-Induced CVD of Titanium Diboride and the Influence of Atomic Hydrogen," *Applied Surface Science*, 1993, **69**, 267-271.

20. Daniel Louis Jean, "Design and Operation of an Advanced Laser Chemical Vapor Dposition System with Online Control," Ph.D. Thesis, Mechanical Engineering, *Georgia Institute of Tecnology*, June 2001

21. D. Jean, C. Duty, R. Johnson, S. Bondi, and W.J. Lackey, "Carbon Fiber Growth Kinetics and Thermodynamics Using Temperature Controlled LCVD," *Carbon*, 2002, **40**, 1435-1445.

22. W.J. Lackey, David Rosen, Chad Duty, Daniel Jean, Scott Bondi, Tarek Elkhatib, Ryan Johnson, MingXuan Jiang, Jian Mi, Josh Gillespie, and Racheal Harvey, "Laser CVD System Design, Operation, and Modeling," *2002 National Science Foundation Design, Service, Manufacturing and Industrial Innovation Research Conference*, San Juan, Puerto Rico, January 7-10, 2002

23. E. Minford, Robert E. Stevens, Vincent L. Magnotta, Paul N. Dyer, Thomas R. Watkins, and David J. Green, "Effects of Deposition Conditions on the

Microstructure and Properties of CVD SiC," *Material Research Society Symposium Proceedings*, 1990, **168**, 233-238.

24. J. Han and K. Jensen, Combined Experimental and Modeling Studies of Laser-assisted CVD of Cu from Copper (1)-Hexaflouroacetylacetonate Trimethylvinylsilane," *Journal of Applied Physics IV*, 1994, **75**, 2240-2250.

25. J. Maxwell, K. Larsson, M. Boman, P. Hooge, Kirk Williams, P. Coane, "Rapid Prototyping of functional three dimensional Microsolenoids and Electromagnets by High-Pressure Laser Chemical Vapor Deposition," *Solid Freeform Fabrication Symposium Proceedings*, 1998, 529-536.

26. Akio Watanabe, Kazuo Osato, Shinji Ninomiya, Masakazu Mukaida, Tatsuo Tsunoda and Yoji Imai, "SiC Thin Film Preparation by ArF Excimer Laser Chemical Vapor Deposition," *Thin Solid Films*, 1996, **274**, 70-75.

27. Angus I. Kingon, Leonard J. Lutz, P. Liaw, and Robert F. Davis, "Thermodynamics Calculations of the Chemical Vapor Deposition of Silicon Carbide," *Journal of the American Ceramic Society*, 1983, **66**, 558-566.

28. M. D. Allendorf, T. H. Osterheld, and C. F. Melius, "The Decomposition of Methyltrichlorosilane: Studies in a High-Temperature Flow Reactor," *Materials Research. Society Symposium Proceedings*, **334**, 1993, 105-110.

29. T. M. Besmann and M. L. Johnson, "Kinetics of the Low-Pressure Chemical Vapor Deposition of Silicon Carbide," pp. 443-56 in *Proc. 3rd Int'l. Sym. Ceramic Materials and Components for Engines*, Las Vegas, NV, November 27-30, 1988.

30. J. Chin, P. K. Gantzel, and R. G. Hudson, "The Structure of Chemical Vapor Deposited Silicon Carbide," *Thin Solid Films*, 1977, **40**, 57-72.

31. S. Suresh and A. E. Giannakopoulos, "A New Method for Estimating Residual Stresses by Instrumented Sharp Indentation," *Acta Mater*, 1998, **Vol 46**, No. 16, 5755-5767.

32. Lu, Yong-Feng, "Square Shaped Temperature distribution induced by a Gaussian-shaped laser beam," *Applied Surface Science*, 1994, **81**, 357-364.